Master Thesis

修士論文

Search for proton decay into charged antilepton and η meson in Super-Kamiokande

（スーパーカミオカンデにおける反荷電レプトンと
η 中間子に崩壊する陽子崩壊の探索）

January 2021

令和３年１月修士（理学）申請

Department of Physics, Graduate School of Science,
The University of Tokyo

東京大学大学院理学系研究科物理学専攻

Natsumi Ogawa

小川　夏実

Abstract

There are four fundamental forces in nature: the electromagnetic, weak, strong, and gravitational forces. They are believed to be originated from a single unified force at the very beginning of our universe. Grand Unified Theories explain the unification of the electromagnetic, weak, and strong forces and most of them predict protons to decay into lighter particles. In this thesis, a search of proton decay into an antilepton and a η meson has been performed. The cross sections of η nuclear effect are revised from the latest published paper, resulting in reducing their uncertainties around by a factor of two. We analyze the data exposure of 55.7 kiloton·years (905.0 live days) of Super-Kamiokande. No candidate event for the proton decay has been found. By combining the results of other data taking period from the previous research, the lifetime limit for $p \to e^+\eta$ ($p \to \mu^+\eta$) has been set to be 1.33×10^{34} (6.1×10^{33}) years with a total of 0.373 Megaton·years exposure (3244.4 live days). This gives 28% (30%) longer lifetime limit than that of the latest published result and the most stringent limit for these modes in the world.

Table of Contents

Abstract **v**

Table of Contents **vii**

List of Figures **ix**

List of Tables **xiii**

1 Underlying Physics **1**
1.1 The Standard Model 1
1.1.1 Gauge Symmetry 1
1.1.2 Spontaneous Symmetry Breaking 3
1.1.3 Electroweak Unification 5
1.2 Grand Unified Theories 6
1.2.1 SU(5) Model 6
1.2.2 SUSY SU(5) Model 7
1.2.3 SO(10) Model 8
1.2.4 Proton Decay into an Antilepton and a Meson 8
1.3 History of Nucleon Decay Research 8
1.4 Thesis Overview 10

2 The Super-Kamiokande Experiment **11**
2.1 The Super-Kamiokande Detector 11
2.1.1 Princeple of the Detector 12
2.1.2 Photodetection 13
2.1.3 Water Purification 16
2.2 Event Reconstruction 17
2.2.1 Vertex Fitting 17
2.2.2 Ring Counting 19
2.2.3 Particle Identification 20
2.2.4 Momentum Determination 23
2.2.5 Michel Electron Finding 24
2.2.6 Neutron Tagging for SK-IV 24
2.3 Accumulated Data of Super-Kamiokande 24

3 **Event Simulation** **27**
3.1 Proton Decay Simulation . . . 27
3.1.1 Fermi Motion of Nucleons . . . 28
3.1.2 Correlated Decay . . . 28
3.1.3 η Nuclear Effect . . . 29
3.2 Background Simulation . . . 29
3.2.1 Atmospheric Neutrino Flux . . . 29
3.2.2 Neutrino Interactions . . . 30
3.2.3 π Nuclear Effect . . . 33
3.3 Detector Simulation . . . 34

4 **Evaluation of η Meson Nuclear Effect** **35**
4.1 Reaction Processes of η Mesons in Super-Kamiokande . . . 35
4.1.1 Internal Nuclear Effect . . . 35
4.1.2 Decay Modes of Survived η Mesons . . . 36
4.2 η Photoproduction Reaction . . . 36
4.2.1 Experiment at Mainz . . . 36
4.2.2 Simulation of η Photoproduction Reaction with η Nuclear Effect . . . 36
4.2.3 Systematic Uncertainties in the Previous Study . . . 38
4.3 Interpolating the η Nuclear Effect Cross Section . . . 41
4.3.1 Fitting Two Experimental Data with Least Chi-square Method . . . 42
4.3.2 Estimation of the Uncertainty of Fitting Parameters . . . 43
4.3.3 Reduced χ^2 value and the goodness of fit . . . 44
4.3.4 Fit with three different functions . . . 45
4.3.5 Goodness of Fittings . . . 50
4.3.6 Uncertainty Estimation from Each Function . . . 51
4.4 Estimation of Effect on Proton Decay Search . . . 53

5 **Proton Decay Analysis** **55**
5.1 Proton Decay Search . . . 55
5.1.1 Selection Criteria . . . 55
5.1.2 Signal Efficiencies and The Number of Background Events . . . 63
5.1.3 Confirmation of Data Agreement with MC . . . 65
5.1.4 Results . . . 74
5.2 Systematic Uncertainties . . . 74
5.2.1 Systematic Uncertainties on Signal Efficiency . . . 75
5.2.2 Systematic Uncertainties on the Number of Background Events . . . 75
5.3 Lifetime Limits . . . 78
5.3.1 Lifetime Estimation . . . 78
5.3.2 Final Results . . . 79

6 **Discussion and Conclusion** **81**
6.1 Comparison with GUT models . . . 81
6.2 Conclusion . . . 81
6.3 Future Prospects . . . 82

Acknowledgements **83**

Bibliography **85**

List of Figures

1.1 Shape of potential $V(\phi^2)$ under $\mu^2 < 0$ and $\lambda > 0$ 4
1.2 Feynman diagrams of proton decay via X and Y bosons 6
1.3 Running coupling constants α_1^{-1}, α_2^{-1} and α_3^{-1} as a function of energy scale in minimal SU(5) and minimal SUSY SU(5) model 7
1.4 Summary of lower limits of nucleon partial lifetime from several experiments 9

2.1 Overview of the Super-Kamiokande detector 12
2.2 Outline drawing of Cherenkov light 13
2.3 Schematic view of a 20-inch ID PMT 14
2.4 Quantum efficiency of the photocathode as a function of wavelength 14
2.5 Timing chart of ATM operation in SK-I to SK-III 15
2.6 Timing chart of QTC operation QBEE for SK-IV 16
2.7 An observed charge distribution as a function of Cherenkov opening angle (top) and its second derivative (bottom) 18
2.8 An outline drawing of detecting additional rings 19
2.9 Typical shower-like (e-like) ring pattern 20
2.10 Typical non shower-like (μ-like) ring pattern 21
2.11 Area where photons are emitted by a muon 21
2.12 Distributions of RTOT and true momentum up to 2000 MeV/c for both e-like and μ-like rings 23

3.1 Distributions for simulated momentum (left) and invariant mass (right) after the proton decay events 27
3.2 Invariant mass distribution of the decayed proton in ^{16}O for $p \to e^+\eta$ MC . 28
3.3 Direction-averaged atmospheric neutrino flux at SK calculated by the Honda flux 29
3.4 The simulated cross sections for ν ($\bar{\nu}$) interactions in NEUT with data . . . 30
3.5 Calculated cross sections of CCQE scattering with experimental data as the function of neutrino energy 31
3.6 Calculated cross sections of $\nu + N \to l + N' + \pi$ interactions with data as the function of neutrino energy 32
3.7 Total CC interactions of CCQE scattering, single meson production, and deep inelastic scattering with data as the function of neutrino energy 32
3.8 Measered and NEUT simulated cross sections of $\pi^+ - {}^{12}$C scattering (left) and of $\pi^+ - {}^{12}$C scattering (right) as a function of pion momentum 33
3.9 Fraction of final state of pion interaction as a function of pion momentum . 33

4.1 Measured differential cross sections of photoproduction of η mesons in the laboratory system on a ^{12}C target identified by γ-rays with energies of $E_\gamma = 735 - 765$ MeV . . . 37
4.2 Image of how the simulation of η photoproduction with a ^{12}C target proceeds 37
4.3 Calculated cross section of η nuclear effect, $\sigma_{\text{nuc}}^{\text{prev}}$, from $\text{S}_{11}(1535)$ resonance state by the Breit-Wigner formula . . . 38
4.4 Measured and simulated differential cross sections of photoproduction of η mesons according to Breit-Wigner formula on a ^{12}C target with γ-rays with energies of $E_\gamma = 735 - 765$ MeV . . . 39
4.5 Distributions of the final state of η mesons of the $p \to e^+\eta$ MC events . . . 40
4.6 Measured absorption cross section of η as a function of the laboratory momentum of η obtained by the experiment at Mainz . . . 42
4.7 χ^2 distribution when the cross section of the nuclear effect is assumed as $\sigma_{\text{nuc}} = a$ [mb] . . . 45
4.8 Measured η absorption cross sections, σ_{abs}, and assumed cross sections of η nuclear effect in the η photoproduction simulation as $\sigma_{\text{nuc}} = a$ [mb] . . . 46
4.9 Measured and simulated differential cross sections of photoproduction of η assuming the cross section of the η nuclear effect as $\sigma_{\text{nuc}} = a$ [mb] . . . 46
4.10 χ^2 distribution when the cross section of the nuclear effect is assumed as $\sigma_{\text{nuc}} = a \cdot \exp(-b \cdot p_\eta)$ [mb] . . . 47
4.11 Measured η absorption cross sections, σ_{abs}, and assumed cross sections of η nuclear effect in the η photoproduction simulation as $\sigma_{\text{nuc}} = a \cdot \exp(-b \cdot p_\eta)$ [mb] . . . 47
4.12 Measured and simulated differential cross sections of photoproduction of η assuming the cross section of the η nuclear effect as $\sigma_{\text{nuc}} = a \cdot \exp(-b \cdot p_\eta)$ [mb] 48
4.13 χ^2 distribution when the cross section of the nuclear effect is assumed as $\sigma_{\text{nuc}} = a + b \cdot \exp(-c \cdot p_\eta)$ [mb] . . . 49
4.14 Measured η absorption cross sections, σ_{abs}, and assumed cross sections of η nuclear effect in the η photoproduction simulation as $\sigma_{\text{nuc}} = a \cdot \exp(-b \cdot p_\eta)$ [mb] . . . 49
4.15 Measured and simulated differential cross sections of photoproduction of η assuming the cross section of the η nuclear effect as $\sigma_{\text{nuc}} = a + b \cdot \exp(-c \cdot p_\eta)$ [mb] . . . 50
4.16 Momentum distributions of η mesons from bound protons of $p \to e^+\eta$ (left) and $p \to \mu^+\eta$ (right) . . . 51

5.1 A typical PMT hit pattern of $p \to e^+\eta$, $\eta \to 2\gamma$ events in SK . . . 56
5.2 A typical PMT hit pattern of $p \to e^+\eta$, $\eta \to 2\gamma$ events in SK . . . 56
5.3 Distributions of the number of ring of the $p \to e^+\eta$ (left) and $p \to \mu^+\eta$ (right) MC . . . 58
5.4 Distributions of the number of ring depending on the decay modes of the η meson from $p \to e^+\eta$ (left) and $p \to \mu^+\eta$ (right) MC . . . 58
5.5 Distributions of reconstructed η invariant mass of the $p \to e^+\eta$ MC in SK-IV after applying the selection criteria A and B . . . 59
5.6 Distributions of reconstructed η invariant mass of the $p \to \mu^+\eta$ MC in SK-IV after applying the selection criteria A and B . . . 60
5.7 Distributions of the number of Michel electrons of the $p \to e^+\eta$ (left) and $p \to \mu^+\eta$ (right) MC after applying the selection criteria A-C . . . 61

5.8 Distributions of reconstructed invariant total mass of the $p \to e^+\eta$ (left) and $p \to \mu^+\eta$ (right) MC after applying the selection criteria A-D 62
5.9 Distributions of reconstructed total momentum of the $p \to e^+\eta$ (left) and $p \to \mu^+\eta$ (right) MC after applying the selection criteria A-D 62
5.10 Distributions of the number of neutrons of the $p \to e^+\eta$ (left) and $p \to \mu^+\eta$ (right) MC after applying the selection criteria A-D 63
5.11 Scatter plots of total mass and total momentum after applying the selection criteria A-D for $p \to e^+\eta$, $\eta \to 2\gamma$ search 66
5.12 Scatter plots of total mass and total momentum after applying the selection criteria A-D for $p \to \mu^+\eta$, $\eta \to 2\gamma$ search 66
5.13 Distributions of reconstructed total momenta outside the signal region after applying the selection criteria A-D for $p \to e^+\eta$ (left) and $p \to \mu^+\eta$ (right) . 67
5.14 Distributions of reconstructed total masses outside the signal region after applying the selection criteria A-D for $p \to e^+\eta$ (left) and $p \to \mu^+\eta$ (right) . 67
5.15 The signal efficiencies (upper) and the number of expected backgrounds (lower, red histogram) and data candidates (lower, black circles) of SK-IV for $p \to e^+\eta$, $\eta \to 2\gamma$ search on the left and $p \to \mu^+\eta$, $\eta \to 2\gamma$ search on the right 68
5.16 Reconstructed total invariant mass and momentum of proton decay MC (upper), atmospheric neutrino MC (middle), and data (lower) for $p \to e^+\eta$, $\eta \to 2\gamma$ search on the left and $p \to \mu^+\eta$, $\eta \to 2\gamma$ search on the right 69
5.17 Distributions of reconstructed total invariant momentum of the $p \to l^+\eta$ MC (upper), and atmospheric neutrino MC and data (lower) for $p \to e^+\eta$ search on the left and $p \to e^+\eta$ search on the right 70
5.18 The signal efficiencies (upper) and the number of expected backgrounds (lower, red histogram) and data candidates (lower, black circles) of from SK-I to SK-IV for $p \to e^+\eta$, $\eta \to 2\gamma$ search on the left and $p \to \mu^+\eta$, $\eta \to 2\gamma$ search on the right 71
5.19 Reconstructed total invariant mass and momentum of the data from SK-I to SK-IV period for $p \to e^+\eta$, $\eta \to 2\gamma$ search on the left and $p \to \mu^+\eta$, $\eta \to 2\gamma$ search on the right 72

List of Tables

1.1 Predicted branching ratios for proton decay modes into a positron and a meson based on SU(5) and SO(10) models 8

2.1 The summary of SK data taking periods 11
2.2 The summary of Cherenkov momentum thresholds in water 12
2.3 Specifications of the 20-inch ID PMTs 14

4.1 Decay mode and the branching ratio of the $S_{11}(1535)$ resonance state . . . 35
4.2 Decay modes and the branching ratios of η mesons 36
4.3 Fraction of the final states of η meson after the proton decay of $p \to l^+\eta$ in ^{16}O with the η nuclear effect deduced from the Breit-Wigner formula 39
4.4 Fraction of the final states of η meson from the proton decay of $p \to e^+\eta$ in ^{16}O when the η nuclear effect is assumed as $\sigma_{\text{nuc}} = a$ [mb] 51
4.5 Fraction of the final states of η meson from the proton decay of $p \to \mu^+\eta$ in ^{16}O when the η nuclear effect is assumed as $\sigma_{\text{nuc}} = a$ [mb] 52
4.6 Fraction of the final states of η meson from the proton decay of $p \to e^+\eta$ in ^{16}O when the η nuclear effect is assumed as $\sigma_{\text{nuc}} = a \cdot \exp(-b \cdot p_\eta)$ [mb] . . 52
4.7 Fraction of the final states of η meson from the proton decay of $p \to \mu^+\eta$ in ^{16}O when the η nuclear effect is assumed as $\sigma_{\text{nuc}} = a \cdot \exp(-b \cdot p_\eta)$ [mb] . 52
4.8 The no η nuclear interaction rate of η meson from the proton decay of $p \to e^+\eta$ in ^{16}O when the η nuclear effect is assumed as $\sigma_{\text{nuc}} = a$ [mb] or $\sigma_{\text{nuc}} = a \cdot \exp(-b \cdot p_\eta)$ [mb] 53
4.9 The no η nuclear interaction rate of η meson from the proton decay of $p \to \mu^+\eta$ in ^{16}O when the η nuclear effect is assumed as $\sigma_{\text{nuc}} = a$ [mb] or $\sigma_{\text{nuc}} = a \cdot \exp(-b \cdot p_\eta)$ [mb] 53

5.1 Event selection criteria for $p \to l^+\eta, \eta \to 2\gamma$ modes 57
5.2 Number of events satisfying each event selection criteria of $p \to l^+\eta$, $\eta \to 2\gamma$ mode within 10,000 of $p \to l^+\eta$ events in MC and 500 years of atmospheric neutrino MC events 64
5.3 Signal efficiencies (ratios) for $p \to l^+\eta$, $\eta \to 2\gamma$ mode against the number of $p \to l^+\eta$ events in MC 64
5.4 Number of events and ratios satisfying each event selection criteria of $p \to l^+\eta$, $\eta \to 2\gamma$ mode within 3615 (3553) of $p \to e^+\eta$, $\eta \to 2\gamma$ ($p \to \mu^+\eta$, $\eta \to 2\gamma$) events in MC 64
5.5 Breakdown (number of events contribution) of the neutrino interaction modes of the background events in the signal boxes 65

5.6 Summary of the signal efficiencies, the number of expected background events and the number of candidate events from 91.5, 49.1, 31.8, and 199.9 kton·years exposure during SK-I, SK-II, SK-III, and SK-IV periods 73
5.7 Summary of the systematic uncertainties (percentage contribution) on signal efficiencies for each factors for SK-IV period 74
5.8 Summary of the systematic uncertainties (percentage contribution) on the number of background events for each factors for SK-IV period 77
5.9 Impact of signal efficiencies and their systematic errors on lifetime limit . . 80
5.10 Summary of proton decay search of $p \to l^+\eta$ 80

Chapter 1

Underlying Physics

In our universe, all the interactions, or forces, are known to be described by the four fundamental forces: the electromagnetic, weak, strong, and gravitational forces. They are believed to be fundamentally equivalent and to be differentiated from a unified force at the very beginning of our universe. The elucidation of the unified description of the four forces is one of the primary goals of particle physics. Many approaches both on experimental and theoretical aspects have been made to verify the unification. The Standard Model (SM), the theoretical framework of current particle physics, describes elementary particles with electromagnetic, weak, and strong interactions. The Glashow-Weinberg-Salam theory in 1967 and 1968 [1,2] successfully explained the unification of the electromagnetic and weak interactions as the electroweak force. Therefore, the next idea is to unify the three forces of the electromagnetic, weak, and strong forces. Such theoretical hypotheses to merge them are called Grand Unified Theories (GUT).

1.1 The Standard Model

The Standard Model is a mathematical model in particle physics which describes the three fundamental forces: the electromagnetic, weak, and strong forces. The framework is based on the gauge group $SU(3) \times SU(2) \times U(1)$, where $SU(2) \times U(1)$ and $SU(3)$ describe the electroweak and the strong forces, respectively. In the model, the interactions are described as exchanges of gauge bosons: photons, W, Z, and gluons.

1.1.1 Gauge Symmetry

Symmetry is the fundamental concept of the current particle physics. In particular, the gauge symmetry, which requires Lagrangians to be invariant under a group of local transformation, describes the dynamics of elementary particles in the Standard Model.

(1) Quantum Electrodynamics (QED)

The first idea of gauge symmetry can be found from classical electromagnetism. The physical $\boldsymbol{E}$ and $\boldsymbol{B}$ fields, obtained from the scalar and vector potentials ϕ and $\boldsymbol{A}$, do not change under the gauge transformation of

$$\phi \to \phi' = \phi - \frac{\partial \chi}{\partial t} \quad \text{and} \quad \mathbf{A} \to \mathbf{A}' = \mathbf{A} + \boldsymbol{\nabla}\chi. \tag{1.1}$$

This gauge transformation is written succinctly by $A_\mu = (\phi, -\mathbf{A})$ and $\partial_\mu = (\partial_0, \boldsymbol{\nabla})$ as

$$A_\mu \to A'_\mu = A_\mu - \partial_\mu \chi. \tag{1.2}$$

Suppose there is a fundamental symmetry requiring that physics is invariant in the universe under local phase transformations defined as

$$\psi(x) \to \psi'(x) = \hat{U}(x)\psi(x) = e^{iq\chi(x)}\psi(x). \tag{1.3}$$

Here, the phase $q\chi(x)$ is a function of space-time x that can be different at all points. Under this local U(1) phase transformation, the free-particle Dirac equation

$$i\gamma^\mu \partial_\mu \psi = m\psi, \tag{1.4}$$

becomes

$$i\gamma^\mu \partial\mu \left(e^{iq\chi(x)\psi}\right) = me^{iq\chi(x)\psi}\psi, \tag{1.5}$$
$$\Leftrightarrow e^{iq\chi(x)}\ i\gamma^\mu \left[\partial_\mu \psi + iq\left(\partial_\mu \chi\right)\psi\right] = e^{iq\chi(x)} m\psi, \tag{1.6}$$
$$i\gamma^\mu \left(\partial_\mu + iq\partial_\mu \chi\right)\psi = m\psi. \tag{1.7}$$

Here the additional term $-q\gamma^\mu(\partial_\mu \chi)\psi$ appears compared to Eq. (1.4). Therefore, the invariance under a U(1) local phase transformation is not satisfied for the free-particle Dirac equation. To establish the required invariance, equation Eq. (1.4) needs to be modified as

$$i\gamma^\mu(\partial_\mu + iqA_\mu)\psi - m\psi = 0. \tag{1.8}$$

where A_μ is interpreted as the electromagnetic field corresponding to a massless gauge boson, photon. Then, Eq. (1.8) is kept invariant under the U(1) local gauge transformation of Eq. (1.3) with

$$A_\mu \to A'_\mu = A_\mu - \partial_\mu \chi. \tag{1.2}$$

In the form of Lagrangian $\mathcal{L}$, Eq. (1.8) can be written as

$$\mathcal{L} = \bar{\psi}(i\gamma_\mu \mathcal{D}^\mu - m)\psi, \tag{1.9}$$
$$\mathcal{D} = \partial^\mu + ieA^\mu. \tag{1.10}$$

They are invariant under the gauge transformation. The Lagrangian for the QED, $\mathcal{L}_{\text{QED}}$, is described as below by adding the factors for the motions of photons

$$\mathcal{L}_{\text{QED}} = \bar{\psi}(i\gamma_\mu \mathcal{D}^\mu - m)\psi - \frac{1}{4} f^{\mu\nu} f_{\mu\nu}, \tag{1.11}$$
$$f^{\mu\nu} \equiv \partial^\mu A^\nu - \partial^\mu A^\nu. \tag{1.12}$$

(2) Quantum Chromodynamics (QCD)

The strong interaction is described by Quantum Chromodynamics (QCD) and requires to be invariant under unitary transformations in color space with color charges of r, g, and b.

This symmetry is preserved under the SU(3) local color phase transformation as described below:

$$\psi(x) \to \psi'(x) = \exp\left[ig_S \boldsymbol{\alpha(x)} \cdot \hat{\mathbf{T}}\right]\psi(x), \tag{1.13}$$

where $\hat{\mathbf{T}} = \{\mathbf{T^a}\}$ are the eight generators of the SU(3) symmetry group written in terms of Gell-Mann matrices and $\boldsymbol{\alpha(x)} = \alpha(x)^a$ are the eight functions of the space-time coordinate x. The Lagrangian for the strong interaction can be formulated as gauge invariant for SU(3) conversion as

$$\mathcal{L}_{\mathrm{QCD}} = \bar{\psi}(i\gamma_\mu D^\mu - m)\psi - \frac{1}{4}F_a^{\mu\nu}F_{\mu\nu}^a, \tag{1.14}$$

$$D^\mu = \partial^\mu + ig_S(G_a^\mu T^a), \tag{1.15}$$

$$F_{\mu\nu}^a = \partial_\mu G_\nu^a - \partial_\nu G_\mu^a - g_S f_{abc} G_\mu^b G_\nu^c, \tag{1.16}$$

where G_μ^a are the eight gauge fields, f_{abc} are the structure constants of the SU(3) group with commutation relations of $[\lambda_a, \lambda_b] = 2if_{abc}\lambda_c$. Similar to QED, the phase transformations give rise to additional terms of $g_S f_{abc} G_\mu^b G_\nu^c$ due to the non-Abelian nature, which corresponds to the massless gauge bosons, gluons.

(3) Weak Interaction

The weak interaction requires local gauge invariance under the transformation in the weak isospin space. For the case of the first generation, the wave function for the weak interaction $\phi(x)$ can be expressed as weak isospin doublets of

$$\varphi(x) = \begin{pmatrix} \nu_e(x) \\ e^-(x) \end{pmatrix}, \quad \begin{pmatrix} u(x) \\ d(x) \end{pmatrix}, \tag{1.17}$$

$$\varphi(x) \to \varphi'(x) = \exp[ig_W \boldsymbol{\alpha(x)} \cdot \mathbf{T}]\varphi(x). \tag{1.18}$$

The SU(2) gauge invariant Lagrangian for the weak interaction can be formulated as

$$\mathcal{L} = i\bar{\varphi}\gamma_\mu(\partial^\mu + ig_W \mathbf{W}^\mu \cdot \mathbf{T})\varphi, \tag{1.19}$$

where W stands for the three gauge fields of massless gauge bosons.

1.1.2 Spontaneous Symmetry Breaking

While the Lagrangian indicates the massless gauge bosons for the weak interaction, the experimental data indicate the non-zero masses of W and Z bosons. This fact breaks the required gauge symmetry of the Standard Model. To solve this problem, the ideas of the Higgs mechanism and the spontaneous symmetry breaking have been introduced [4, 5].

In general, the Lagrangian for a massless boson is described as

$$\mathcal{L} = \frac{1}{2}(\partial_\mu\phi)(\partial^\mu\phi). \tag{1.20}$$

Supposing the U(1) local gauge transformation $\phi(x) \to \phi'(x) = e^{ig\chi(x)}$, the gauge invariance can be achieved by replacing with the corresponding covariant derivatives of

$$\partial_\mu \to D_\mu = \partial_\mu + igB_\mu. \tag{1.21}$$

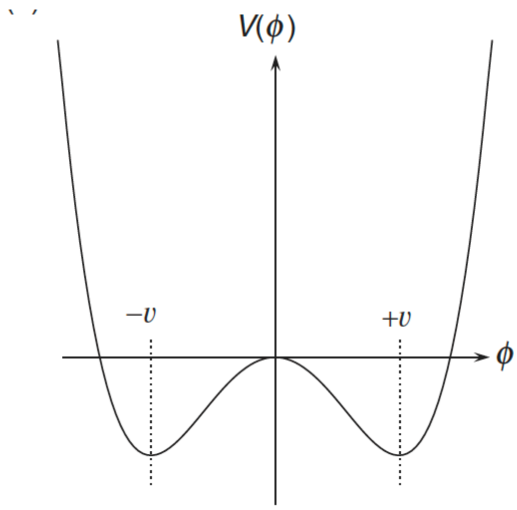

Fig. 1.1: Shape of potential $V(\phi^2)$ under $\mu^2 < 0$ and $\lambda > 0$. From [3].

Considering a scalar field ϕ with potential

$$V(\phi^2) = \frac{1}{2}\mu^2\phi^2 + \frac{1}{4}\lambda\phi^4, \tag{1.22}$$

the Lagrangian for ϕ is given by

$$\mathcal{L} = \frac{1}{2}(D_\mu\phi)^*(D^\mu\phi) - V(\phi^2) - \frac{1}{4}F^{\mu\nu}F_{\mu\nu}, \tag{1.23}$$

where $F^{\mu\nu}F_{\mu\nu}$ is the kinetic term for the new gauge field B^μ with

$$F^{\mu\nu} = \partial^\mu B^\nu - \partial^\nu B^\mu. \tag{1.24}$$

Here, the term $(\partial_\mu\phi)(\partial^\mu\phi)/2$ in $V(\phi^2)$ represents the kinetic energy of the scalar particle, $\mu^2/2$ stands for the mass of the particle, and ϕ^4 is related to the self-interactions of the scalar field. While parameters λ and μ satisfy $\lambda > 0$ and $\mu^2 < 0$ respectively, the potential $V(\phi^2)$ is minimized at

$$\phi = \pm v = \pm \left| \sqrt{\frac{-\mu^2}{\lambda}} \right|, \tag{1.25}$$

as shown in Figure 1.1. The field is expressed to have a non-zero vacuum expectation value v. Since the vacuum state can take either of $\phi = \pm v$ and breaks the symmetry of the Lagrangian, this process is called spontaneous symmetry breaking. The Lagrangian Eq. (1.23) can be written with a function of the excitation of the field $\eta(x) = \phi(x) - v$ as

$$\mathcal{L}(\eta) = \frac{1}{2}(\partial_\mu\eta)(\partial^\mu\eta) - \lambda v^2\eta^2 - \frac{1}{4}F_{\mu\nu}F^{\mu\nu} + \frac{1}{2}g^2v^2B_\mu B^\mu + \cdots . \tag{1.26}$$

The former and latter two terms represent the Lagrangian for η field with the mass of $m_\eta = \sqrt{2\lambda}v$ and that for a gauge boson with the mass of $m_B = gv$, respectively.

1.1.3 Electroweak Unification

The masses of W and Z gauge bosons are considered to be generated by the Higgs mechanism described in the previous section above. In the Glashow-Weinberg-Salam (GWS) model [1], the mechanism is embedded in the U(1)×SU(2) local gauge symmetry of electroweak interaction. The GWS theory gives the unified description of the electromagnetic and weak forces as electroweak interaction. To generate the masses of electroweak gauge bosons of $W^{\pm}$ and Z by the Higgs mechanism, the Higgs field is required to have at least two complex scalar fields:

$$\phi = \begin{pmatrix} \phi^+ \\ \phi^0 \end{pmatrix} = \frac{1}{\sqrt{2}} \begin{pmatrix} \phi_1 + i\phi_2 \\ \phi_3 + i\phi_4 \end{pmatrix}. \tag{1.27}$$

The Lagrangian for this doublet of complex scalar fields is described as

$$\mathcal{L} = (\partial_\mu \phi)^\dagger (\partial^\mu \phi) - V(\phi), \tag{1.28}$$
$$V(\phi) = \mu^2 \phi^\dagger \phi + \lambda (\phi^\dagger \phi)^2. \tag{1.29}$$

In $\mu^2 < 0$ case, the potential takes the set of minima at

$$\phi^\dagger \phi = \frac{1}{2}(\phi_1^2 + \phi_2^2 + \phi_3^2 + \phi_4^2) = \frac{v^2}{2} = -\frac{\mu^2}{2\lambda}. \tag{1.30}$$

When the set of fields is arbitrary chosen as $\phi_1 = \phi_2 = \phi_4 = 0$, the Higgs doublet is converted after the symmetry breaking as follows ;

$$\phi = \begin{pmatrix} \phi^+ \\ \phi^0 \end{pmatrix} \to \frac{1}{\sqrt{2}} \begin{pmatrix} 0 \\ v + h(x) \end{pmatrix}. \tag{1.31}$$

The gauge symmetry has broken into SU(2)×U(1)→U(1). The Lagrangian after the symmetry breaking is described replacing the derivatives in Eq. (1.28) by

$$\partial_\mu \to D_\mu = \partial_\mu + i g_W \mathbf{T} \cdot \mathbf{W}_\mu + i g' \frac{Y}{2} B_\mu, \tag{1.32}$$

where $\mathbf{T}$ are the three generators of the SU(2) symmetry and Y is the hypercharge. Then, the first term in the Lagrangian can be written as

$$(D_\mu \phi)^\dagger (D^\mu \phi) = \frac{1}{2}(\partial_\mu h)(\partial^\mu h) + \frac{1}{8} g_W^2 (W_\mu^{(1)} + i W_\mu^{(2)})(W^{(1)\mu} - i W^{(2)\mu})(v+h)^2 \tag{1.33}$$
$$+ \frac{1}{8}(g_W W_\mu^{(3)} - g' B_\mu)(g_W W^{(3)\mu} - g' B^\mu)(v+h)^2. \tag{1.34}$$

Here, the mass terms for the $W^{(1)}$ and $W^{(2)}$ appear as $m_W^2 W_\mu^{(1)} W^{(1)\mu}/2$ and $m_W^2 W_\mu^{(2)} W^{(2)\mu}/2$ respectively, and therefore the mass of W boson is

$$m_W = \frac{1}{2} g_W v. \tag{1.35}$$

From the remaining factors in Eq. (1.34) of $W^{(3)}$ and B, these two fields should satisfy

$$\partial_\mu \partial^\mu \begin{pmatrix} W^{(3)\mu} \\ B^\mu \end{pmatrix} = \frac{v^2}{8} \begin{pmatrix} g_W^2 & -g_W g' \\ -g_W g' & g'^2 \end{pmatrix} \begin{pmatrix} W^{(3)\mu} \\ B^\mu \end{pmatrix}. \tag{1.36}$$

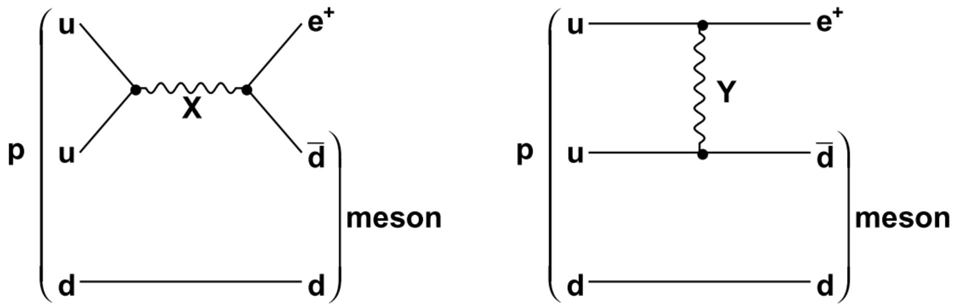

Fig. 1.2: Feynman diagrams of proton decay via X and Y bosons. From [6].

The mass eigenstates and the mass can be obtained by solving this equation

$$\begin{cases} A_\mu = \cos\theta_W B_\mu + \sin\theta_W W_\mu^{(3)}: \quad m_A = 0, \\ Z_\mu = -\sin\theta_W B_\mu + \cos\theta_W W_\mu^{(3)}: \quad m_Z = \frac{1}{2}v\sqrt{g_W^2 + g'^2}, \end{cases} \tag{1.37}$$

where θ_W is the Weinberg angle which satisfies

$$\frac{m_W}{m_Z} = \cos\theta_W. \tag{1.38}$$

Therefore, the GWS theory provide a unified description of electromagnetic and weak interactions and agree well with the experimental results.

1.2 Grand Unified Theories

After the success of electroweak unification, Grand Unified Theories have been proposed to explain the merging of the electroweak and strong interactions. The main idea of the Grand Unified Theories is that the gauge symmetries of SU(2)×U(1) from the electroweak interactions and SU(3) from the strong interaction are incorporated into a global symmetry at high energy scale. In this section, some representative GUT models are introduced.

1.2.1 SU(5) Model

The first GUT with the most simple model, minimal SU(5) model, was proposed by Georgi and Glashow in 1974 [7], where SU(5) is the minimum group covering SU(3)×SU(2)×U(1). 24 independent matrices are defining SU(5), which corresponds to 24 gauge bosons of

$$V_{\mathrm{SU}(5)} = \begin{pmatrix} G_1^1 - \frac{2B}{\sqrt{30}} & G_2^1 & G_3^1 & \bar{X}_1 & \bar{Y}_1 \\ G_1^2 & G_2^2 - \frac{2B}{\sqrt{30}} & G_3^2 & \bar{X}_2 & \bar{Y}_2 \\ G_1^3 & G_2^3 & G_3^3 - \frac{2B}{\sqrt{30}} & \bar{X}_3 & \bar{Y}_3 \\ X^1 & X^2 & X^3 & \frac{W^3}{\sqrt{2}} + \frac{3B}{\sqrt{30}} & W^+ \\ Y^1 & Y^2 & Y^3 & W^- & -\frac{W^3}{\sqrt{2}} + \frac{3B}{\sqrt{30}} \end{pmatrix}, \tag{1.39}$$

where G_i^j is the eight gluons. $W^\pm$, W^3, and B are the gauge bosons for electroweak interactions. X and Y are the new gauge bosons with electric charges of 4/3 and 1/3,

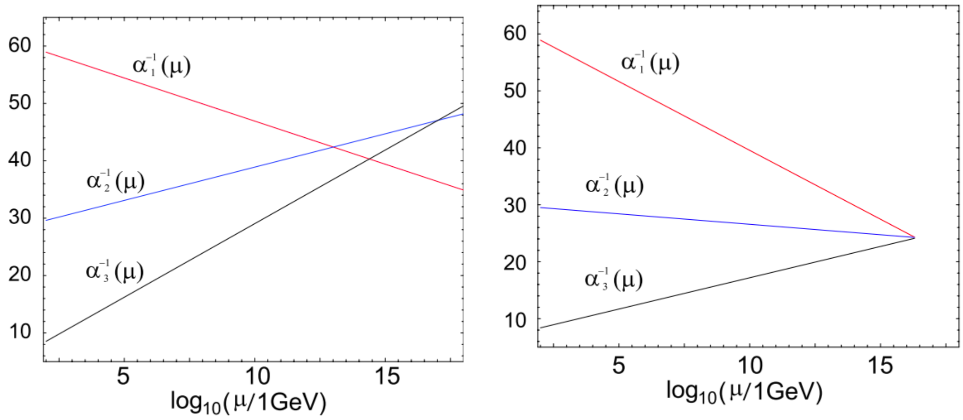

Fig. 1.3: Running coupling constants α_1^{-1}, α_2^{-1} and α_3^{-1} as a function of energy scale in minimal SU(5) and minimal SUSY SU(5) model. From [12].

respectively. The fermions are assigned to the $\bar{\mathbf{5}} + \mathbf{10}$ dimensional representations

$$\bar{\mathbf{5}} = \begin{pmatrix} d_1^c \\ d_2^c \\ d_3^c \\ e \\ -\nu_e \end{pmatrix}, \qquad \mathbf{10} = \begin{pmatrix} 0 & u_3^c & -u_2^c & u_1 & d_1 \\ -u_3^c & 0 & u_1^c & u_2 & d_2 \\ u_2^c & -u_1^c & 0 & u_3 & d_3 \\ -u_1 & -u_2 & -u_3 & u_1 & d_1 \\ -d_1 & -d_2 & -d_3 & -e^c & 0 \end{pmatrix}. \tag{1.40}$$

Since the new bosons X and Y can intermediate quarks and leptons, the baryon and lepton numbers are no longer conserved in SU(5) model. This indicates new interactions where leptons and quarks transform into each other and violating the baryon number. The most distinct phenomenon predicted by GUTs is the nucleon decays with considerably long lifetimes. For example, two quarks in a proton can transform into a lepton and an antiquark mediated by X and Y bosons, and therefore a proton decays into a lepton and a meson as shown in Figure 1.2. The $p \to e^+\pi^0$ is the dominant decay mode in this minimal SU(5) model with a lifetime of $10^{31\pm1}$ years [8]. However, this model was excluded by several experiments [9–11]. The previous experimental approaches are summarized in section 1.3.

1.2.2 SUSY SU(5) Model

One feasible extension of the SU(5) model is made by introducing the Supersymmetry (SUSY) hypothesis. SUSY proposes a new symmetry between fermions and bosons and the existence of the SUSY partner for every particle, all of which have yet to be observed so far. The clear difference between SU(5) and SUSY SU(5) can be seen in the three running coupling constants of electroweak and strong interactions as shown in Fig. 1.3: the three couplings do not meet exactly in a point in SU(5), whereas they completely match at around 2×10^{16} GeV in SUSY SU(5) [13–15]. The dominant proton decay mode in SUSY SU(5) is $p \to \bar{\nu}K^+$. The lifetime limits are expected to be 2.9×10^{30} years for $p \to \bar{\nu}K^+$, and 4.1×10^{33} years for $p \to e^+\pi^0$ [16]. This model had also been excluded by the results from Super-Kamiokande experiment [17].

Tab. 1.1: Predicted branching ratios for proton decay modes into a positron and a meson based on SU(5) and SO(10) models.

	Branching ratio [%]			
	SU(5)			SO(10)
Reference	[22]	[23]	[24]	[25]
$p \to e^+\pi^0$	33	9	35	30
$p \to e^+\eta$	12	3	15	13
$p \to e^+\rho^0$	17	21	2	2
$p \to e^+\omega$	22	56	17	14
others	17	11	31	31

1.2.3 SO(10) Model

Another extension of GUT is to introduce a larger symmetry group containing the SU(3)×SU(2)×U(1) from the Standard Model. One of the plausible models is based on the SO(10) symmetry. In this model, the right-hand neutrino is introduced and all the fermions are embedded into a single representation and the neutrino masses are predicted [18]. The SO(10) symmetry breaks into SU(3)×SU(2)×U(1) intermediated by several symmetries, for example, $\mathrm{SU(4)}\times\mathrm{SU(2)_L}\times\mathrm{SU(2)_R}$ known as the Pati-Salam GUT model [19]. The dominant decay mode id $p \to e^+\pi^0$ with its lifetime ranging from 10^{32} to 10^{39} years [20, 21].

1.2.4 Proton Decay into an Antilepton and a Meson

Although the branching ratio of $p \to e^+\pi^0$ mode dominates in many models, those of the other modes are not negligible. The decay rates of modes with heavy non-strange mesons (η, ρ, ω) are comparable to the modes with pions [22–25]. The branching ratios of the nucleon decay modes into an antilepton and a meson based on SU(5) or SO(10) models are summarized in Tab. 1.1. In addition to $p \to e^+$(meson) modes, $p \to \mu^+$(meson) modes are predicted to occur by the mixing effects between families. In the SU(5) GUT models, the decay rates of modes accompanied by muons are estimated to be [26]

$$\frac{\Gamma(N \to \mu^+(\mathrm{meson}))}{\Gamma(N \to e^+(\mathrm{meson}))} = \frac{\sin{\theta_c}^2 \cos{\theta_c}^2}{(1+\sin{\theta_c}^2)^2+1} = 0.010, \tag{1.41}$$

where θ_c is the Cabbibo angle. The nucleon decays are supposed to occur with such an extremely low probability that the number of expected observation event is one or less for a single channel. Therefore, it is crucial to survey comprehensively across multiple decay modes to enhance the chance of observing proton decay events.

1.3 History of Nucleon Decay Research

The first attempt of proton decay search took place by Goldhaber [30] in 1954. The search was conducted by seeking for the radioactive decay or fission products from the excited state of ^{232}Th after proton decay. The lifetime was concluded to be more than $\sim 10^{20}$ years. This indirect proton decay search had been conducted for several radiochemical materials [31].

At the same time, the searches for nucleon decay by the direct detection of decay products had started. Reins, Cowan and Goldhaber [32] had measured charged particles

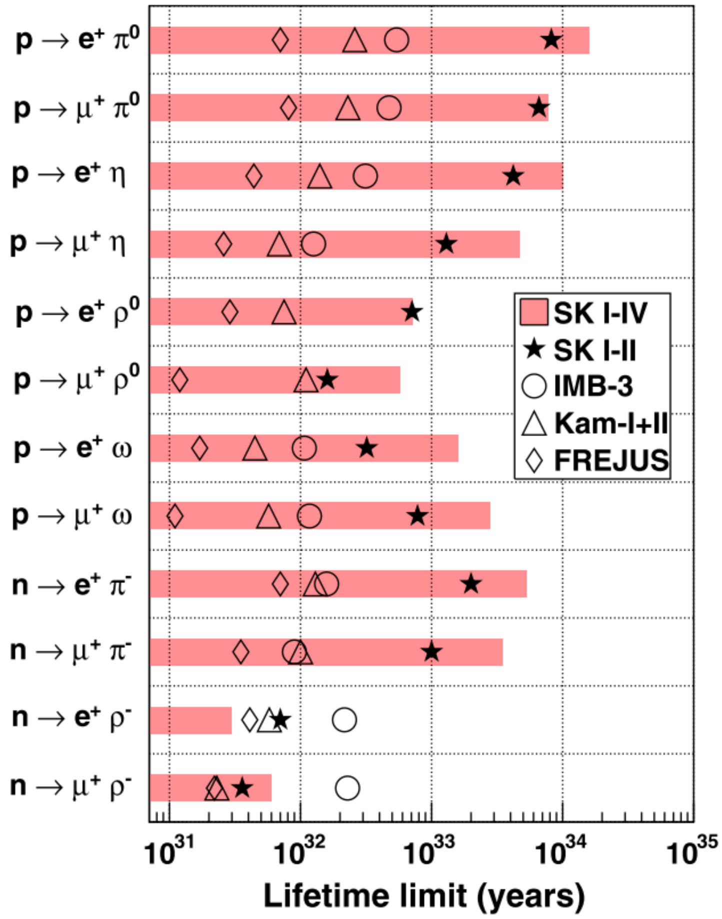

Fig. 1.4: Summary of lower limits of nucleon partial lifetime from several experiments. The experimental results are taken from [9–11, 27, 28]. From [29].

with kinetic energies above 100 MeV from proton decay in 300 liters of liquid scintillator. This experiment set a limit for proton lifetime of $\sim 10^{22}$ years. The experiment was improved in 1958 and updated the limit to $\sim 10^{23}$ years [32].

After the publication of the first GUT in 1974 [7], many nucleon decay experiments were proposed motivated by the prediction of the minimal SU(5) GUT. One of the major experimental ideas was the fine-grained iron calorimeters with alternating layers of iron plates and tracking detectors: the Kolar Gold Field [33], NUSEX [34], Soudan [35], and Frejus [11] experiments. While these detectors showed good performance in energy resolution and particle identification, the volume had limited to a few ktons due to the high cost.

To assure large detector volume with feasible cost, water Cherenkov experiments were contrived. These detectors perform high momentum and direction resolution by detecting the patterns of the Cherenkov ring images. The IMB [10], KAMIOKANDE [9], and Super-Kamiokande (SK) experiment [17, 28, 29] have large fiducial masses of 3.3 kton, 1.0 kton, and 22.5 kton, respectively, compared to the iron calorimeters.

So far many proton decay modes have been searched by several experiments and no evidence has been found. The summary of the proton into an antilepton plus a meson modes are shown as Fig. 1.4.

1.4 Thesis Overview

As described in section 1.2.4, many GUTs predict protons to decay into heavy non-strange mesons (η, ρ, ω) with comparatively large branching ratios to the dominant $p \to e^+\pi^0$ mode. Although these modes were analyzed in the previous study [29] by Super-Kamiokande, there is still room for improvement of proton decay simulation, especially for the modes decay into eta mesons, with additional data exposure of 55.7 kton·years (904.4 live days).

Therefore, this thesis studies the proton decay modes of $p \to e^+\eta,\ \eta \to 2\gamma$ and $p \to \mu^+\eta,\ \eta \to 2\gamma$ by using 0.37 Mton·years exposure of data from Super-Kamiokande. In chapter 2, the overview and event reconstruction algorithm of Super-Kamiokande are described. Then, the Monte Carlo (MC) simulations for proton decay and background events are described in chapter 3. chapter 4 shows the estimation of η nuclear effects in the proton decay simulation. The event selection criteria and the proton decay analysis with final results are represented in chapter 5. Finally, the discussion and conclusion are summarized in chapter 6.

In contrast to the latest publication [29], the cross sections and their uncertainty of nuclear effect of η mesons have been updated. This revise has been applied to the searches where η mesons decay with $\eta \to 2\gamma$ mode of a certain data taking period (SK-IV). The analysis of the other data taking periods (SK-I, II, and III) of $\eta \to 2\gamma$ and other decay mode of η mesons are yet to be updated. Their results are taken from the previous study. The limits of proton lifetime have been calculated by combining the results of revised study of $p \to l^+\eta$, $\eta \to 2\gamma$ for SK-IV period, and the others from the latest publication.

Chapter 2

The Super-Kamiokande Experiment

2.1 The Super-Kamiokande Detector

Super-Kamiokande (SK) is a large water Cherenkov detector whose main purpose is to search for the proton decay. The detector comprises a cylindrical stainless-steel tank with 39.3 m diameter and 41.4 m height, 50 ktons of ultrapure water, and around 13,000 photomultiplier tubes (PMTs) as shown in Fig. 2.1. The detector is placed at 1,000 m underground of Mt. Ikenoyama, in the Kamioka-mine, Hida-city, Gifu Prefecture, Japan. This corresponds to the depth of 2700 m.w.e. and reduces the background cosmic muon flux to 6×10^{-8} cm^{-2}s^{-1}sr^{-1}, a reduction of five orders magnitude compared to the flux on the surface of the Earth. The observed rate of cosmic muon at SK is around 2 Hz.

The detector consists of two sections: the inner detector (ID) and the outer detector (OD) as illustrated in Fig. 2.1. ID is the main detector containing 32 ktons of water and covered by 11,146 of 20-inch PMTs facing inwards, corresponding to around 40% coverage. OD has been mainly used for rejecting cosmic muon events as a veto detector and also as a shield against γ-rays from the surrounding rocks. The outer surface is covered by 1,885 of 8-inch PMTs facing outwards. ID and OD are separated by PET black sheets.

The data taking periods of SK can be divided into four until 2018; SK-I, II, III, and IV. The operation had started on April 1st 1996 and stopped in July 2001 to replace bad PMTs (SK-I). Due to the accident that one of the ID PMTs collapsed to make a shock wave in November 1996, 6,777 ID PMTs and 1,100 OD PMTs were destroyed. Ever since this accident, ID PMTs have been protected by fiber reinforced plastics (FRPs) and acrylic cases. The operation had resumed with 5,182 ID PMTs and 1,885 OD PMTs from October

Tab. 2.1: The summary of SK data taking periods.

		SK-I	SK-II	SK-III	SK-IV
Operation	Start	Apr. 1996	Oct. 2002	Jun. 2006	Sep. 2008
	End	Jul. 2001	Oct. 2005	Sep. 2008	May. 2018
Livetime (days)		1489.2	798.6	518.1	3244.4
Number of PMTs	ID	11,146	5,182	11,129	11,129
	OD	1,885	1,885	1,885	1,885
Photo coverage		40%	19%	40%	40%

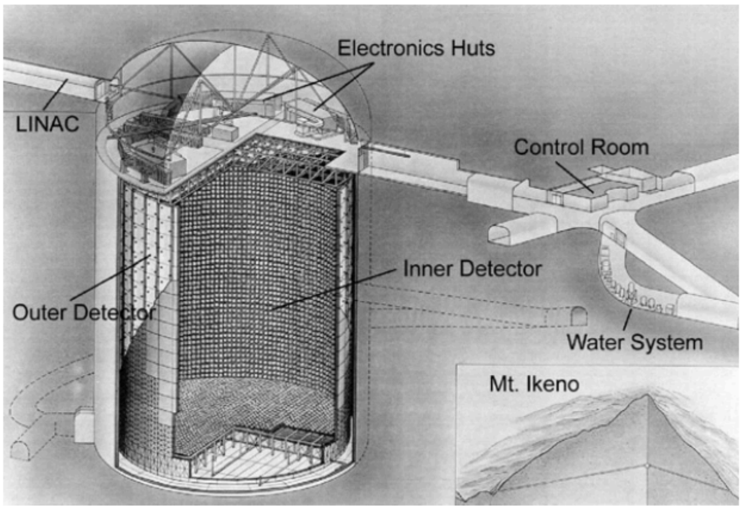

Fig. 2.1: Overview of the Super-Kamiokande detector. From [36].

Tab. 2.2: The summary of Cherenkov momentum thresholds in water.

	e	μ	p
p_{thresh} [MeV/c]	0.57	118	1052

2002 to October 2005 (SK-II). After the replenishment of the rest of the PMTs, the data taking had started with 11,129 ID PMTs from June 2006 to September 2008 (SK-III). In September 2008, the readout electronics and the data acquisition system were upgraded. The SK-IV period had begun at that time and stopped in May 2018, which is the longest data taking period. The features of each period are summarized in Tab. 2.1.

2.1.1 Princeple of the Detector

Super-Kamiokande is capable of observing charged particles by detecting the emitted Cherenkov light with the PMTs. When a charged particle passes through a dielectric medium at a speed greater than that of light, Cherenkov light is emitted in a cone around the direction of the particle with an opening angle of

$$\cos\theta_c = \frac{1}{n\beta}, \tag{2.1}$$

where θ_c is the opening angle, n is the refractive index of the medium, and $\beta = v/c$ is the speed of the particle v divided by the propagation speed of light c. The schematic view of Cherenkov radiation is shown in Fig. 2.2. Here, the charged particle emits the light in the direction of θ_c until it reduces its speed to below the speed of light. Therefore, the light is projected on the wall as a ring, which is called the Cherenkov ring. The momentum threshold for the Cherenkov radiation is

$$p_{\text{thresh}} = \frac{mc\beta_{\text{thresh}}}{\sqrt{1-\beta^2_{\text{thresh}}}}, \quad \text{with} \quad \beta_{\text{thresh}} = \frac{1}{\text{n}}, \tag{2.2}$$

and the thresholds for various particles in water (n=1.34) are summarized in Tab. 2.2. The opening angle is around 42° for particles travelling at $\beta \sim 1$ in water.

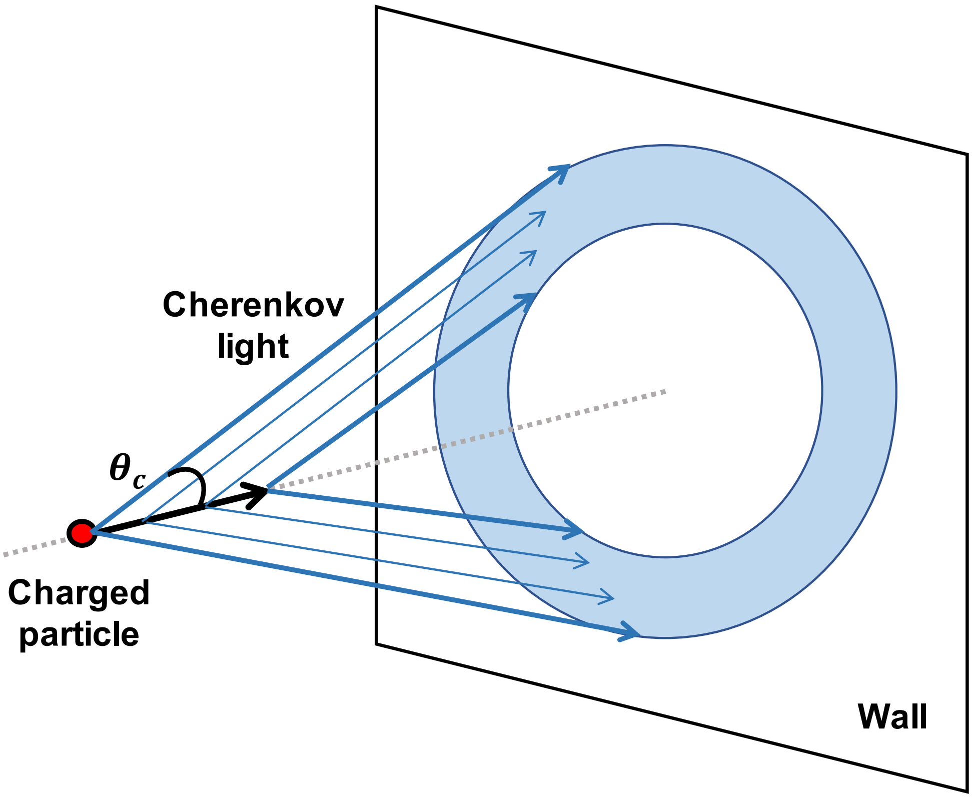

Fig. 2.2: Outline drawing of Cherenkov light.

The spectrum of Cherenkov light as the number of emitted photons N per wavelength λ per unit travel length x is given by the following formula

$$\frac{d^2N}{d\lambda dx} = \frac{2\pi\alpha}{\lambda^2}\left(1 - \frac{1}{n^2\beta^2}\right), \tag{2.3}$$

where α is the fine structure constant. When 300 nm $\leq \lambda \leq$ 600 nm, around 340 photons are emitted per unit cm by a charged particle with $\beta \sim 1$ in water.

2.1.2 Photodetection

(1) Photosensors

20-inch PMTs with 11-stage Venetian blind type dynodes (R3600) manufactured by Hamamatsu Photonics K. K. are used for ID detectors. Figure 2.3 shows the structure of a 20-inch ID PMT. The bialkali (Sb-K-Cs) photocathodes are adopted and the quantum efficiency peaks at 22% at the wavelength of 360 nm as shown in Fig. 2.4. The typical specifications of ID PMTs are summarized in Tab. 2.3.

8-inch PMTs (R1408) are used for OD detectors. The details of this PMT are described in [37].

(2) Electronics and Data Acquisition

Due to the upgrade of SK in 2008, the electronics and data acquisition systems of SK-IV are different from those of SK-I, II, and III. The electronic circuit modules used for SK-I

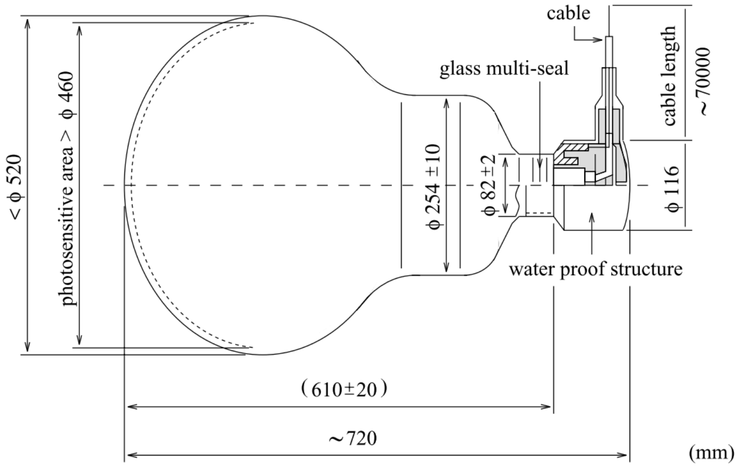

Fig. 2.3: Schematic view of a 20-inch ID PMT.

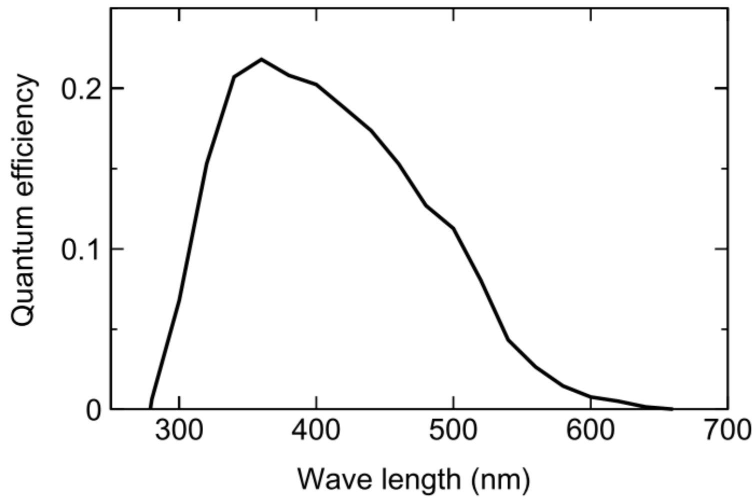

Fig. 2.4: Quantum efficiency of the photocathode as a function of wavelength.

Tab. 2.3: Specifications of the 20-inch ID PMTs.

Photocathode material	Bialkali (Sb-K-Bs)
Quantum efficiency	22% at $\lambda = 360$ nm
Dynode structure	11-stage Venetian blind type
Operation high voltage	1700 - 2000 V
Gain	10^7 at 2000 V
Dark current	200 nA at 10^7 gain
Dark rate	3 kHz at 10^7 gain with 0.25 p.e. threshold
Transit time	90 ns at 10^7 gain
Transit time spread	2.2 ns (1σ)

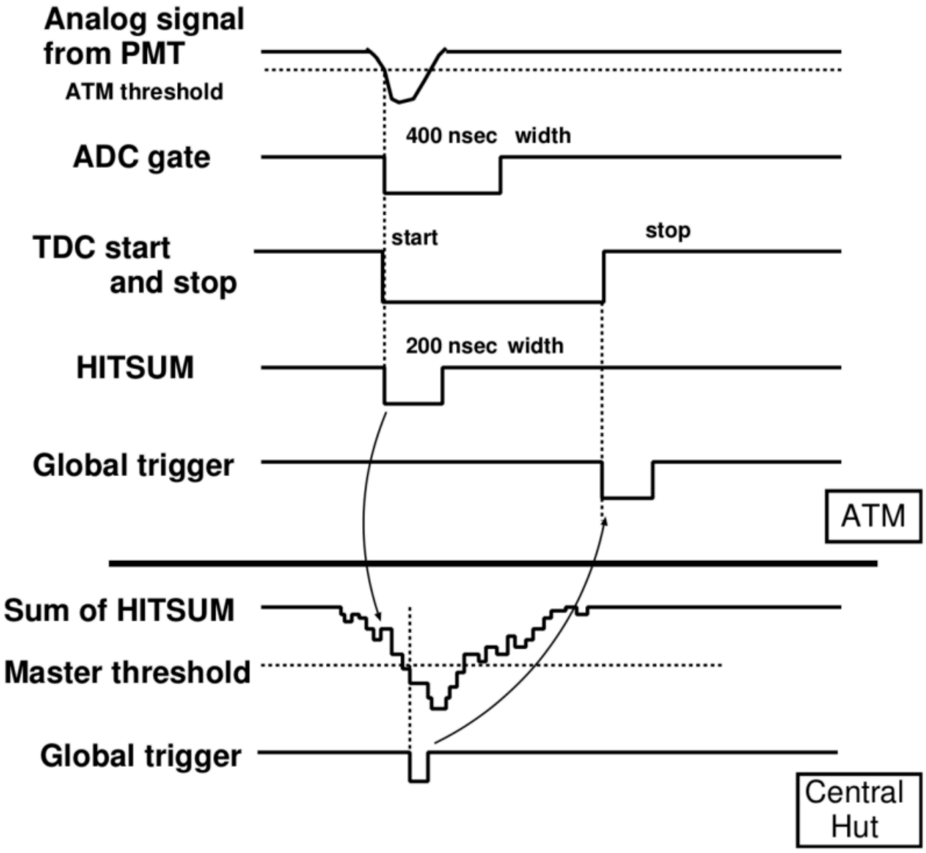

Fig. 2.5: Timing chart of ATM operation in SK-I to SK-III. From [38].

to SK-III period are called ATM for ID and OD QTC for OD with hardware triggers. For SK-IV, QBEE circuits are used for both ID and OD with software trigger.

Systems for SK-I to SK-III The timing chart of ID trigger for SK-I to SK-III is shown in Fig. 2.5. The ATM (Analog Timing Module) records and digitizes the integrated charge and the arrival time information for each PMT signal with Analog-to-Digital Converter (ADC) and Time-to-Digital Converter (TDC). One ATM module processes 12 ID PMT signals. The input PMT signals of each ID PMTs are divided into four by a current splitter. One of the four signals is input into a discriminator and a rectangular pulse would be output if the signal is a hit. Then, the event trigger (global trigger) is issued by the sum of the rectangular pulse (HITSUM) from all of the ID PMTs. In this system, three types of event triggers are used depending on the energy; the super low energy (SLE), low energy (LE), and high energy (HE) triggers. Once the event trigger happens, each ATM starts to digitize and record the information in internal memory buffers.

For OD PMTs, the signals are processed by charge-to-time converter modules in a similar way to the ATM system. The details of electronics and data acquisition for SK-I to SK-III periods are described in [36].

System for SK-IV To improve the problems of dead time and cable reflection of ATMs, a new electronic module QBEE [39] was developed and installed for ID and OD PMTs

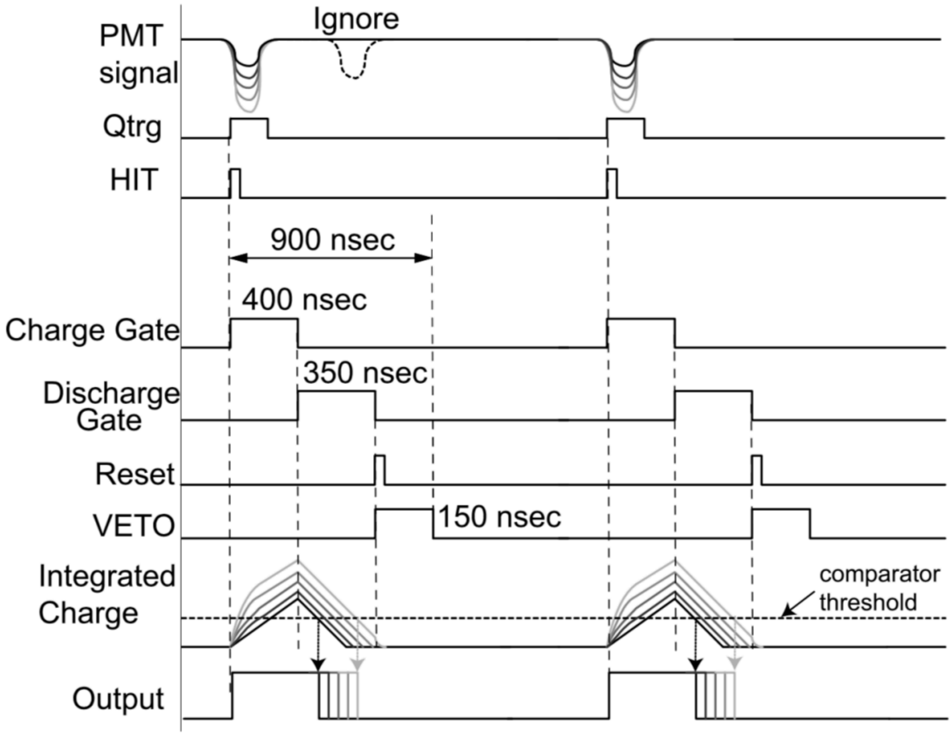

Fig. 2.6: Timing chart of QTC operation QBEE for SK-IV. From [39].

since SK-IV period. One QBEE consists of 24 channels. The charge of a PMT signal is integrated by a Charge-to-Time Converter (QTC), and then the QTC output is converted into a digitized time and charge by a TDC in each channel. Figure 2.6 shows the timing chart of QTC. One distinct feature compared to the previous system of SK-I, II, and III is the acquisition of timing information. In QBEE modules, the charge integrated by QTC is discharged as constant current. By measuring the discharging time, QTC output signals contain both charge and timing information. Thanks to this new method, QBEE enables to record events with no dead time. Another modification had been made in the trigger system. Unlike the hardware trigger in ATM, a software trigger is issued when the number of PMT hits exceeds the threshold. In addition to the SLE, LE, and HE triggers, special high energy (SHE) and “after trigger (AFT)” triggers were newly installed for a neutron tagging algorithm, which is described in section 2.2.6.

2.1.3 Water Purification

To achieve high detection efficiency of Cherenkov light, it is essential to keep high transparency of the water to avoid the light being absorbed or scatted. In addition, removing radioactive materials, especially radon from bedrocks, is crucial to reduce the background events. For these reasons, 50 ktons of water in the tank is constantly reprocessed by a water purification system with the flow rate of around 35 ton/hour.

2.2 Event Reconstruction

The event reconstruction processes are applied to data sets to derive information of physics quantities, such as the number of Cherenkov rings, momentum, particle identification, charge, and time information of PMTs. The APfit reconstruction scheme is used in this analysis and applied for both SK data and MC events. Here, the overview of the APfit is described in this section and the details can be found in [40].

The reconstruction algorithm proceeds as the following steps.

1. Vertex fitting
2. Ring Counting
3. Particle Identification
4. Momentum Reconstruction
5. Michel Electron Finding
6. Neutron Tagging for SK-IV

The neutron tagging is applied only for data and MC events for SK-IV because it requires the updated electronics.

2.2.1 Vertex Fitting

The reconstruction process starts from determining the vertex position of the observed event. This process consists of three steps: point fit, ring edge search, and TDC fit.

Point Fit Firstly, the vertex position is roughly estimated by assuming that the Cherenkov light has been emitted from a single point. The fitting is proceeded on the basis that the timing residual ((photon arrival time)-(time of fight)) distribution should peak at the true vertex position. The goodness of fit G is therefore defined as

$$G = \frac{1}{N} \sum_i \exp\left(-\frac{(t_i - t_0)^2}{2(1.5\sigma)^2}\right), \tag{2.4}$$

where N is the number of hit PMTs, t_i is the time of flight subtracted timing of i-th PMT, t_0 is the interaction time chosen to maximize the goodness, and σ is the PMT timing resolution of 2.5 ns. The factor 1.5 is chosen to optimize the fitting performance.

Ring Edge Search Secondly, the algorithm estimates the direction and the edge of the most energetic Cherenkov ring. The opening angle of the ring edge θ_{edge} has been defined as the angle satisfying

$$\frac{d^2\text{PE}(\theta)}{d^2\theta} = 0, \tag{2.5}$$

where $\text{PE}(\theta)$ is the angular distribution of the observed charge as a function of opening angle θ. Figure 2.7 shows the typical $\text{PE}(\theta)$ distribution and the θ_{edge}. The direction is evaluated by the estimator $Q(\theta_{\text{edge}})$ defined as

$$Q(\theta_{\text{edge}}) = \frac{\int_0^{\theta_{\text{edge}}} \text{PE}(\theta)\ \text{d}\theta}{\sin\theta_{\text{edge}}} \times \left(\left.\frac{d\text{PE}(\theta)}{d\theta}\right|_{\theta=\theta_{\text{edge}}}\right)^2 \times \exp\left(-\frac{(\theta_{\text{edge}} - \theta_{\text{exp}})^2}{2\sigma_\theta^2}\right), \tag{2.6}$$

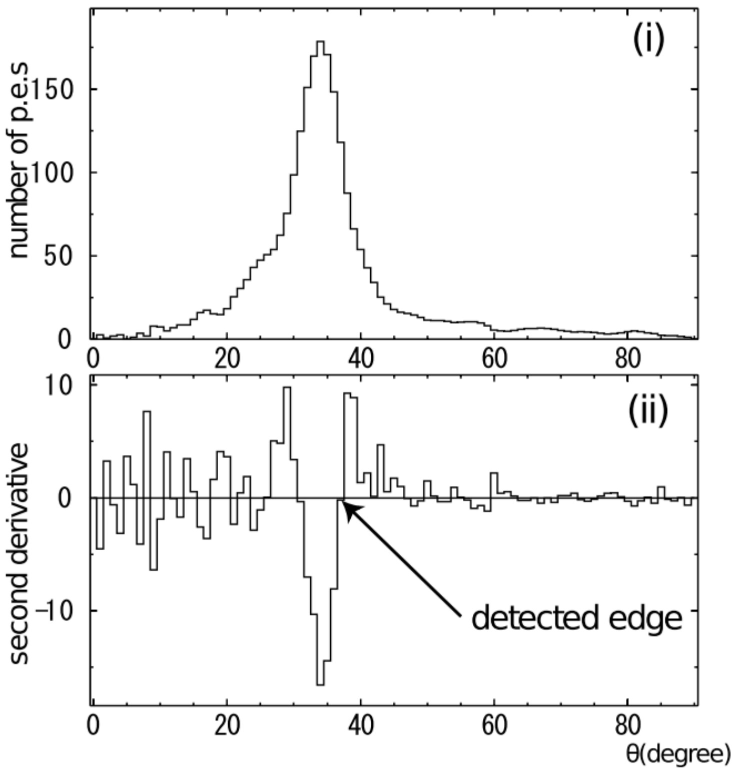

Fig. 2.7: An observed charge distribution as a function of Cherenkov opening angle (top) and its second derivative (bottom). From [39].

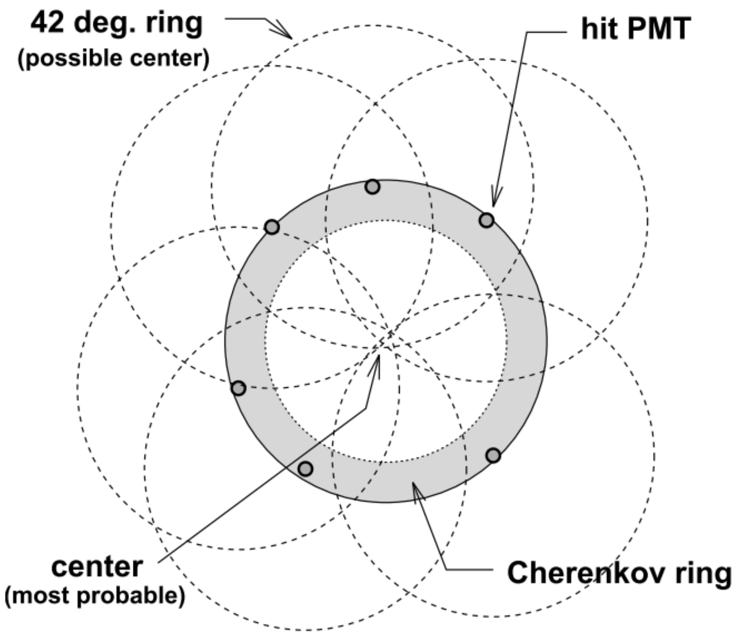

Fig. 2.8: An outline drawing of detecting additional rings. The shaded and dashed circles stand for the Cherenkov ring and rings with 42° half angles. From [39].

where θ_{exp} is the expected Cherenkov opening angle calculated from total charge inside θ_{edge} and σ_θ is its resolution. Q_{edge} is calculated by changing the particle direction around the initial direction derived from point fit and the direction that maximizes Q_{edge} is chosen.

TDC Fit Finally, the precise vertex position is determined from the information of the track of a charged particle and the scattered Cherenkov photons. The track length is estimated by the total charge with an expectation of 3 MeV/cm energy deposit. The residual of observed and expected photon arrival timings are calculated differently for PMTs inside and outside the ring edge. PMTs inside the edge mostly detect the photons directly, whereas PMTs outside observe scattered photons or reflected light from the wall. Therefore, the timing residuals for PMTs inside the ring edge are calculated by considering that Cherenkov light is emitted with the same angle along the track. For PMTs outside the edge, on the other hand, the timing was modulated by the time of flight of Cherenkov light from the vertex with scattering parameters. By evaluating the goodness for PMTs inside and outside respectively by Eq. (2.4), the vertex position is re-estimated precisely.

2.2.2 Ring Counting

After determining the vertex position and the most energetic Cherenkov ring, additional Cherenkov rings are investigated by ring counting algorithm.

The Hough transformation [41], a feature extraction technique, is used to search for the Cherenkov ring candidates. Figure 2.8 shows the basic concept of finding additional rings. The shaded ring in shows the Cherenkov ring projected to the detector wall. The dashed circles represent virtual circles with 42° half angles centered at the hit PMTs. The center of the Cherenkov ring is defined as the intersection point of these dashed circles and thereby the direction can be estimated. Then, a log likelihood method judges whether this

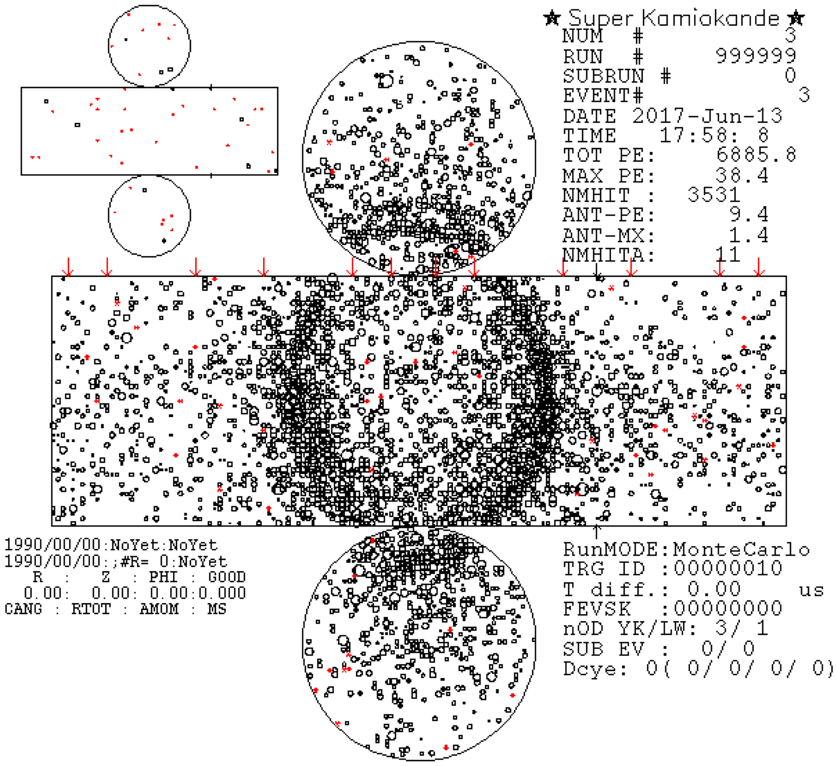

Fig. 2.9: Typical shower-like (e-like) ring pattern.

candidate ring is true or fake. This likelihood is calculated by the expected and observed charge inside the tested ring.

2.2.3 Particle Identification

Next, the particle identification (PID) process runs to classify the Cherenkov rings into two types: a shower-like (e-like) or a non-shower-like (μ-like). Electrons and γ-rays produce diffused and blurred Cherenkov ring patterns as shown in Fig. 2.9 because of the effects of electromagnetic showering and multiple scattering. These rings are identified as e-like. On the other hand, muons and charged pions create μ-like rings with sharper ring edges as shown in Fig. 2.10. In addition, the Cherenkov rings of electrons and γ-rays have opening angles of ~ 42 °, while those of μ-like rings vary depending on the momenta and energy losses. By using these differences, the PID algorithm identifies whether the ring is e-like or μ-like. The PID consists of two processes: expected charge distribution and determination of particle types.

Expected Charge Distribution Firstly, the expected charge in each PMT is calculated. The expected charge distribution in the i-th PMT from an electron $q_i^{\mathrm{exp}}(e)$, and

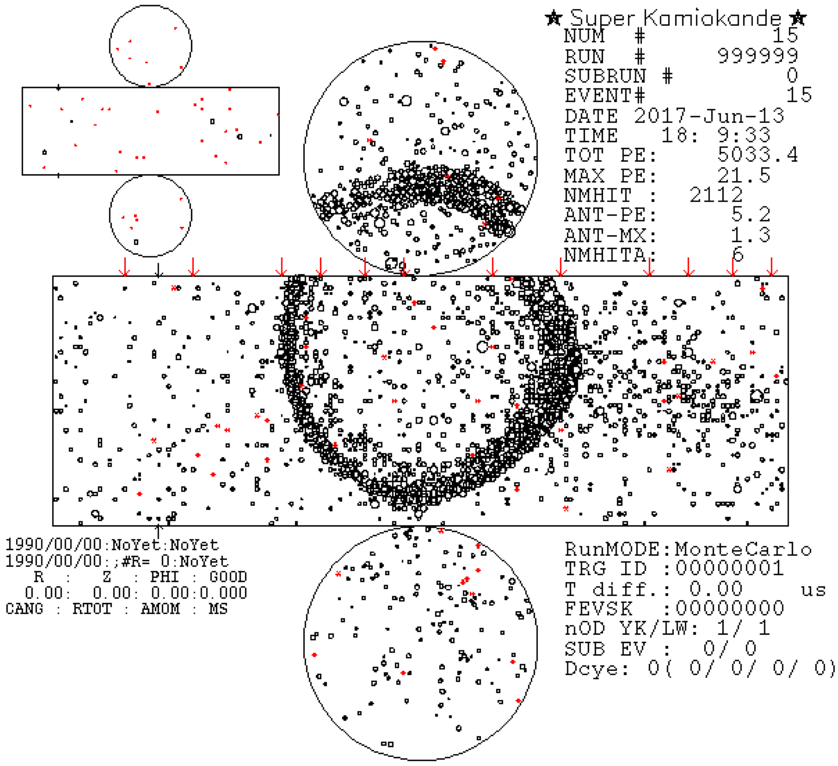

Fig. 2.10: Typical non shower-like (μ-like) ring pattern.

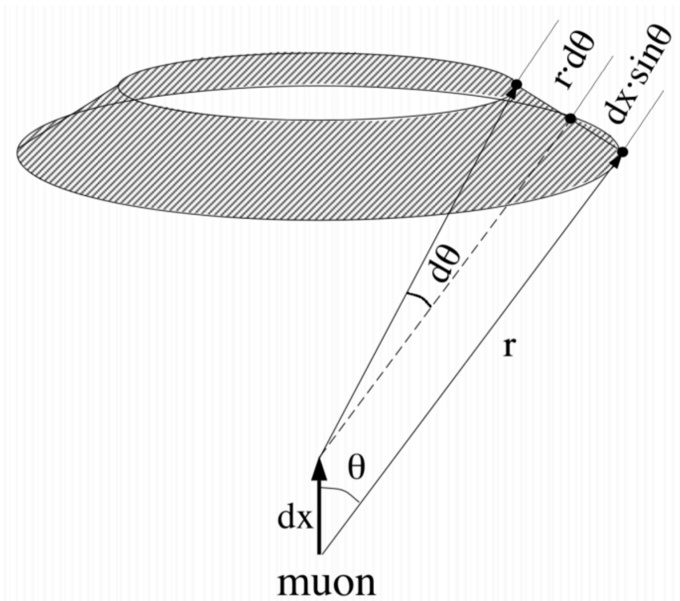

Fig. 2.11: Area where photons are emitted by a muon. From [42].

from a muon $q_i^{\exp}(\mu)$ are estimated by

$$q_i^{\exp}(e) = \alpha_e Q^{\exp}(p_e, \theta_i) \left(\frac{R}{r_i}\right)^{3/2} e^{-r_i/L} f(\Theta_i) + q_i^{\mathrm{scat}}, \tag{2.7}$$

$$q_i^{\exp}(\mu) = \left(\frac{\alpha_\mu \sin^2 \theta_{x_i}}{r_i \left(\sin\theta_{x_i} + r_i \left. \frac{d\theta}{dx} \right|_{x=x_i} \right)} + q^{\mathrm{knock}} \right) e^{-r_i/L} f(\Theta_i) + q_i^{\mathrm{scat}}, \tag{2.8}$$

where

$\alpha_e,\ \alpha_\mu$: normalization factor

$Q^{\exp}(p_e, \theta_i)$: expected charge distribution depending on the electron momentum and the angle θ_i for the i-th PMT

R: virtual sphere radius (16.9 m)

r_i: distance from the vertex to the i-th PMT

L: light attenuation length in water

$f(\Theta_i)$: angular acceptance as a function of the photon injection angle Θ_i for the i-th PMT

q_i^{scat}: expected charge due to scattering light for the i-th PMT

θ_{x_i}: Cherenkov angle of a muon track length at x

q_i^{knock}: expected charge due to knock-on electrons for the i-th PMT

$Q^{\exp}(p_e, \theta_i)$ distribution has been obtained by MC simulation. The term $\sin^2\theta_{x_i}$ in Eq. (2.8) comes from the angular dependence of Cherenkov light intensity and the term $r(\sin\theta + r(d\theta/dx))$ arises from the area where photons are emitted as shown in Fig. 2.11.

Determination of Particle Types The likelihood for the n-th ring is defined as

$$L_n(e \text{ or } \mu) = \prod_{\theta_i < (1.5\times\theta_c)} prob\left(q_i^{\mathrm{obs}},\ q_{i,n}^{\exp}(e \text{ or } \mu) + \sum_{n' \neq n} q_{i,n'}^{\exp} \right), \tag{2.9}$$

where $q_{i,n}^{\exp}$ is the expected charge distribution from the n-th ring assuming its particle as an electron (Eq. (2.7)) or a muon (Eq. (2.8)) and q_i^{obs} is the observed charge in the i-th PMT. Here, the function *prob* gives the probability to detect q_i^{obs} when $q_i^{\exp}$ is estimated and defined as

$$prob(q^{\mathrm{obs}}, q^{\exp}) = \frac{1}{\sqrt{2\pi}\sigma} \exp\left(-\frac{(q^{\mathrm{obs}} - q^{\exp})^2}{2\sigma^2} \right), \tag{2.10}$$

where σ is the resolution for $q_{\exp}$. The likelihood L_n is optimized by changing the direction and the opening angle of the n-th ring to take the maximum value. Then, L_n is converted into the form of a probability to determine the particle type from the ring pattern as

$$P_n^{\mathrm{pattern}}(e \text{ or } \mu) = \exp\left(-\frac{\{\chi_n^2(e \text{ or } \mu) - min[\chi_n^2(e),\ \chi_n^2(\mu)]\}}{2\sigma_{\chi_n^2}^2} \right), \tag{2.11}$$

$$\chi_n^2(e \text{ or } \mu) = -2\log L_n(e \text{ or } \mu) + \text{constant}, \tag{2.12}$$

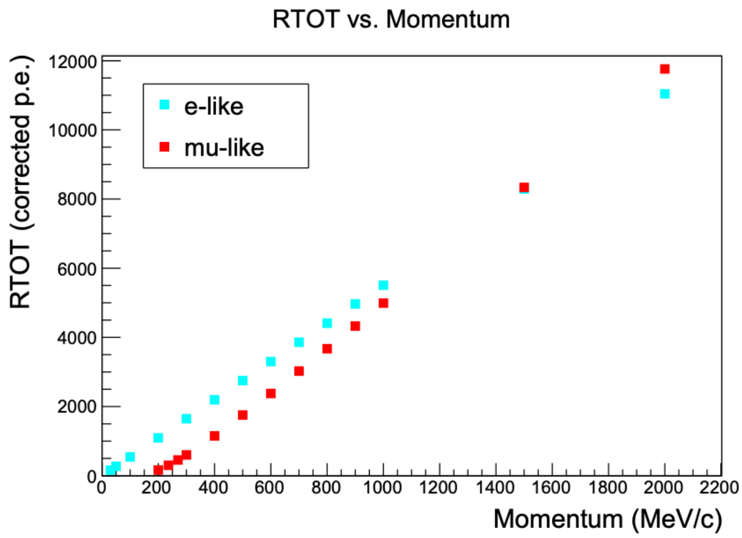

Fig. 2.12: Distributions of RTOT and true momentum up to 2000 MeV/c for both e-like and μ-like rings. From [43].

where the resolution of χ^2 distribution is given as $\sigma_{\chi^2_n} = \sqrt{2N}$ and N is the number of PMTs used in the calculation. The probability coming from the Cherenkov opening angle is defined as

$$P_n^{\text{angle}}(e \text{ or } \mu) = \exp\left(-\frac{(\theta_n^{\text{obs}} - \theta_n^{\text{exp}}(e \text{ or } \mu))^2}{2(\delta\theta_n)^2}\right), \tag{2.13}$$

where θ_n^{obs} and $\delta\theta_n$ are the reconstructed Cherenkov opening angle of the n-th ring and its fitting error, respectively, and $\theta_n^{\text{exp}}(e \text{ or } \mu)$ is the expected opening angle estimated by the reconstructed momentum assuming the particle as an electron or a muon. A probability function was thus calculated by taking into account both the probabilities of the ring pattern and the opening angle,

$$P(e, \mu) = P^{\text{pattern}}(e, \mu) \times P^{\text{angle}}(e, \mu). \tag{2.14}$$

At last, the type of the particle is determined by

$$P_{\text{PID}} \equiv \sqrt{-\log P(\mu)} - \sqrt{-\log P(e)}. \tag{2.15}$$

The Cherenkov ring is classified as e-like when $P_{\text{PID}} < 0$ and as μ-like when $P_{\text{PID}} > 0$.

2.2.4 Momentum Determination

The momentum of each ring is evaluated by the observed charge inside the 70° half-angle cone towards the ring direction. With the modification of the light attenuation in water and the angular acceptance of the PMTs, the total charge from the n-th ring RTOT$_n$ is calculated as

$$\text{RTOT}_n = \frac{G_{\text{MC}}}{G_{\text{data}}}\left[\alpha \times \sum_{\theta_{i,n}<70^\circ}\left(q_{i,n} \times \exp\left(\frac{r_{i,n}}{L}\right) \times \frac{\cos\Theta_i}{f(\Theta_i)}\right) - \sum_{\theta_{i,n}<70^\circ} S_i\right], \tag{2.16}$$

where

α: normalization factor

$G_{\mathrm{data}}, G_{\mathrm{MC}}$: relative PMT gain parameter for cosmic muon data and MC

$\theta_{i,n}$: opening angle between the i-th PMT the n-th ring direction

t_i: TOF subtracted hit timing of the i-th PMT

S_i: expected charge of the i-th PMT due to scattering light

Figure 2.12 shows the linear relationship between RTOT and true momentum. RTOT is converted to the corresponding momentum depending on the PID by conversion table made from MC.

2.2.5 Michel Electron Finding

The Michel electrons, decayed electrons from muons, are a significant indicator of the existence of muons. These electrons are tagged by searching hit clusters after the primary Cherenkov ring event around ~ 1 μs. As around 20% of μ^- are absorbed by the nucleus and do not emit decay electrons, the Michel electron tagging efficiency of μ^- is lower than that of μ^+. Moreover, the efficiency is higher for SK-IV than SK-I, II, and III periods because of the elimination of dead time in the electronics. The tagging efficiency is $\sim 80\%$ for μ^+ and $\sim 65\%$ for μ^- for SK-I to SK-III, and $\sim 95\%$ for μ^+ and $\sim 80\%$ for μ^- for SK-IV.

2.2.6 Neutron Tagging for SK-IV

Atmospheric neutrino interactions often produce neutrons, whereas nucleus after proton decay and hydrogen atoms seldom emit neutrons. Therefore, the neutron tagging is significant for distinguishing proton decay events from the background.

Neutrons travelling through water get captured by hydrogen nucleus and emit deexcitation γ-rays of 2.2 MeV with the probability of 100% by the reaction

$$n + p \to d + \gamma \ (2.2 \text{ MeV}). \tag{2.17}$$

The mean travelling time was measured to be 204.87 μs. The produced neutron can be tagged by detecting this 2.2 MeV γ-ray.

First, PMT hits from dark noise is removed. Due to the scintillation light from radioactive isotopes in the PMT glass, dark noise appears in PMTs with a time constant of around 10 μs. Therefore, the dark noise events are removed by rejecting the PMT hits which had recorded another hit within 10 μs. Then, the candidate hit cluster from 2.2 MeV γ-ray is sought by setting conditions to the number of PMT hits within a 10 ns sliding window after the prompt neutrino interaction. Finally, 16 variables that represent the characteristics of the candidate cluster are calculated and input into a neural network to classify into the real and fake clusters. The neutron tagging efficiency is 25.2% with a mistagging rate of 1.8%. The details of neutron tag technology can be found in [44, 45]

2.3 Accumulated Data of Super-Kamiokande

In this study, only the events with their reconstructed vertices and all the visible particles inside the Fiducial Volume (FV) are used for the proton decay analysis. These events are called Fully Contained (FC) events, and the FV is defined as the region 2 m away from the inner detector wall with 22.5 ktons of water. Besides FC events, there are Partially Contained (PC) and Upward Going Muon (UPMU) events. The former corresponds to events with their vertices inside FV but charged particles go outside, and the latter derives from high energy muon generated by upward-going neutrinos interacting with the bedrocks. Most of the FC events are produced from atmospheric neutrinos. So as to extract the FC data set, events which are not induced by atmospheric neutrinos, for example, cosmic muons, radioactivities from materials around the detector, electronic noise, and flashing PMTs, are excluded by imposing conditions on the number of hits, observed charges of ID and OD PMTs, and so on. Out of around 10^6 events accumulated in SK in a single day, ~ 8 events are extracted as FC events.

Chapter 3

Event Simulation

In order to evaluate the signal detection efficiency for the $p \to l^+\eta$ proton decay events, a dedicated simulation has been developed. Firstly, in section 3.1, the processes taken in place in SK followed by the proton decay events are discussed. Besides, the atmospheric neutrino simulation has been contrived to estimate the expected number of background events in section 3.2. As a summary, in section 3.3, the overall detector simulation scheme is described.

3.1 Proton Decay Simulation

In the SK, proton decay events are assumed to occur both in hydrogen nuclei as free protons and in oxygen nuclei as bound protons with a ratio at one to four in the H_2O molecule system. The probabilities of the proton decays are considered to be the same regardless of their initial state. The $p \to l^+\eta$ proton decay events are treated as two body decays. While in the proton decay events from free protons a positron (an antimuon) and an η meson are emitted back-to-back direction with a monochromatic momentum of 310.0 MeV/c (297.7 MeV/c) in the $p \to e^+\eta$ ($p \to \mu^+\eta$) decay, in bound protons the momentum of the decay products have distributions due to the Fermi motion, and η mesons can react with residual nucleons in the originating nuclei. In this work, these effects from oxygen isotopes were taken into account in the simulation as the steps described in the

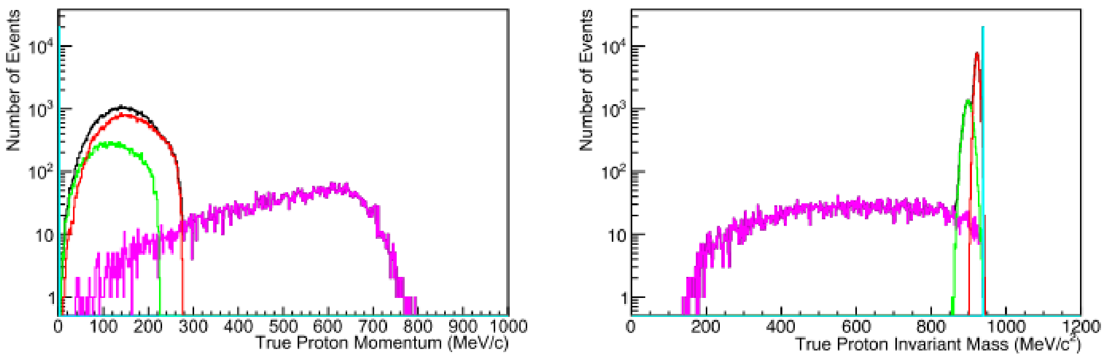

Fig. 3.1: Distributions for simulated momentum (left) and invariant mass (right) after the proton decay events. The cyan, black, green, red, and purple histograms correspond to free, bound, s-state, p-state, and correlated decay protons, respectively [46].

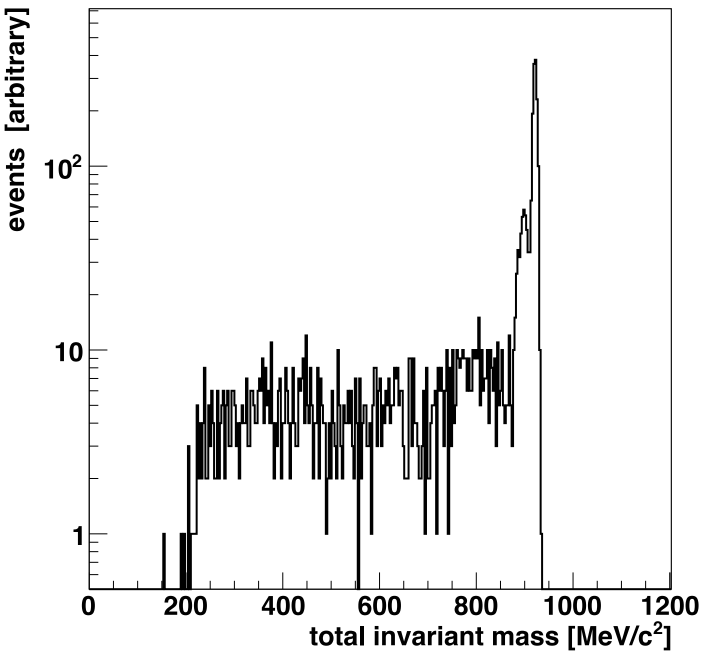

Fig. 3.2: Invariant mass distribution of the decayed proton in ^{16}O for $p \to e^+\eta$ MC. The peaks around 900 MeV/c^2 and 940 MeV/c^2 corresponds to s-state and p-state, and the tail in the low momentum region stands for peaks from correlated decays.

following paragraphs.

3.1.1 Fermi Motion of Nucleons

Firstly, the Fermi motion and the nuclear binding energy in ^{16}O should be evaluated for bound protons. The proton momentum in ^{16}O are simulated based on the measured and calculated nucleon momentum and nuclear binding energy in ^{12}C nucleus from an electron scattering experiment on ^{12}C [47]. The simulated proton momentum distributions for both the s-state and p-state of ^{16}O are shown in Fig. 3.1. The nuclear binding energies are 39.0 MeV for the s-state and 15.5 MeV for the p-state. This effect is taken into account by subtracting the binding energy from the proton rest mass.

3.1.2 Correlated Decay

Second, the decaying protons can be affected by the other nucleons in the same ^{16}O nucleus by their wave function overlapping. In this case, the proton decays as a three body decay, and its momentum changes. This event is called the correlated decay, predicted to occuer with a probability of $\sim$ 10% from [48]. Fig. 3.2 shows the invariant mass distribution of decaying protons from $p \to e^+\eta$ MC in ^{16}O. The lower tail corresponds to correlated decays where the invariant masses are smaller than proton mass due to the invisible momentum of the recoiling nucleon.

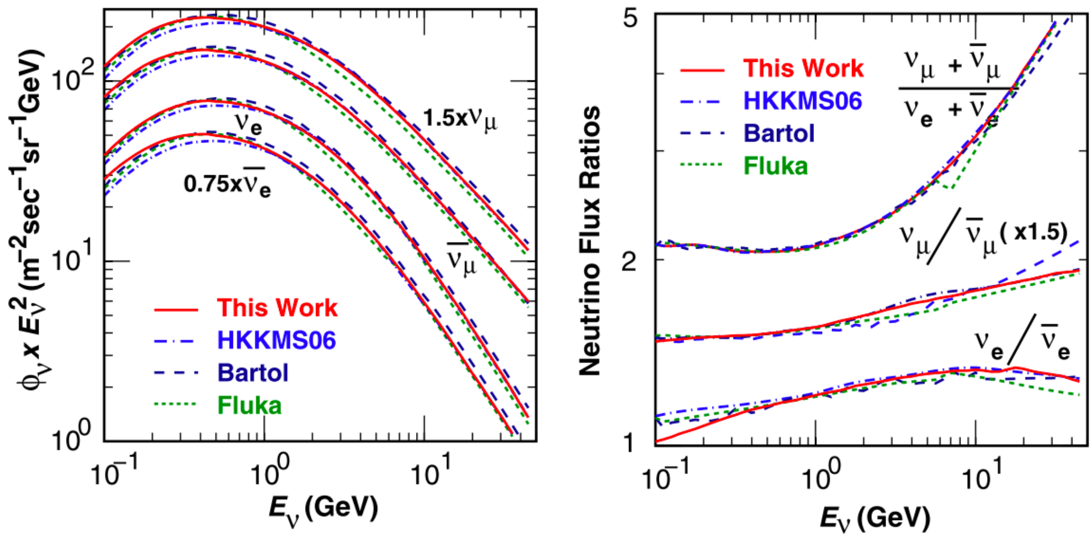

Fig. 3.3: Direction-averaged atmospheric neutrino flux at SK calculated by the Honda flux. The flux averaged over all direction is on the left and the flux ratio is on the right. From [50].

3.1.3 η Nuclear Effect

Finally, the η mesons generated by bound protons in ^{16}O nucleus can interact with nucleons until escaping from the nucleus (η nuclear effect). The decaying proton position in ^{16}O nucleus is given by the Woods-Saxon nuclear density model [49] as

$$\rho(r) = \frac{\rho(0)}{1 + \exp\left(\frac{r-a}{b}\right)}, \tag{3.1}$$

where $\rho(0)$ is the average density of nuclei, a and b are the the maximum radius and the surface thickness of ^{16}O nucleus, respectively. The η mesons are considered to be emitted from this position. The details of the η nuclear effect are discussed in section 4.

3.2 Background Simulation

The background for proton decay search in SK is the events derived from the atmospheric neutrino interactions since the signals can be similar to those of proton decay events. The simulation events for atmospheric neutrino are created, and the number of background events is calculated by simulating atmospheric neutrino flux and the neutrino interactions.

3.2.1 Atmospheric Neutrino Flux

The atmospheric neutrino flux in the event simulation is calculated by the Honda flux from [50, 51]. The Honda flux has been estimated based on the measured primary cosmic ray fluxes in AMS [52] and BESS [53] experiments. The effects of solar wind and geomagnetic field are taken into account. Interactions of the primary cosmic ray with air nuclei are simulated based on JAM [54] for energies of the primary cosmic rays below 32 GeV and DPMJET-III [55] for above 32 GeV. Finally, the flux of atmospheric neutrinos is acquired from the decays of pions, kaons, and the secondary particles from air nuclei.

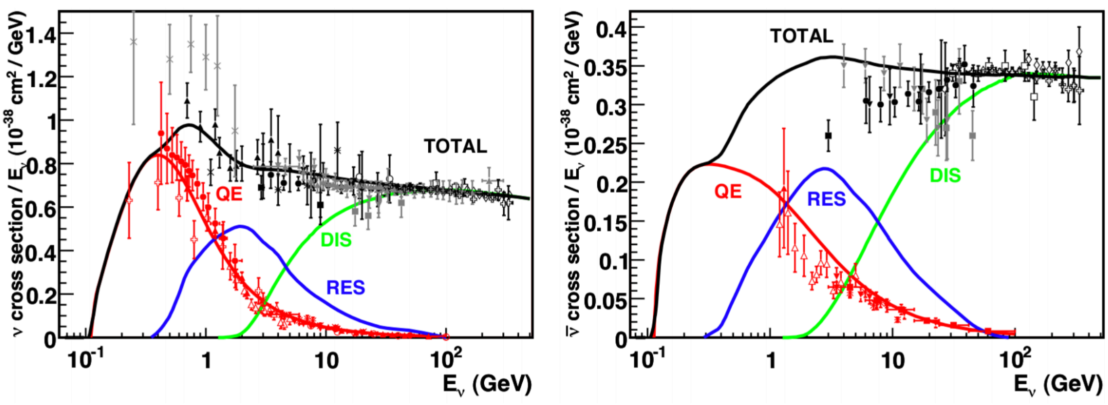

Fig. 3.4: The simulated cross sections for ν ($\bar{\nu}$) interactions in NEUT with data. The red, blue, green, and black solid lines correspond to (quasi-)elastic scattering, single π, K, η, γ production, deep inelastic scattering, and the total of three interactions. From [44].

Figure 3.3 shows the atmospheric neutrino flux averaged over all direction at SK by the Honda flux together with other flux models from FLUKA [56] and the Bartol [57]. The dominant background events for proton decay search are neutrinos with 1 GeV order energy.

3.2.2 Neutrino Interactions

The atmospheric neutrinos interact with the nucleons in the SK tank. These interactions are simulated by NEUT [58]. The interactions considered in the atmospheric neutrino MC events are as follows for both Charged Current (CC) and Neutral Current (NC):

CC/NC elastic and quasi-elastic scattering $\nu + N \rightarrow l + N'$

CC/NC single π production $\nu + N \rightarrow l + N' + \pi$

CC/NC single K production $\nu + N \rightarrow l + N' + K$

CC/NC single η production $\nu + N \rightarrow l + N' + \eta$

CC/NC single γ production $\nu + N \rightarrow l + N' + \gamma$

CC/NC deep inelastic scattering $\nu + N \rightarrow l + N'$+hadrons

CC/NC coherent pion production $\nu + {}^{16}\mathrm{O} \rightarrow l + {}^{16}\mathrm{O} + \pi$

where ν is a neutrino, N and N' are the initial and final nucleons, and l is a lepton (neutrino for NC and charged lepton for CC interaction). The distributions for the simulated cross sections of neutrino interactions in NEUT are shown in Fig. 3.4.

(1) Elastic and Quasi-Elastic Scattering

For NC elastic scattering interaction, a neutrino is scattered by a nucleon without generating any particle. In CC quasi-elastic scattering interaction (CCQE), on the other hand, a neutrino converts into a corresponding charged lepton. The CCQE cross sections for free protons are calculated by the model in [60] in the simulation. For the interactions in

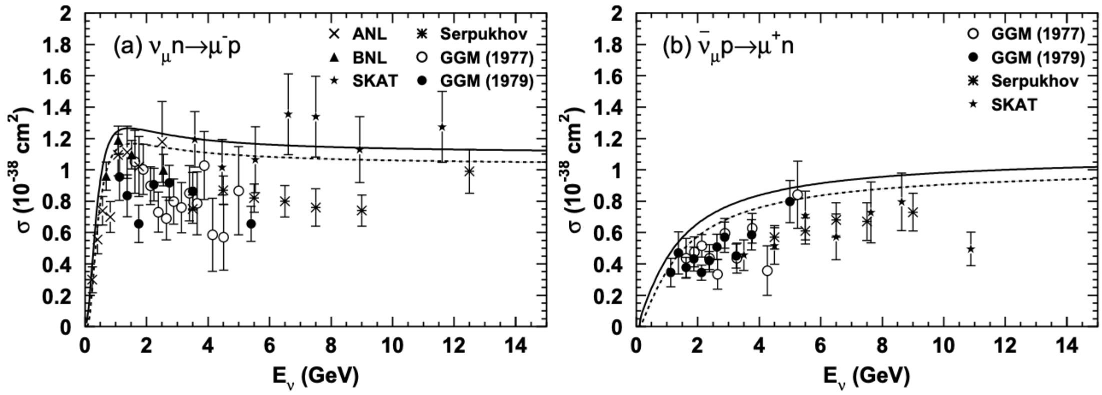

Fig. 3.5: Calculated cross sections of CCQE scattering with experimental data as the function of neutrino energy. The solid and dashed lines show the calculated cross sections for free and bound targets. From [59].

bound nucleons in ^{16}O, the effects of the Fermi motion and the Pauli exclusion principle are evaluated by [61]. The cross section of NC elastic scattering are estimated by adopting the relations as follows [62, 63]:

$$\sigma(\nu p \to \nu p) = 0.153 \times \sigma(\nu n \to e^- p) \tag{3.2}$$

$$\sigma(\bar{\nu} p \to \bar{\nu} p) = 0.218 \times \sigma(\bar{\nu} p \to e^+ n) \tag{3.3}$$

$$\sigma(\nu n \to \nu n) = 1.5 \times \sigma(\nu p \to \nu p) \tag{3.4}$$

$$\sigma(\bar{\nu} n \to \bar{\nu} n) = 1.0 \times \sigma(\bar{\nu} p \to \bar{\nu} p) \tag{3.5}$$

Figure 3.5 shows the calculated cross sections of CCQE scattering with experimental data.

(2) Single Meson and Gamma Production

Single meson of π, K, and η and a γ-ray can be produced through the nucleon resonance state N^*:

$$\nu + N \to l + N^* \tag{3.6}$$

$$N^* \to N' + (\pi, K, \eta, \gamma) \tag{3.7}$$

Single pion production has been simulated by the Rein-Sehgal Model [64]. The cross section is obtained by the amplitudes of each resonance production and the rate of each resonance decaying into a pion and a nucleon. The cross sections for the other production interactions have been calculated by changing the decay rates corresponding to the generated particle. The estimated cross sections of $\nu + N \to l + N' + \pi$ interactions are shown in Fig. 3.6.

(3) Deep Inelastic Scattering

In the energy region of over 10 GeV, deep inelastic scattering becomes the dominant neutrino interaction. Neutrinos with such high energies can interact with a quark comprising a nucleon and produce multiple hadrons. The cross section of deep inelastic scattering has been calculated by following the theory from [65]. In the region of $W < 2.0$ GeV/c^2, only the pions are considered as produced hadrons, and its multiplicity is estimated from the

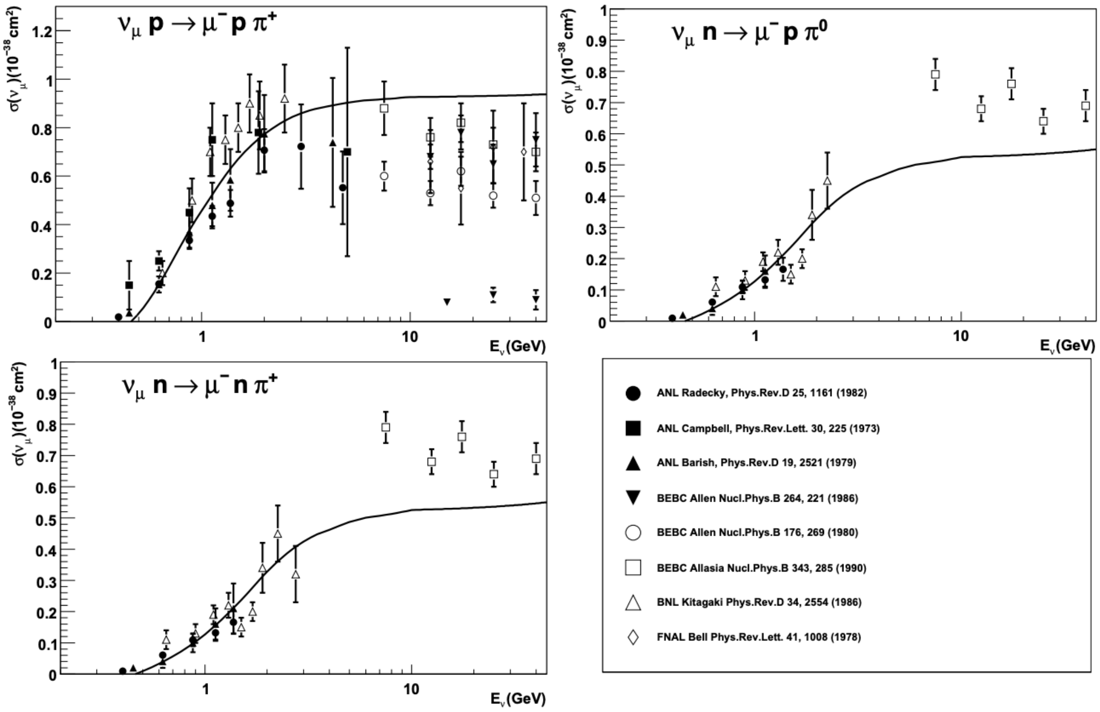

Fig. 3.6: Calculated cross sections of $\nu + N \to l + N' + \pi$ interactions with data as the function of neutrino energy. From [59].

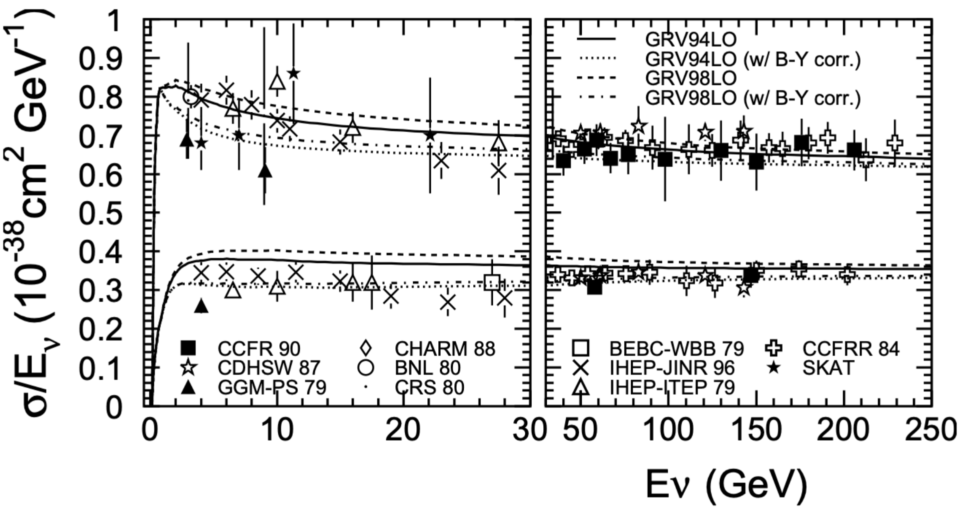

Fig. 3.7: Total CC interactions of CCQE scattering, single meson production, and deep inelastic scattering with data as the function of neutrino energy. The upper (lower) lines corresponds to ν_μ ($\bar{\nu}_\mu$). From [59].

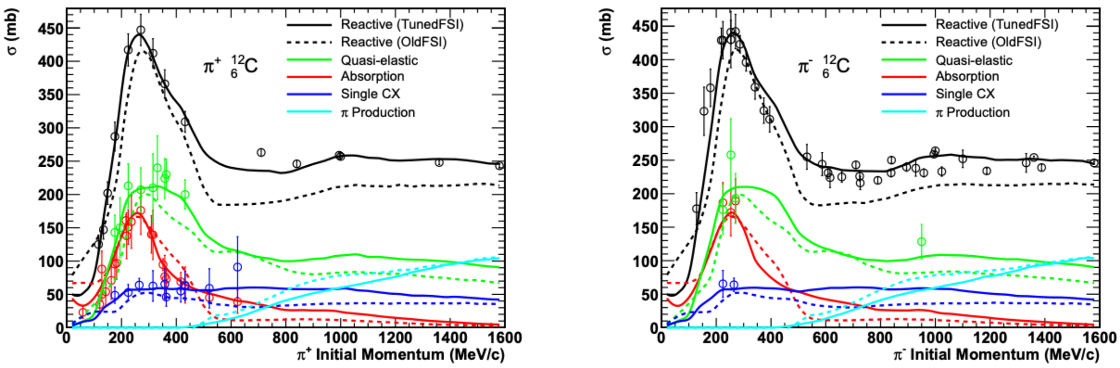

Fig. 3.8: Measered and NEUT simulated cross sections of $\pi^+ - {}^{12}$C scattering (left) and of $\pi^+ - {}^{12}$C scattering (right) as a function of pion momentum. From [69].

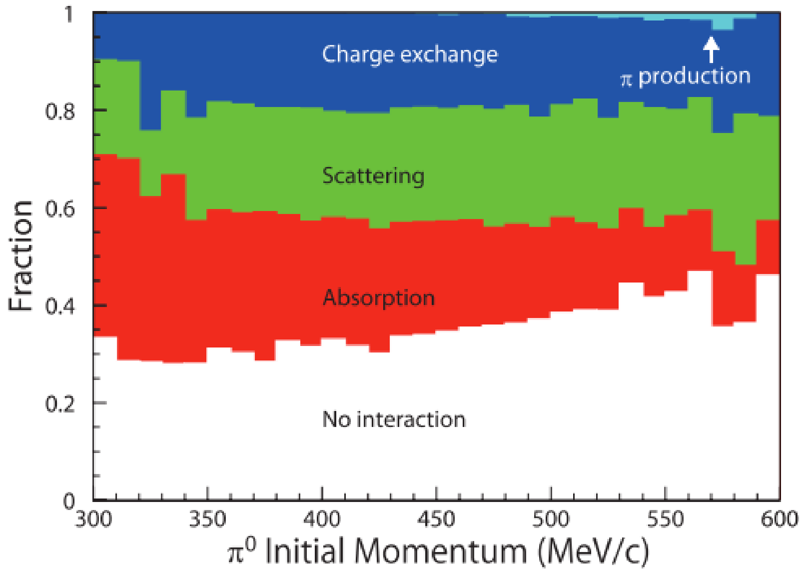

Fig. 3.9: Fraction of final state of pion interaction as a function of pion momentum. From [28].

results of bubble chamber experiments [66,67]. The calculated cross sections for total CC interactions of the CCQE scattering, single meson production, and deep inelastic scattering with data are shown in Fig. 3.7. The productions of K and η mesons are treated in the region $W > 2.0$ GeV/c^2 by PHYTIA/JETSET simulation package [68].

(4) Coherent Pion Production

Neutrinos can interact with oxygen nuclei followed by a charged pion production. The pion is emitted in the forward direction as little momentum is transferred to the oxygen nucleus. This interaction is called the coherent pion production, and has been simulated by Rein-Sehgal [64].

3.2.3 π Nuclear Effect

The pions induced by atmospheric neutrino interactions are the dominant background source. These pions can interact with nucleons in ^{16}O nucleus in a similar way to the η

nuclear effect: pions can be scattered, absorbed, or charge exchanged by π nuclear effect. The cross sections for each interaction are calculated by the cascade model of [70] by NEUT [58] with data from various $\pi-(p,n)$ and $\pi-N$ scattering experiment [69]. Due to the Pauli exclusion principle, the nucleon momentum after π nuclear effect needs to be larger than the Fermi surface momentum of

$$p_F(r) = \left(\frac{3}{2}\pi^2\rho(r)\right)^{\frac{1}{3}}, \tag{3.8}$$

where $\rho(r)$ is given by Eq. (3.1). Figure 3.8 shows the measured and NEUT simulated cross sections of $\pi^{\pm}$-^{12}C scattering. The cross sections of $\pi^{\pm}$-^{16}O scattering, based on the measured and simulated cross sections of $\pi^{\pm}$-^{12}C scattering, are adopted for generating simulation events for atmospheric neutrinos. The fraction of the final state of pion interaction is shown in Fig. 3.9.

3.3 Detector Simulation

The particles generated through the proton decay and atmospheric neutrino events are simulated by a GEANT3 based simulation package SKDETSIM. The particle propagation in water, Cherenkov photon emission, and the response of PMTs and electronics are simulated by SKDETSIM.

The Cherenkov photon propagation has been simulated by considering the Rayleigh/Mie scattering and absorption by H_2O molecule. The Rayleigh scattering, caused by small particles ($r \ll \lambda$, where r is the radius of a particle), dominates when photons have relatively short wavelengths of ($\lambda \leq 450$ nm). The scattering coefficient dependence of λ^{-4} make photons scatter symmetrically in the forward and backward directions. For longer wavelength ($\lambda \geq 450$ nm), the dominant process is the absorption by H_2O molecule. Besides, the Mie scattering is caused by large particles ($r \gg \lambda$) to scatter photons more intensely in the forward than in the backward. These scattering effects tuned by calibration data have been evaluated in the simulation package.

Chapter 4

Evaluation of η Meson Nuclear Effect

The process of η mesons absorbed immediately after proton decay events brought the biggest uncertainty to determine the lifetime of the protons decaying into $p \to l^+\eta$ modes. In this work, the reaction cross section between η mesons and nuclei has been updated from the previous research [29]. The cross section had been studied from an experimental work deducing the photoproduction cross sections of η mesons. In section 4.1, the elementary interaction processes and the detection schemes of η mesons in Super-Kamiokande are described. To estimate the uncertainty of the cross section, the η photoproduction reactions are discussed in section 4.2. From the obtained differential cross sections of η photoproduction reactions and the measured η absorption cross sections, the cross sections of the η nuclear effect have been evaluated by a minimum chi-square method as discussed in section 4.3.

4.1 Reaction Processes of η Mesons in Super-Kamiokande

η mesons produced from oxygen atoms through the proton decay modes $p \to l^+\eta$ occasionally interact while travelling within the nucleus to escape from it. Since this nuclear effect plays a crucial role in proton decay search in that affecting the number of observable η mesons, it is necessary to get a reliable estimation of the ηN reaction cross sections.

4.1.1 Internal Nuclear Effect

η mesons interact with nucleons and can form several baryon resonance states. The $S_{11}(1535)$ resonance state is studied exclusively due to the property that it exists slightly

Tab. 4.1: Decay mode and the branching ratio of the $S_{11}(1535)$ resonance state. Numbers are taken from [71].

Decay mode	Branching ratio[%]
$N\pi$	42
$N\eta$	42
$N\rho \to N\pi\pi$	13
$\Delta\pi \to N\pi\pi$	3

Tab. 4.2: Decay modes and the branching ratios of η mesons. Numbers are taken from [71].

Decay modes	Branching ratios[%]
2γ	39.41 ± 0.20
$3\pi^0$	32.68 ± 0.23
$\pi^+\pi^-\pi^0$	22.92 ± 0.28
$\pi^+\pi^-\gamma$	4.22 ± 0.08

above the ηN threshold providing a large branching ratio of $S_{11}(1535) \to N + \eta$ [72, 73]. Therefore, the η nuclear effect is evaluated through $S_{11}(1535)$ resonance state in this study.

$$\eta + N \longrightarrow S_{11}(1535), \tag{4.1}$$
$$S_{11}(1535) \longrightarrow N + meson(\eta, \pi, \pi\pi). \tag{4.2}$$

The decay modes of $S_{11}(1535)$ state in Eq. (4.2) and their branching ratios from [71] are listed in Tab. 4.1.

4.1.2 Decay Modes of Survived η Mesons

The main decay modes of η mesons and their branching ratios are shown in Tab. 4.2. In this thesis, only the proton decay sequence into the $p \to l^+\eta$, $\eta \to 2\gamma$ modes are studied due to the largest decaying branching ratio of η mesons and their highest signal efficiencies, as discussed in section 5.1.1, above all the decay modes of η mesons.

4.2 η Photoproduction Reaction

In order to confirm the cross section of η nuclear effect, σ_{nuc}, and its uncertainty, the photoproduction reaction of η meson is utilized. The measured differential cross sections of η photoproduction reaction $d\sigma_{\eta\text{photo}}/dp$ from an experiment conducted at Mainz [73] are compared with the simulated values from an phenomenological fitting of σ_{nuc} to verify the assumption.

4.2.1 Experiment at Mainz

The experiment conducted by MAMI accelerator facility at Mainz Germany in 1996 [73] measured the differential cross sections of photoproduction reaction of η mesons, $d\sigma_{\eta\text{photo}}/dp$, by injecting γ-rays with energies of $E_\gamma = 735 - 765$ MeV into a ^{12}C target. The produced η mesons were identified by reconstructing the invariant masses from the two γ-rays emerging from the $\eta \to 2\gamma$ decay. Figure 4.1 shows the measured $d\sigma_{\eta\text{photo}}/dp$ along with the laboratory momentum of η mesons of $p = 0 - 600$ MeV/c. The total systematic error for each $d\sigma_{\eta\text{photo}}/dp$ plot was estimated to be 6%, mainly coming from the uncertainty of detection efficiency.

4.2.2 Simulation of η Photoproduction Reaction with η Nuclear Effect

The overview of the process of η photoproduction with a ^{12}C target is illustrated in Fig. 4.2. Firstly, the elementary process of this reaction is the η photoproduction reactions

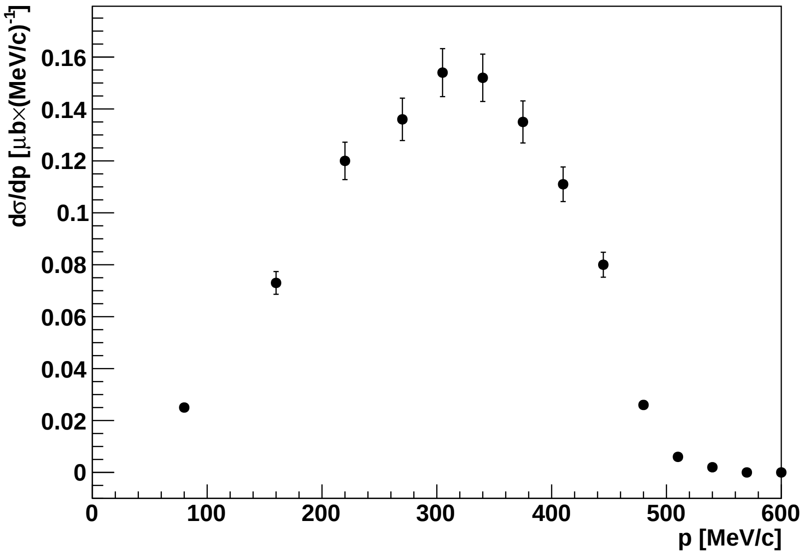

Fig. 4.1: Measured differential cross sections of photoproduction of η mesons in the laboratory system on a ^{12}C target identified by γ-rays with energies of $E_\gamma = 735 - 765$ MeV. Data is taken from [73].

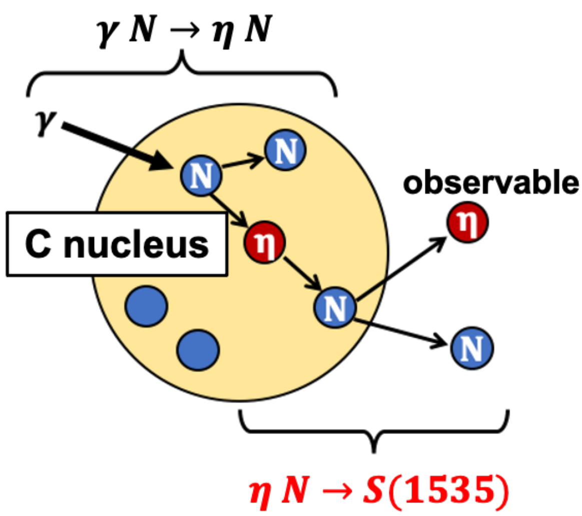

Fig. 4.2: Image of how the simulation of η photoproduction with a ^{12}C target proceeds. The red, blue, and yellow circles stand for η mesons, nucleons, and ^{12}C nucleus, respectively. This figure illustrates when an η meson is scattered by nuclear effect while propagating through the nucleus.

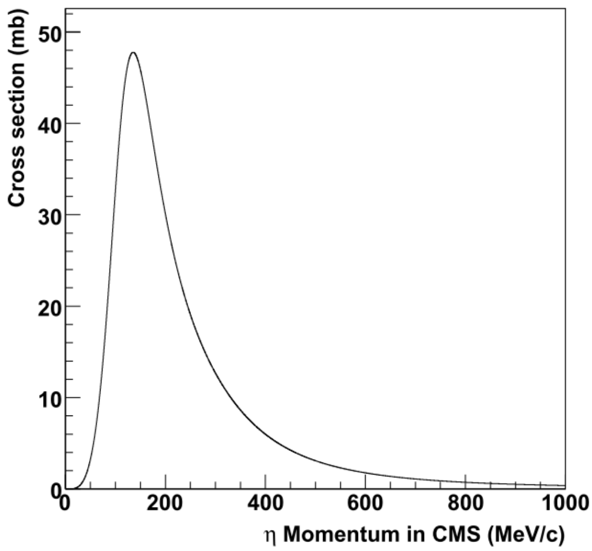

Fig. 4.3: Calculated cross section of η nuclear effect, $\sigma_{\mathrm{nuc}}^{\mathrm{prev}}$, from $\mathrm{S}_{11}(1535)$ resonance state by the Breit-Wigner formula. From [6].

at nucleons, creating an η meson with a γ ray striking a nucleon in the nucleus:

$$\gamma p \to \eta p, \tag{4.3}$$

$$\gamma n \to \eta n. \tag{4.4}$$

The differential cross sections of the η photoproduction on a proton target (Eq. (4.3)) are calculated by the Scattering Analysis Interactive Dial-in (SAID) program [74]. The SAID provides data and the solutions of partial wave analysis of hadron elastic and charge-exchange scatterings. The contribution of the neutrons in the photoproduction cross sections is assumed to be 2/3 of that with a proton target from the results of η photoproduction measurement experiment with a deuteron target [75]. Secondly, η mesons generated by these reactions propagate through the ^{12}C nucleus, and this propagation is simulated by the cross section of η nuclear effect, σ_{nuc}, within a simulation package, NEUT [58]. As only the η mesons which can escape from nucleons without being absorbed are observed, the cross section of the η photoproduction reaction on a ^{12}C target can be estimated by the number of these escaped η mesons.

In the previous study [6,29], σ_{nuc} and its uncertainty were estimated by simulating the η photoproduction cross section in a ^{12}C nucleus by σ_{nuc} in this way and comparing to the measured cross section in [73].

4.2.3 Systematic Uncertainties in the Previous Study

The cross section of the η nuclear effect in the previous study [6,29], $\sigma_{\mathrm{nuc}}^{\mathrm{prev}}$, was calculated by the Breit-Wigner Formula:

$$\sigma_{\mathrm{nuc}}^{\mathrm{prev}} = \frac{\pi}{k^2}\frac{\Gamma_{\eta N}(\Gamma_{\mathrm{total}} - \Gamma_{\eta N})}{(E_{\mathrm{CMS}} - M_{\mathrm{res}})^2 + \Gamma_{\mathrm{total}}^2/4}, \tag{4.5}$$

where E_{CMS} is the energy of η-N in the center of mass frame, M_{res} is the mass of the resonance state $S_{11}(1535)$, and Γ_{total} is the total width of $S_{11}(1535)$ resonance taken

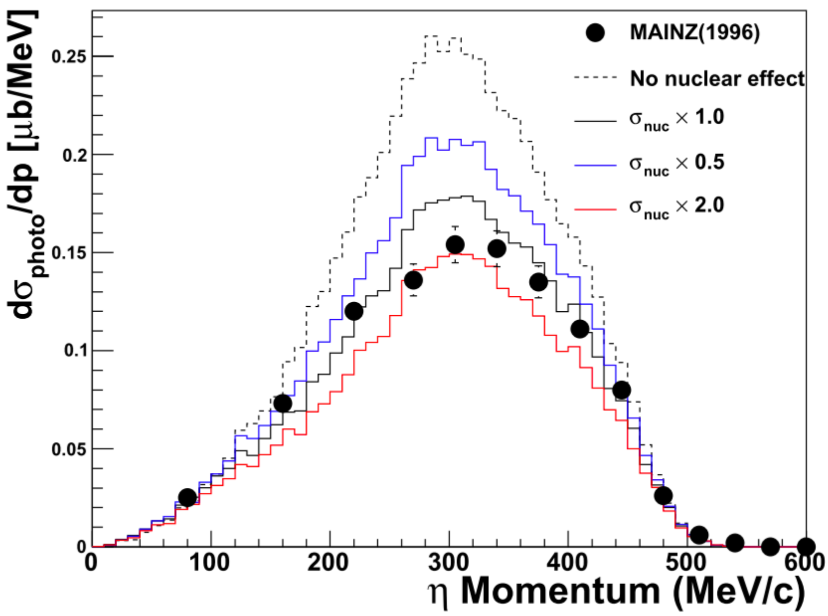

Fig. 4.4: Measured and simulated differential cross sections of photoproduction of η mesons according to Breit-Wigner formula on a ^{12}C target with γ-rays with energies of $E_\gamma = 735 - 765$ MeV. The experimental data from Mainz experiment [73] are shown with black circles. The dashed line indicates the cross-section without η nuclear effect, and the black, blue, and red solid lines show the simulated cross sections when they were multiplied by 100%, 50%, and 200%, respectively. From [6].

Tab. 4.3: Fraction of the final states of η meson after the proton decay of $p \to l^+\eta$ in ^{16}O with the η nuclear effect deduced from the Breit-Wigner formula. From [6].

η nuclear effect in ^{16}O nucleus	default $\sigma_{\rm nuc}^{\rm prev}$	$\sigma_{\rm nuc}^{\rm prev} \times 0.5$	$\sigma_{\rm nuc}^{\rm prev} \times 2$
no interaction	56%	73%	43%
scattered	6%	4%	5%
absorbed	38%	23%	53%

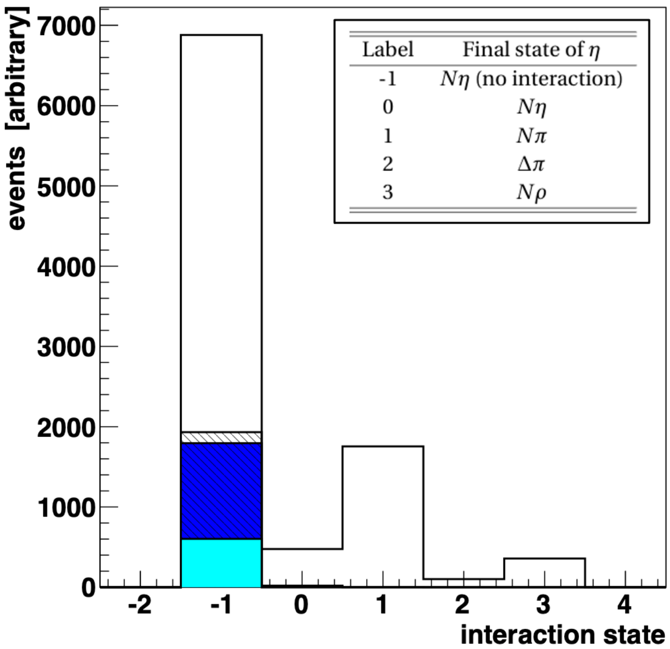

Fig. 4.5: Distributions of the final state of η mesons of the $p \to e^+\eta$ MC events. The black shaded histogram shows the contribution from free proton decay events only. The blue and cyan histograms show the fractions of events that can be reconstructed and identified as proton decays originating from all protons and free protons, respectively. The final interaction states in the x-axis are described the top right table. The number of events in the bins of the blue histogram from left to right are 1757, 26, 0, 0, 0, and 0.

from [71], $\Gamma_{\eta N} = \Gamma_{\text{total}} \times \text{BR}(\eta N)$ is the partial width of $S_{11}(1535) \to \eta N$ estimated as the product of Γ_{total} and the branching ratio of $S_{11}(1535) \to \eta N$, and k is the wave number. Figure 4.3 shows the calculated $\sigma_{\text{nuc}}^{\text{prev}}$ according to Eq. (4.5) as a function of the initial momentum of η meson in the center of mass frame.

Figure 4.4 illustrates the comparison between the measured cross section of η photoproduction from Mainz experiment [73] and the simulated cross section by Eq. (4.5) in the manner described in section 4.2.2. The dashed line in Fig. 4.4 stands for the cross section without any η nuclear effect, which corresponds to the cross section of elementary processes in Eq. (4.3) and Eq. (4.4) multiplied by the number of nucleons in the ^{12}C nucleus. By comparing the measured data plots and the simulated line, the uncertainty of $\sigma_{\text{nuc}}^{\text{prev}}$ was estimated from -50% to $+100\%$ in the previous study.

The analysis of the proton decay search in SK is conducted by reconstructing momenta and masses of the decay particles from a proton or the decayed proton itself from detected Cherenkov lights. If the decay particles are absorbed or scattered by the nuclear effect, the momenta and masses cannot be reconstructed correctly, and thus fail in identifying the initial particles. As a result, only the proton decay candidates of $p \to l^+\eta$ without experiencing any η nuclear effect can be identified by SK. Figure 4.5 shows more than 98.5% of the events that can be reconstructed as proton decays in SK experienced no nuclear interaction. Against this background, the systematic error arising from η nuclear effect was estimated by the uncertainty of the no nuclear interaction rate in a ^{16}O nucleus in the previous research [29]. The no nuclear interaction events are defined as those of proton decay MC where the η meson decayed before being scattered or absorbed (transferred into other particles) by nucleons. Table 4.3 shows the fractions of the final states of η mesons in the proton decay MC events deduced in [29]. From this table, the no nuclear interaction rate with taking into account the uncertainty of $\sigma_{\text{nuc}}^{\text{prev}}$ varies from 43% to 73% with a nominal value of 56%. Hence, the systematic error attributable to the nuclear effect of $p \to l^+\eta$ was estimated as

$$\varepsilon_{\text{nuc}}^{\text{prev}} = \frac{1}{2}\left(\frac{(|73-56|}{56} + \frac{|43-56|)}{56}\right) \sim 27\%. \tag{4.6}$$

4.3 Interpolating the η Nuclear Effect Cross Section

The experimental η absorption cross sections, σ_{abs}, were also measured in the Mainz experiment [73] in Fig. 4.6 as a function of the momentum of η meson in the laboratory frame. As shown in Fig. 4.3, the cross sections of η nucleus effect, $\sigma_{\text{nuc}}^{\text{prev}}$, does not match with the measured η absorption cross sections. This discrepancy could be interpreted as the former only consider a single excite state of $S_{11}(1535)$ resonance state without taking into account the effect of interference between other resonance states, such as $P_{11}(1440)$ and $D_{13}(1520)$.

In this study, the cross section of η nuclear effect, σ_{nuc}, and its uncertainty are estimated by adopting the least χ^2 method for both the measured η photoproduction cross section, $d\sigma_{\eta\text{photo}}/dp$, and η absorption cross section, σ_{abs}, from [73].

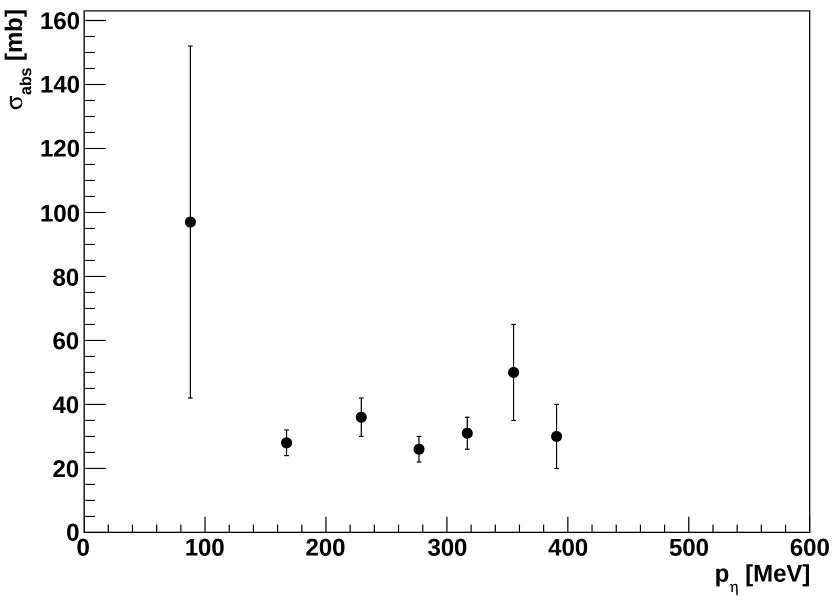

Fig. 4.6: Measured absorption cross section of η as a function of the laboratory momentum of η obtained by the experiment at Mainz. Data is taken from [73].

4.3.1 Fitting Two Experimental Data with Least Chi-square Method

The cross section σ_{nuc} is assessed with three types of functions by minimizing the χ-square values:

$$\chi^2 = \chi^2_{\eta\mathrm{photo}} + \chi^2_{\mathrm{abs}}, \tag{4.7}$$

where $\chi^2_{\eta\mathrm{photo}}$ and χ^2_{abs} are given as

$$\chi^2_{\eta\mathrm{photo}} = \sum_{i=1}^{n_{\eta\mathrm{photo}}} \left[\frac{1}{\varepsilon_{\eta\mathrm{photo},i}} \left(\frac{d\sigma_{\eta\mathrm{photo},i}}{dp} - \left(\frac{d\sigma_{\eta\mathrm{photo},i}}{dp}\right)_{\mathrm{sim}}\right)\right]^2, \tag{4.8}$$

$$\chi^2_{\mathrm{abs}} = \sum_{i=1}^{n_{\mathrm{abs}}} \left(\frac{\sigma_{\mathrm{abs},i} - \sigma_{\mathrm{nuc}}(p_\eta)}{\varepsilon_{\mathrm{abs},i}}\right)^2, \tag{4.9}$$

where $(d\sigma_{\eta\mathrm{photo}}/dp)_{\mathrm{sim}}$ is the simulated $d\sigma_{\eta\mathrm{photo}}/dp$, $\sigma_{\mathrm{nuc}}(p_\eta)$ is the assumed cross section of nuclear effect, $\varepsilon_{\eta\mathrm{photo}}$ and $\varepsilon_{\mathrm{abs}}$ are the errors of measured $(d\sigma_{\eta\mathrm{photo}}/dp)_{\mathrm{sim}}$ and σ_{abs}, respectively, and $n_{\eta\mathrm{photo}}$ and n_{abs} are the numbers of data points. Here, $\sigma_{\mathrm{abs}} \sim \sigma_{\mathrm{nuc}}$ is assumed as the difference between these two cross sections is the inclusion of the effects of the elastic scattering and multistep interactions, which can be assumed to play a minor role of up to a few percentage as discussed in [73]. The estimation of the errors of fitting parameters are described in section 4.3.2.

While the uncertainties reported in the η photoproduction experiment [73] had been contributed only by the systematic errors of 6% for the data points of the cross sections, the additional statistical errors are evaluated especially for the high momentum region, where the $d\sigma_{\eta\mathrm{photo}}/dp$ values converge to 0 μb $\times$ (MeV/c)$^{-1}$. By the fluctuation of the points at these values from the experiment of $E_\gamma = 634 - 705$ MeV with a ^{12}C target, the statistical error of 0.004 [mb] is additionally included in this study. Thus, The total uncertainty $\varepsilon_{\eta\mathrm{photo},i}$ is given as follows:

$$\varepsilon_{\eta\mathrm{photo},i} = \sqrt{\left(0.06 \times \frac{d\sigma_{\eta\mathrm{photo},i}}{dp}\right)^2 + (0.004)^2} \text{ mb}. \tag{4.10}$$

4.3.2 Estimation of the Uncertainty of Fitting Parameters

The fit of n-tuple data sets of $(x_1, y_1), \cdots, (x_n, y_n)$ with an arbitrary function $f(x; a_1, \cdots, a_m)$ to determine the parameters $a_1, \cdots, a_m$, the least χ^2 method is employed. In this method, the set of the parameters satisfying the χ^2 defined below to be the least are adopted as the best fit

$$\chi^2 \equiv \sum_{i=1}^{n} \left(\frac{y_i - y(x_i)}{\sigma_i}\right)^2. \tag{4.11}$$

The uncertainty of y_i given as σ_i is assumed to follow a Gaussian distributed random error. When the true parameter sets are supposed as $(a_1, \cdots, a_m)$, the likelihood of taking the n-tuple data sets $(x_1, y_1), \cdots, (x_n, y_n)$ is given as

$$P(a_1, \cdots, a_n) = \prod_{i=1}^{n} \frac{1}{\sigma_i\sqrt{2\pi}} \cdot \exp\left[-\frac{(y_i - f(x_i; a_1, \cdots, a_m))^2}{2\sigma_i^2}\right], \tag{4.12}$$

$$= \left(\prod_{i=1}^{n} \frac{1}{\sigma_i\sqrt{2\pi}}\right) \cdot \exp\left(-\frac{\chi^2}{2}\right), \tag{4.13}$$

where in the second line, the likelihood can be written as a function of χ^2 in Eq. (4.13) with the definition of χ^2(Eq. (4.11)). The likelihood $P(a_1, \cdots, a_n)$ reaches the maximum value when χ^2 takes its minimum χ^2_{min} of

$$\chi^2_{\mathrm{min}} = \sum_{i=1}^{n} \left(\frac{y_i - f(x_i; \tilde{a_1}, \cdots, \tilde{a_m})}{\sigma_i}\right)^2, \tag{4.14}$$

where $\tilde{a_1}, \cdots, \tilde{a_p}$ are the parameters of $f(x_i; \tilde{a_1}, \cdots, \tilde{a_m})$ with χ^2_{min}.

To estimate the uncertainties of the fitting parameters, consider the residual of χ^2, $\Delta\chi^2 = \chi^2 - \chi^2_{\mathrm{min}}$. From Eq. (4.11) and Eq. (4.14),

$$\Delta\chi^2 = \sum_{i=1}^{n} \frac{(y_i - f(x_i; a_1, \cdots, a_m))^2 - (y_i - f(x_i; \tilde{a}_1, \cdots, \tilde{a}_m))^2}{\sigma_i^2}, \tag{4.15}$$

$$= \sum_{i=1}^{n} \frac{(f(x_i; a_1, \cdots, a_m) + f(x_i; \tilde{a}_1, \cdots, \tilde{a}_m) - 2y_i)\,(f(x_i; a_1, \cdots, a_m) - f(x_i; \tilde{a}_1, \cdots, \tilde{a}_m))}{\sigma_i^2}. \tag{4.16}$$

By taking the second order of the differential coefficients,

$$\Delta\chi^2 \approx \sum_{i=1}^{n}\sum_{j=0}^{m} \frac{\left(2f(x_i; \tilde{a}_1, \cdots, \tilde{a}_m) - 2y_i + \frac{\partial f(x_i; \tilde{a}_1, \cdots, \tilde{a}_m)}{\partial a_j} \cdot \Delta a_j\right)}{\sigma_i^2} \cdot \left(\frac{\partial f(x_i; \tilde{a}_1, \cdots, \tilde{a}_m)}{\partial a_j} \cdot \Delta a_j\right), \tag{4.17}$$

where Δa_j is defined as $\Delta a_j = a_j - \tilde{a}_j$. By the definition of minimum χ^2 value, Eq. (4.14) can be transformed as:

$$\frac{\partial \chi^2(\tilde{a}_1, \cdots, \tilde{a}_m)}{\partial a_j} = 0, \tag{4.18}$$

$$\Leftrightarrow \sum_{i=0}^{n} \frac{f(x_i, \tilde{a}_1, \cdots, \tilde{a}_m) - y_i}{\sigma_i^2} \cdot \left(2 \frac{\partial f(x_i, \tilde{a}_1, \cdots, \tilde{a}_m)}{\partial a_j} \right) = 0. \tag{4.19}$$

Therefore, in the case of $\mathbf{a} \approx \tilde{\mathbf{a}}$, Eq. (4.17) can be approximated as:

$$\Delta\chi^2 \approx \sum_{j=1}^{m} A_j (a_j - \tilde{a}_j)^2. \tag{4.20}$$

Equation (4.13) can be transformed as bellow.

$$P(a_1, \cdots, a_n) = \prod_{i=1}^{n} \frac{1}{\sigma_i \sqrt{2\pi}} \cdot \exp\left[-\frac{1}{2}(\Delta\chi^2 + \chi^2_{\mathrm{min}}) \right], \tag{4.21}$$

$$\propto \prod_{j=1}^{m} \frac{1}{\sigma_i \sqrt{2\pi}} \cdot \exp\left[-\frac{A_j (a_j - \tilde{a_j})^2}{2} \right], \tag{4.22}$$

$$\propto \prod_{j=1}^{m} \frac{1}{\sigma_i \sqrt{2\pi}} \cdot \exp\left[-\frac{(a_j - \tilde{a_j})^2}{2\delta_j^2} \right], \tag{4.23}$$

where in the third line, $\sqrt{A_j} = 1/\delta_j$ is adopted. From Eq. (4.23), it can be approximated that $\Delta\chi^2$ would follow the χ^2 distribution with the number of freedom of m, which is the number of fitting parameters. From the χ^2 distribution, the value of $\Delta\chi^2$ when it is within the $1\sigma = 68.3\%$ region is deduced to satisfy $\Delta\chi^2 \leq 1.00$ when $m = 1$, $\Delta\chi^2 \leq 2.30$ when $m = 2$, and $\Delta\chi^2 \leq 3.53$ when $m = 3$. Accordingly, the errors of the fitting parameters are estimated as the uncertainties within the $\chi^2_{\mathrm{min}} + 1$ region for $m = 1.00$ fitting function, the $\chi^2_{\mathrm{min}} + 2.30$ region for $m = 2$ fitting function, and the $\chi^2_{\mathrm{min}} + 3.53$ region for $m = 3$ fitting function.

4.3.3 Reduced χ^2 value and the goodness of fit

The χ^2 distribution is known to obey a χ^2 distribution when the fit function is exactly same as the "true" function. This is based on the assumption that each data points should distribute with a Gaussian of the standard deviation of the error bars. As the minimum χ^2 value after a certain fit to n-point data with a k-parameter function is expected to follow the χ^2 distribution with the degree of freedom of $n - k$, the reduced χ^2, defined as

$$\chi^2_{\nu,\mathrm{min}} = \frac{\chi^2_{\mathrm{min}}}{n - k} \tag{4.24}$$

is often used as an indicator of the goodness of fit. As the mean value of a χ^2 distribution with the $n - k$ degree of freedom is $n - k$, it can be denoted that the fit is reasonable when $\chi^2_{\nu,\mathrm{min}} \sim 1$. While in the case of $\chi^2_{\nu,\mathrm{min}} > 1$, it is interpreted as less fit, the case of $\chi^2_{\nu,\mathrm{min}} < 1$ shows the function is over-fitting. Here below, the result of three different functions fit with χ^2 minimisation are discussed comparing with their goodness of fit.

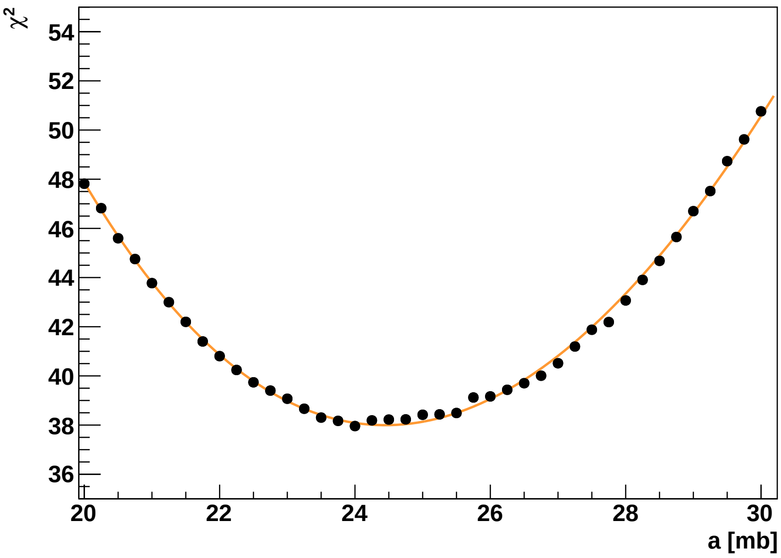

Fig. 4.7: χ^2 distribution when the cross section of the nuclear effect is assumed as $\sigma_{\mathrm{nuc}} = a$ [mb]. The orange line shows the fit results of χ^2 distribution with a quartic function.

4.3.4 Fit with three different functions

In this study, three types of functions listed below are compared to obtain the best estimation of σ_{nuc} function:

- **Case1:** $\sigma_{\mathrm{nuc}} = a$
- **Case2:** $\sigma_{\mathrm{nuc}} = a \cdot \exp\left(-b \cdot p_\eta\right)$
- **Case3:** $\sigma_{\mathrm{nuc}} = a + b \cdot \exp\left(-c \cdot p_\eta\right)$

(1) Case1: $\sigma_{\mathrm{nuc}} = a$

First, from the distribution of measured σ_{abs} in Fig. 4.6, σ_{nuc} is considered as a function independent of p_η:

$$\sigma_{\mathrm{nuc}} = a \text{ [mb]}. \tag{4.25}$$

$d\sigma_{\eta\mathrm{photo}}/dp$ is simulated by σ_{nuc}, and χ^2 defined in Eq. (4.7) is calculated. Figure 4.7 shows the distribution of χ^2 and parameter a. From the fitting curve of Fig. 4.7, χ^2 represents the minimum value of $\chi^2_{\mathrm{min}} = 38.2$, and $\chi^2_{\nu,\mathrm{min}} = 2.12$ at $a = 24.3$ mb, explained in section 4.3.3. Furthermore, $\chi^2 = \chi^2_{\mathrm{min}} + 1.00$ is satisfied when $a = 23.0$ or 25.8 mb. Therefore, as discussed in section 4.3.2, σ_{nuc} and its uncertainty is estimated as

$$\sigma_{\mathrm{nuc}} = 24.3^{+1.5}_{-1.3} \text{ mb}. \tag{4.26}$$

The measured and assumed absorption cross sections σ_{abs} and the measured and simulated η photoproduction cross sections are shown in Fig. 4.8 and Fig. 4.9, respectively.

(2) Case2: $\sigma_{\mathrm{nuc}} = a \cdot \exp\left(-b \cdot p_\eta\right)$

Figure 4.9 demonstrates the simulated differential cross sections of η photoproduction are underestimated in the high momentum region compared to measured values. This means

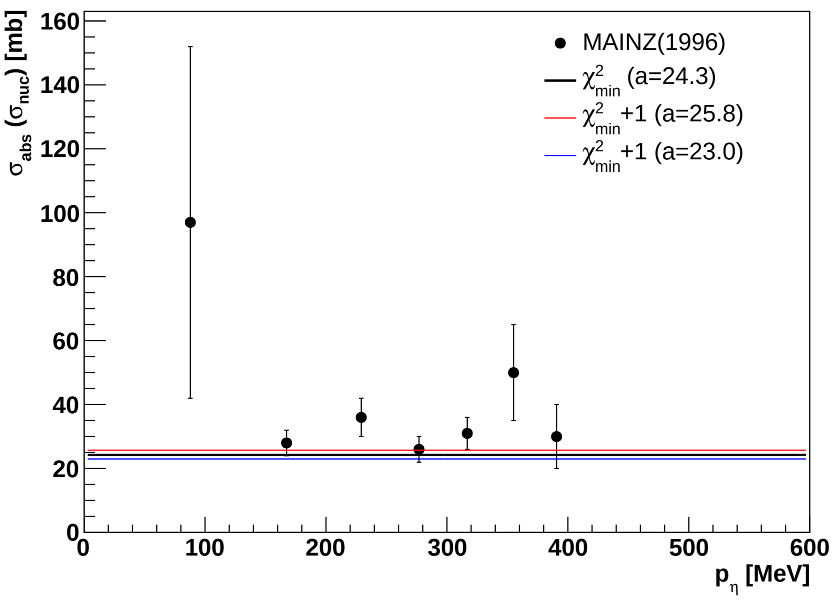

Fig. 4.8: Measured η absorption cross sections, $\sigma_{\rm abs}$, and assumed cross sections of η nuclear effect in the η photoproduction simulation as $\sigma_{\rm nuc} = a$ [mb]. The experimental data of $\sigma_{\rm abs}$ from Mainz experiment [73] are shown as the black circles. The black, red, and blue solid lines show the nuclear effect cross sections, $\sigma_{\rm nuc}$, with parameters of $a = 24.3$, $a = 25.8$, and $a = 23.0$, respectively.

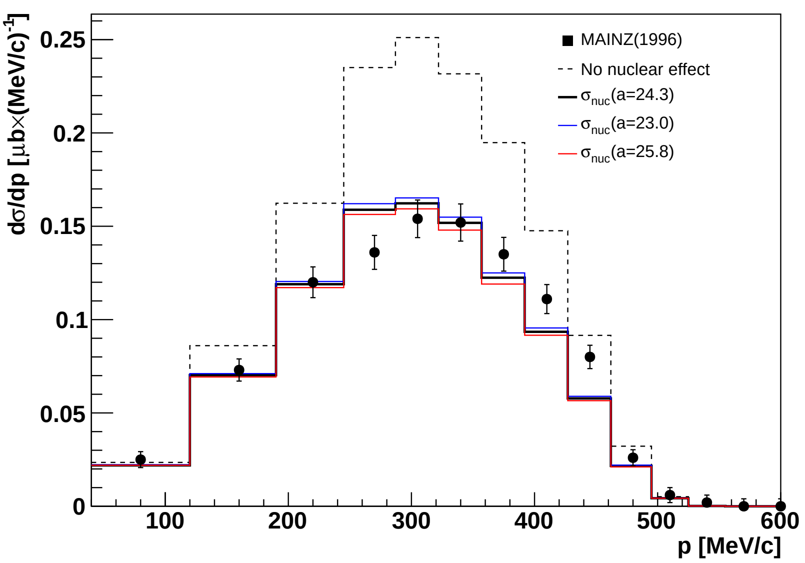

Fig. 4.9: Measured and simulated differential cross sections of photoproduction of η assuming the cross section of the η nuclear effect as $\sigma_{\rm nuc} = a$ [mb]. The experimental data from Mainz experiment [73] are shown as the black circles. The dashed line shows the cross-section without η nuclear effect, and the black, red, and blue solid lines show the simulated cross sections with parameters of $a = 24.3$, $a = 25.8$, and $a = 23.0$, respectively.

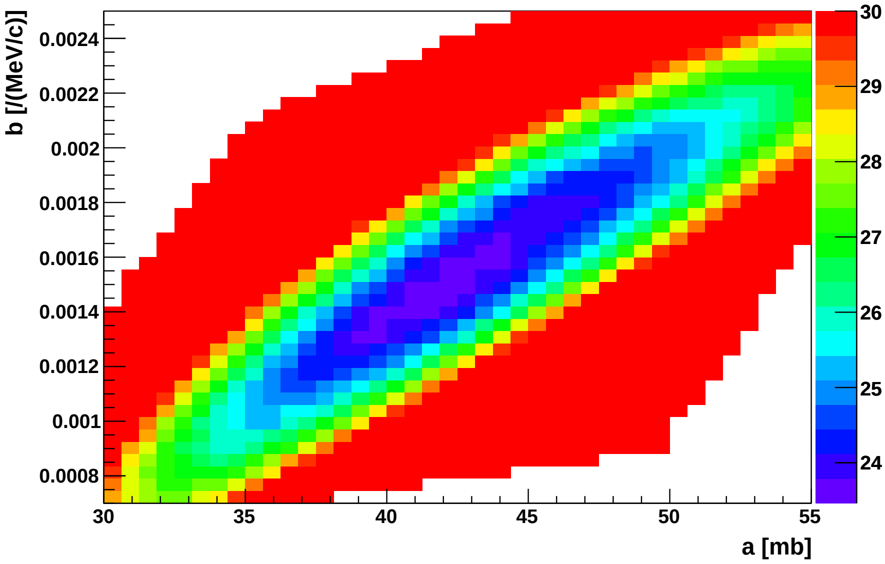

Fig. 4.10: χ^2 distribution when the cross section of the nuclear effect is assumed as $\sigma_{\rm nuc} = a \cdot \exp(-b \cdot p_\eta)$ [mb]. The red circle in the center shows the parameter set whose χ^2 showed the minimum value $\chi^2_{\rm min}$. The parameter sets in the region colored with red satisfy $\chi^2 > 30.0$.

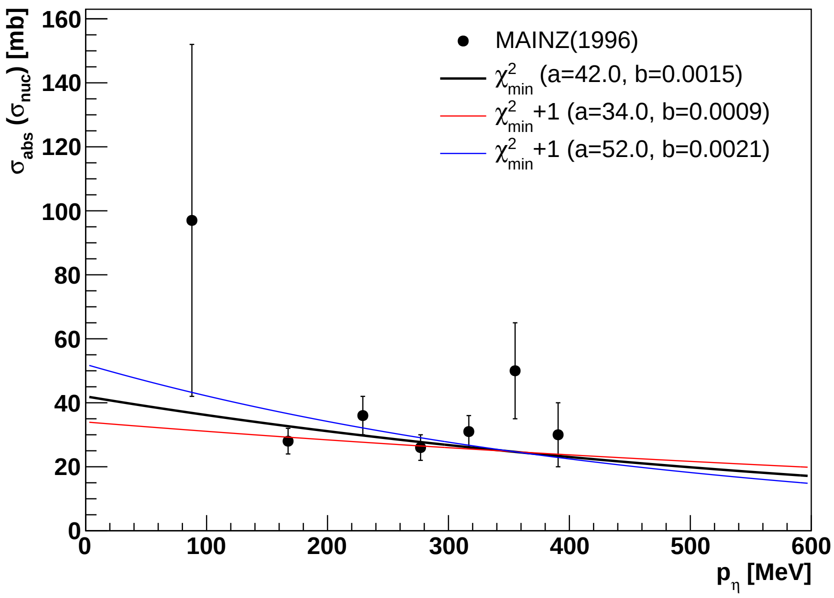

Fig. 4.11: Measured η absorption cross sections, $\sigma_{\rm abs}$, and assumed cross sections of η nuclear effect in the η photoproduction simulation as $\sigma_{\rm nuc} = a \cdot \exp(-b \cdot p_\eta)$ [mb]. The experimental data of $\sigma_{\rm abs}$ from Mainz experiment [73] are shown as the black circles. The black, red, and blue solid lines show the nuclear effect cross sections, $\sigma_{\rm nuc}$, with parameters of $(a, b) = (42.0, 0.0015) = (34.0, 0.0009)$, and $(52.0, 0.0021)$, respectively. The parameter sets of $(a, b) = (34.0, 0.0009)$ and $(52.0, 0.0021)$ are chosen as representative points that fulfill $\chi = \chi_{\rm min} + 2.30$.

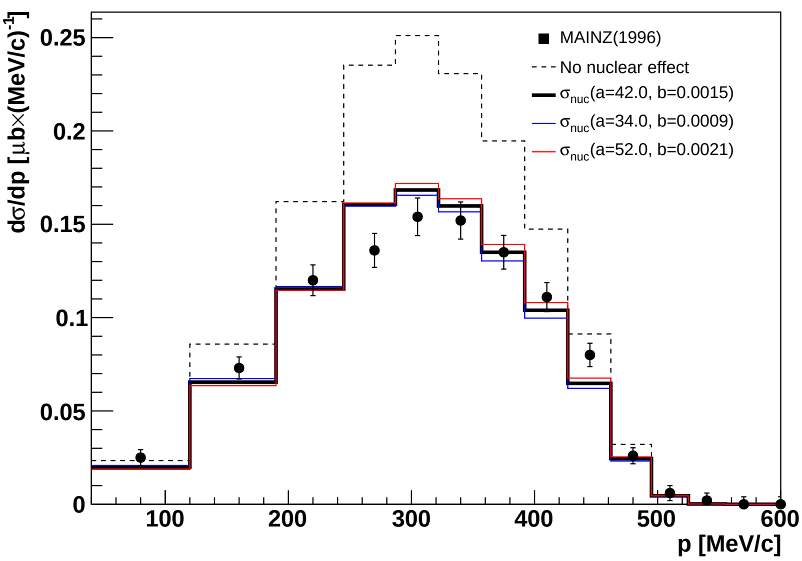

Fig. 4.12: Measured and simulated differential cross sections of photoproduction of η assuming the cross section of the η nuclear effect as $\sigma_{\rm nuc} = a \cdot \exp(-b \cdot p_\eta)$ [mb]. The experimental data from Mainz experiment [73] are shown as the black circles. The dashed line shows the cross-section without η nuclear effect, and the black, red, and blue solid lines show the simulated cross sections with parameters of $(a, b) = (42.0, 0.0015) = (34.0, 0.0009)$, and $(52.0, 0.0021)$, respectively. The parameter sets of $(a, b) = (34.0, 0.0009)$, $(52.0, 0.0021)$ are chosen as representative points that fulfill $\chi = \chi_{min} + 2.30$.

the η mesons with high momenta have been much absorbed or scattered in the nuclei than actually they are, indicating the overestimation of nuclear effect cross section. Therefore, so as to mitigate this inconsistency, an exponential function decreasing with momentum is tested as:

$$\sigma_{\rm nuc} = a \cdot \exp(-b \cdot p_\eta) \text{ [mb]}. \tag{4.27}$$

$d\sigma_{\eta photo}/dp$ is simulated by $\sigma_{\rm nuc}$, and χ^2 defined in Eq. (4.7) is calculated. Figure 4.10 shows the distribution of χ^2, parameter a, and b. χ^2 represents the minimum value of $\chi^2_{\rm min} = 23.5$, $\chi^2_{\nu,\rm min} = 1.39$ when $(a, b) = (42.0,\ 0.0015)$. Thus, the most plausible $\sigma_{\rm nuc}$ as a function of exponential is deduced to be

$$\sigma_{\rm nuc} = 42.0 \cdot \exp(-0.0015 \cdot p_\eta) \text{ mb}. \tag{4.28}$$

The region satisfying $\chi^2 = \chi^2_{\rm min} + 2.30 = 25.8$ corresponds to the 68.3% confidence level of parameter set (a, b). The measured and assumed absorption cross sections $\sigma_{\rm abs}$ are shown in Fig. 4.11, and the measured and simulated η photoproduction cross sections are described in Fig. 4.12.

(3) Case3: $\sigma_{\rm nuc} = a + b \cdot \exp(-c \cdot p_\eta)$

Finally, the χ^2 minimization is tested as a combined function of Eq. (4.25) and Eq. (4.27) as:

$$\sigma_{\rm nuc} = a + b \cdot \exp(-c \cdot p_\eta) \text{ [mb]}. \tag{4.29}$$

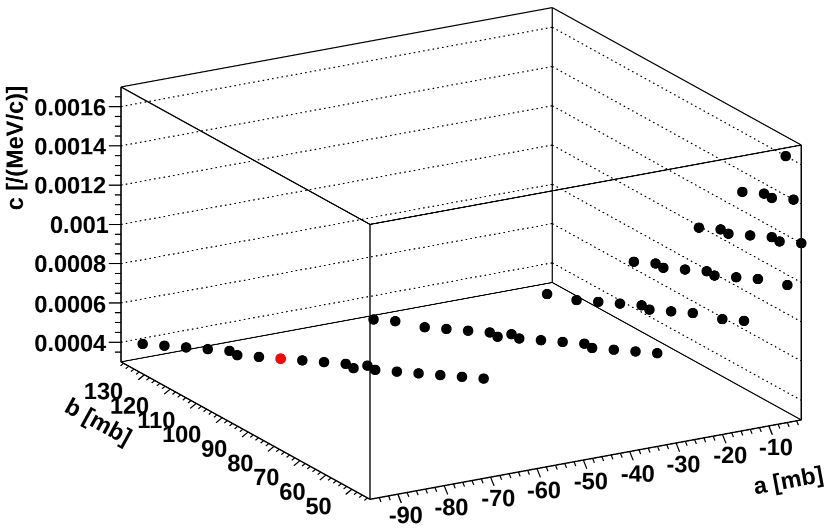

Fig. 4.13: χ^2 distribution when the cross section of the nuclear effect is assumed as $\sigma_{\mathrm{nuc}} = a + b \cdot \exp(-c \cdot p_\eta)$ [mb]. The red circle stands out for the parameter set whose χ^2 showed the minimum value χ^2_{min}. Although the 1σ confidence level of the fitting parameters with three parameter function is given by $\chi^2 \le \chi^2_{\mathrm{min}} + 3.53$, the black circles show the parameter sets which satisfied $\chi^2 \le \chi^2_{\mathrm{min}} + 1$.

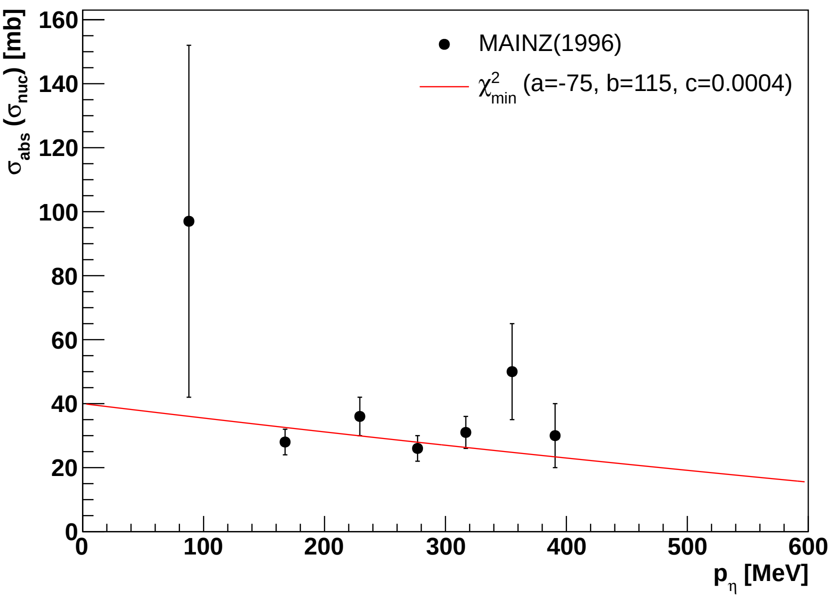

Fig. 4.14: Measured η absorption cross sections, σ_{abs}, and assumed cross sections of η nuclear effect in the η photoproduction simulation as $\sigma_{\mathrm{nuc}} = a \cdot \exp(-b \cdot p_\eta)$ [mb]. The experimental data of σ_{abs} from Mainz experiment [73] are shown as the black circles. The red solid line show the nuclear effect cross section, σ_{nuc}, with parameters of $(a, b, c) = (-75.0, 115, 0.0015)$ with χ^2_{min}.

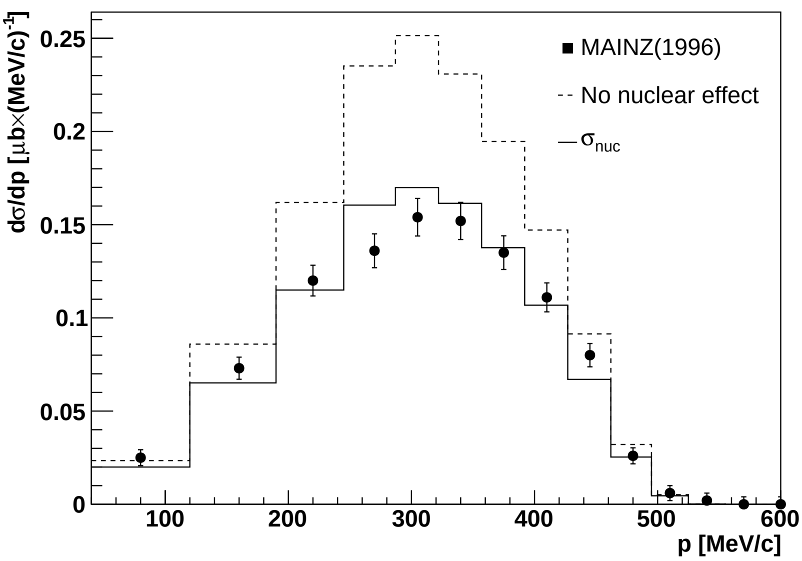

Fig. 4.15: Measured and simulated differential cross sections of photoproduction of η assuming the cross section of the η nuclear effect as $\sigma_{\text{nuc}} = a + b \cdot \exp(-c \cdot p_\eta)$ [mb]. The dashed line shows the cross-section without η nuclear effect, and the black solid line show the simulated cross section with parameters of $(a, b, c) = (-75.0, 115, 0.0015)$ with χ^2_{min}.

$d\sigma_{\eta\text{photo}}/dp$ is simulated by σ_{nuc} and χ^2 defined in Eq. (4.7) is calculated. Figure 4.13 indicates the three parameters, a, b, and c, satisfying the condition of $\chi^2 \leq \chi^2_{\text{min}} + 1$. Here, $\chi^2_{\text{min}} = 22.3$, $\chi^2_{\nu,\text{min}} = 1.39$ are achieved at $(a,\ b,\ c) = (-75,\ 115,\ 0.0004)$ shown as the red circle in the figure. Thus, the most plausible σ_{nuc} written by this function is deduced to be

$$\sigma_{\text{nuc}} = -75 + 115 \cdot \exp(-0.0004 \cdot p_\eta) \text{ mb}. \tag{4.30}$$

The measured and assumed absorption cross sections σ_{abs} are shown in Fig. 4.14, and the measured and simulated η photoproduction cross sections are described in Fig. 4.15. From the the chart illustrated in Fig. 4.13, it can be seen that there is a correlation between parameters a and b. The uncertainties of fitting parameters (section 4.3.2) are not estimated for this function since the goodness of fit does not improved from Eq. (4.27) as described in section 4.3.5.

4.3.5 Goodness of Fittings

To summarize the χ^2 minimization with three types of functions, the achieved $\chi^2_{\nu,\text{min}}$ and the degrees of freedom for respective functions, $\sigma_{\text{nuc}} = a$, $\sigma_{\text{nuc}} = a \cdot \exp(-b \cdot p_\eta)$, and $\sigma_{\text{nuc}} = a + b \cdot \exp(-c \cdot p_\eta)$, are 2.12 with 18, 1.39 with 17, and 1.39 with 16. The p-values are 0.004, 0.134, and 0.134, enumerated in the same order as above. While slight improvement could be seen from the first to the second fitting, no difference appeared between the second and the third ones. Thus, the third function is not dealt with in this study. From this result, it is suggested that the simple exponential function Eq. (4.28)

$$\sigma_{\text{nuc}} = 42.0 \cdot \exp(-0.0015 \cdot p_\eta) \text{ mb}, \tag{4.28}$$

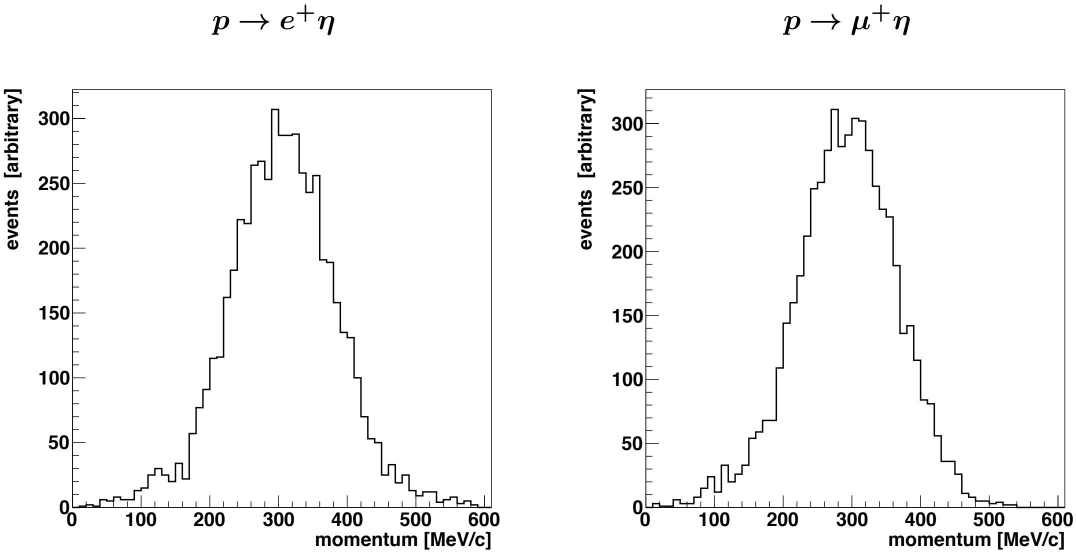

Fig. 4.16: Momentum distributions of η mesons from bound protons of $p \to e^+\eta$ (left) and $p \to \mu^+\eta$ (right).

Tab. 4.4: Fraction of the final states of η meson from the proton decay of $p \to e^+\eta$ in ^{16}O when the η nuclear effect is assumed as $\sigma_{\text{nuc}} = a$ [mb].

Parameter a	$a = 24.3$	$a = 25.8$	$a = 23.0$
η nuclear effect in ^{16}O nucleus	χ^2_{min}	$\chi^2_{\text{min}} + 1.00$	$\chi^2_{\text{min}} + 1.00$
no interaction	60%	59%	63%
scattered	6%	4%	5%
absorbed	38%	23%	53%

would be the best among the three.

It is also noticeable that there is a discrepancy about two times of the standard deviation at the (245, 295) and (425, 460) MeV/c bins in every fits shown in Fig. 4.9, Fig. 4.12, and Fig. 4.15 could not be improved in any attempt. The momentum after the proton decay from a bound proton is simulated to distribute around 300 MeV/c as indicated in Fig. 4.16. Although the deficiency at the low momentum side and the excess at the opposite side of η photoproduction cross sections can be found, the consistency of fit functions with the measured σ_{abs} around 300 MeV/c region can support the validity of the estimation.

4.3.6 Uncertainty Estimation from Each Function

By applying the estimated cross section of η nuclear effect as a function of $\sigma_{\text{nuc}} = a$ ($\sigma_{\text{nuc}} = a \cdot \exp(-b \cdot p_\eta)$) to proton decay MC simulations, the fraction of the final states of η meson for $p \to e^+\eta$ and $p \to \mu^+\eta$ are be obtained as Tab. 4.4 and Tab. 4.5 (Tab. 4.6 and Tab. 4.7). The no interaction rate varies around 5% (10%) relative to the nominal value in the column second to the left within the uncertainty of the parameter a (parameter sets of a and b) when the function is assumed as a constant value (an exponential).

Tab. 4.5: Fraction of the final states of η meson from the proton decay of $p \to \mu^+\eta$ in ^{16}O when the η nuclear effect is assumed as $\sigma_{\text{nuc}} = a$ [mb].

Parameter a	$a = 24.3$	$a = 25.8$	$a = 23.0$
η nuclear effect in ^{16}O nucleus	χ^2_{min}	$\chi^2_{\text{min}} + 1.00$	$\chi^2_{\text{min}} + 1.00$
no interaction	62%	60%	65%
scattered	6%	4%	5%
absorbed	38%	23%	53%

Tab. 4.6: Fraction of the final states of η meson from the proton decay of $p \to e^+\eta$ in ^{16}O when the η nuclear effect is assumed as $\sigma_{\text{nuc}} = a \cdot \exp(-b \cdot p_\eta)$ [mb].

Parameters (a, b)	$(42.0, 0.0015)$	$(52.0, 0.0021)$	$(34.0, 0.0009)$
η nuclear effect in ^{16}O nucleus	χ^2_{min}	$\chi^2_{\text{min}} + 2.30$	$\chi^2_{\text{min}} + 2.30$
no interaction	65%	60%	67%
scattered	6%	4%	5%
absorbed	38%	23%	53%

Tab. 4.7: Fraction of the final states of η meson from the proton decay of $p \to \mu^+\eta$ in ^{16}O when the η nuclear effect is assumed as $\sigma_{\text{nuc}} = a \cdot \exp(-b \cdot p_\eta)$ [mb].

Parameters (a, b)	$(42.0, 0.0015)$	$(52.0, 0.0021)$	$(34.0, 0.0009)$
η nuclear effect in ^{16}O nucleus	χ^2_{min}	$\chi^2_{\text{min}} + 2.30$	$\chi^2_{\text{min}} + 2.30$
no interaction	64%	60%	70%
scattered	6%	4%	5%
absorbed	38%	23%	53%

Tab. 4.8: The no η nuclear interaction rate of η meson from the proton decay of $p \to e^+\eta$ in ^{16}O when the η nuclear effect is assumed as $\sigma_{\text{nuc}} = a$ [mb] or $\sigma_{\text{nuc}} = a \cdot \exp(-b \cdot p_\eta)$ [mb].

	No η nuclear interaction rate		
Function of σ_{nuc}	Nominal σ_{nuc}	Minimum	Maximum
$\sigma_{\text{nuc}} = a$ [mb]	60%	59%	63%
$\sigma_{\text{nuc}} = a \cdot \exp(-b \cdot p_\eta)$ [mb]	65%	60%	67%
Adopted	65%	59%	67%

Tab. 4.9: The no η nuclear interaction rate of η meson from the proton decay of $p \to \mu^+\eta$ in ^{16}O when the η nuclear effect is assumed as $\sigma_{\text{nuc}} = a$ [mb] or $\sigma_{\text{nuc}} = a \cdot \exp(-b \cdot p_\eta)$ [mb].

	No η nuclear interaction rate		
Function of σ_{nuc}	Nominal σ_{nuc}	Minimum	Maximum
$\sigma_{\text{nuc}} = a$ [mb]	62%	60%	65%
$\sigma_{\text{nuc}} = a \cdot \exp(-b \cdot p_\eta)$ [mb]	64%	60%	70%
Adopted	64%	60%	70%

4.4 Estimation of Effect on Proton Decay Search

The no nuclear interaction rate of η meson of proton decay MC events for $p \to e^+\eta$ and $p \to \mu^+\eta$ are individually summarized in Tab. 4.8 and Tab. 4.9. The nominal σ_{nuc} has been determined as the σ_{nuc} with parameters minimizing χ^2. The right two columns in Tab. 4.8 and Tab. 4.9 show the minimum and maximum ratio above all the proton decay MC events generated with set of parameters within $\chi^2_{\text{min}}+1.00$ or $\chi^2_{\text{min}}+2.30$ for each case. The adopted minimum and maximum values have been decided so that the uncertainty would take the widest range. By taking the relative variations of no interaction rates, the systematic errors arose from η nuclear effect of $p \to e^+\eta$ and $p \to \mu^+\eta$ modes are estimated as

$$\varepsilon_{\text{nuc},\ p\to e^+\eta} = \frac{|59-65|}{65} \sim 10\%, \tag{4.31}$$

$$\varepsilon_{\text{nuc},\ p\to \mu^+\eta} = \frac{|70-64|}{64} \sim 10\%. \tag{4.32}$$

Chapter 5

Proton Decay Analysis

The proton decay into $p \to e^+\eta$ and $p \to \mu^+\eta$, followed by $\eta \to 2\gamma$ decay are searched by analyzing the SK-IV data obtained from October 21st 2015 to May 31st 2018, which have not been analyzed in the previous research [29]. The amount of the statistics corresponds to 904.99 days of live time and 55.7 kton·years of exposure. The proton decay candidates are extracted from data by the event selection criteria described in Tab. 5.1. The signal efficiencies are evaluated by the number of events survived the selection criteria in the proton decay MC. The background events are estimated by applying the criteria to 500 years of the atmospheric neutrino MC and then normalizing by live time. Finally, the partial lifetime limits of proton for the two decay modes are calculated from the newly analyzed data in this study and the one scrutinized in the previous study [29].

5.1 Proton Decay Search

The proton decays into an antilepton and an η meson back-to-back with a monochromatic momentum of 310.0 MeV/c for $p \to e^+\eta$ and 297.7 MeV/c for $p \to \mu^+\eta$ in the proton rest frame. Figure 5.1 shows the signals of a typical proton decay MC event of $p \to e^+\eta$. Three shower-like (e-like) Cherenkov rings are clearly seen; one of the rings is produced by a positron and the rests are from η. On the other hand, Fig. 5.2 shows the signals of a typical event of $p \to \mu^+\eta$. The ring in the right with a sharp outline corresponds to the antimuon, and the other two are derived from γ-rays.

5.1.1 Selection Criteria

In order to search the data sets of SK for proton decay events, it is essential to sort out the events by the features of proton decay events and extract the candidates. Here, the information listed below are utilized for this event selection.

1. The number of the Cherenkov rings
2. The pattern of the Cherenkov rings
3. The reconstructed invariant η mass, m_η
4. The number of Michel electrons
5. The reconstructed total mass, m_{tot}

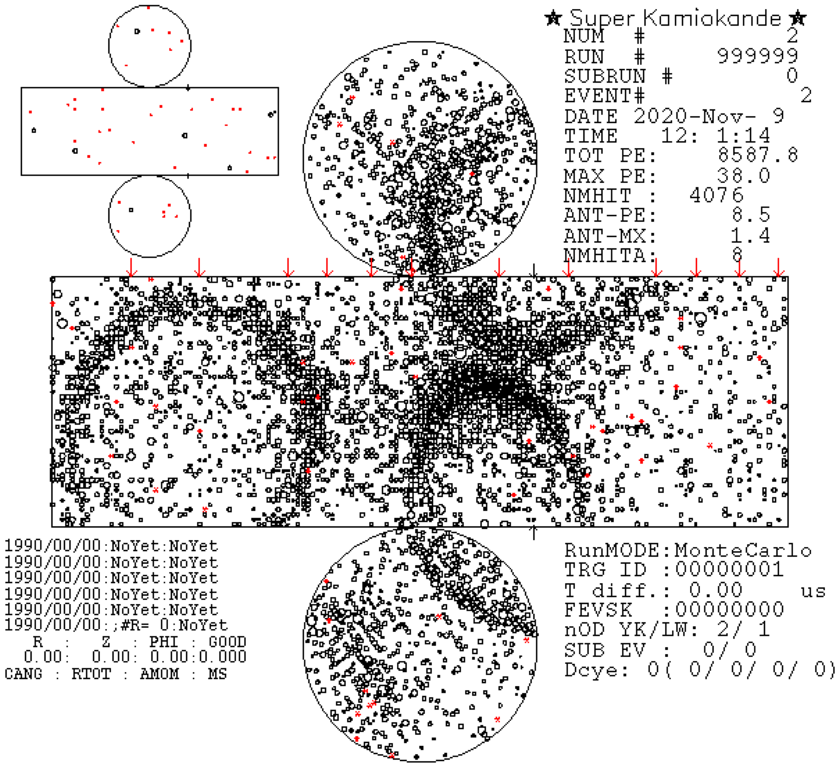

Fig. 5.1: A typical PMT hit pattern of $p \to e^+\eta$, $\eta \to 2\gamma$ events in SK.

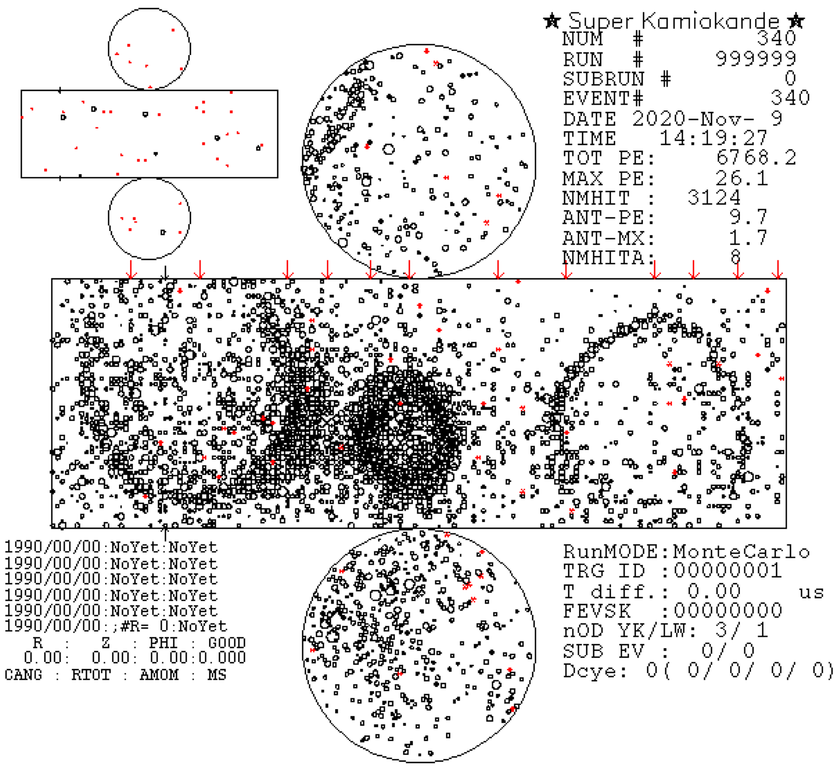

Fig. 5.2: A typical PMT hit pattern of $p \to e^+\eta$, $\eta \to 2\gamma$ events in SK.

Tab. 5.1: Event selection criteria for $p \to l^+\eta, \eta \to 2\gamma$ modes.

		Event cut	$p \to e^+\eta, \eta \to 2\gamma$	$p \to \mu^+\eta, \eta \to 2\gamma$
A		The number of rings	3	3
B		PID	all shower-like	one non-shower-like, two shower-like
C		Invariant η mass (m_η)	$480 \leq m_\eta \leq 620$	$480 \leq m_\eta \leq 620$
D		The number of Michel electrons	0	1
E		The total momentum (p_{tot}), the total invariant mass (m_{tot})	$p_{\text{tot}} \leq 250$ $800 \leq m_{\text{tot}} \leq 1050$	$p_{\text{tot}} \leq 250$ $800 \leq m_{\text{tot}} \leq 1050$
F		The total momentum (p_{tot})	$100 < p_{\text{tot}} \leq 250$	$100 < p_{\text{tot}} \leq 250$
	H	The number of neutrons	0	0
G		The total momentum (p_{tot})	$p_{\text{tot}} \leq 100$	$p_{\text{tot}} \leq 100$
	I	The number of neutrons	0	0

6. The reconstructed total momentum, p_{tot}

$p_{\text{tot}}, m_{\text{tot}}$ and the total energy E_{tot} are given by

$$p_{\text{tot}} = \left| \sum_{i=1}^{n_{\text{par}}} \boldsymbol{p_i} \right|, \tag{5.1}$$

$$E_{\text{tot}} = \sum_{i=1}^{n_{\text{par}}} \sqrt{m_i^2 + \boldsymbol{p_i}^2}, \tag{5.2}$$

$$m_{\text{tot}} = \sqrt{E_{\text{tot}}^2 - p_{\text{tot}}^2}, \tag{5.3}$$

where m_i is the mass of i-th particle, $\boldsymbol{p_i}$ is the momentum of i-th particle (ring), and n_{par} is the number of decay particles. For $p \to e^+\eta$ ($p \to \mu^+\eta$) mode, the decay particles a positron (antimuon) and an η meson, and the number of decay particles equals two. m_η is calculated by the same manner as Eq. (5.1)-Eq. (5.3), with decay particles of γ-rays and $n_{\text{par}} = 2$.

All the conditions for proton decay events described above are summarized in Tab. 5.1. The criteria H and I are applied for events passed F and G, respectively. Fully Contained Fiducial Volume (FCFV) cut, which requires the distance between the reconstructed vertex and the wall to be larger than 200 cm, has been applied to all the events in the proton decay search. The definitions and details of FC events are described in section 2.3. Hereinafter, the region of reconstructed total mass and momenta satisfying the criterion H (I) are called as upper (lower) signal box.

A: Number of Rings In the proton decay modes studied in this thesis, a proton decays into an antilepton and an η meson back-to-back in the proton rest frame, and the η meson decays into two γ-rays. Therefore, all the proton decay events produce there rings: one from the antilepton and the other two from the γ-rays. From these characteristics, proton decay events should be detected with three Cherenkov rings, which is indicated as criteria A in Tab. 5.1.

The number of rings distributions from all decay modes of η mesons are shown in Fig. 5.3 for each $p \to e^+\eta$ and $p \to \mu^+\eta$ MC events. It is obvious that 3-ring events dominate for the proton decay MC events. The fractions of 3-ring events are 49% (48%)

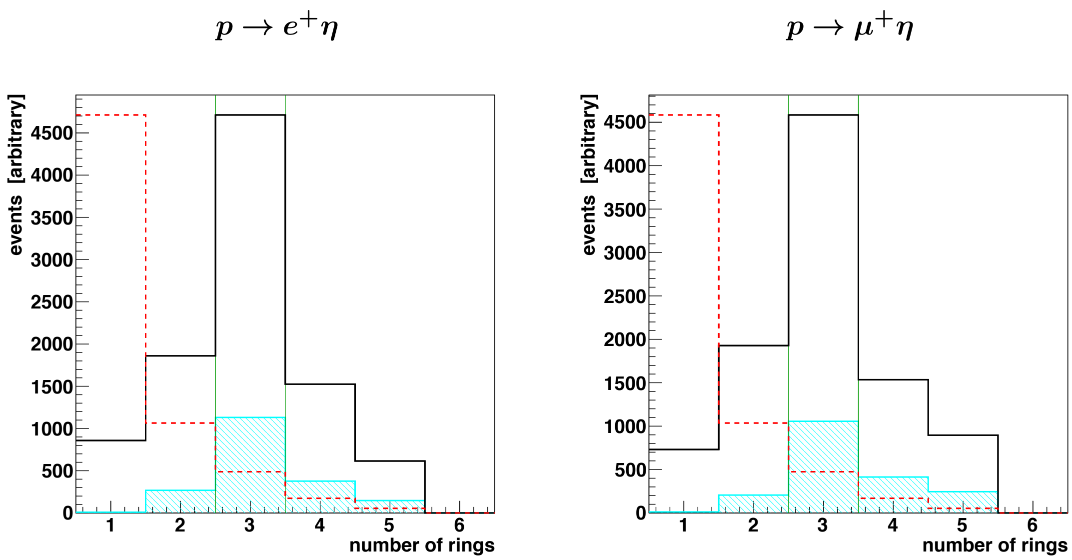

Fig. 5.3: Distributions of the number of ring of the $p \rightarrow e^+\eta$ (left) and $p \rightarrow \mu^+\eta$ (right) MC. All of the decay modes of η mesons are considered. The black and cyan shaded histogram shows the distribution from all and free protons, respectively. The red dashed line shows the number of rings distribution of the atmospheric neutrino MC in SK-IV normalized by the maximum bin values. The green solid lines indicate the selection criterion A in Tab. 5.1

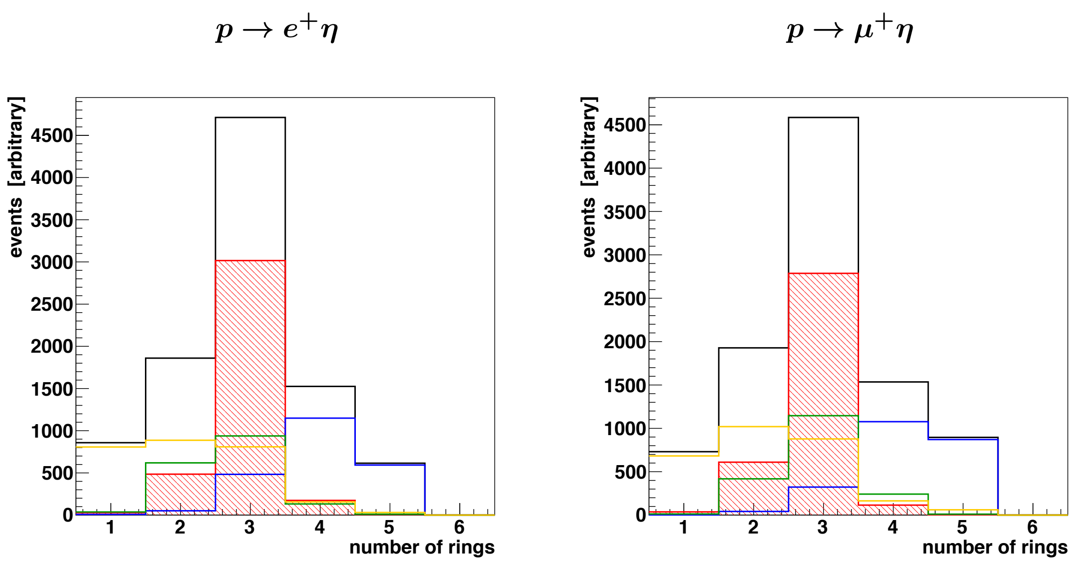

Fig. 5.4: Distributions of the number of ring depending on the decay modes of the η meson from $p \rightarrow e^+\eta$ (left) and $p \rightarrow \mu^+\eta$ (right) MC. The red shaded histogram, the blue and green histograms shows the distribution of the $\eta \rightarrow 2\gamma$, $\eta \rightarrow 3\pi^0$, and $\eta \rightarrow \pi^+\pi^-\pi^0$ modes, respectively. The orange histogram represent the distribution for events where the η mesons are absorbed or scattered by the nuclear effect.

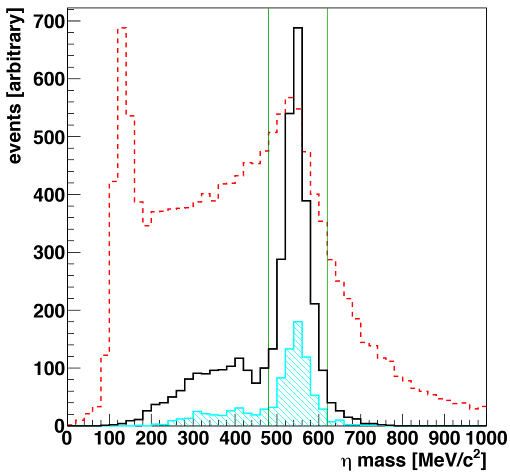

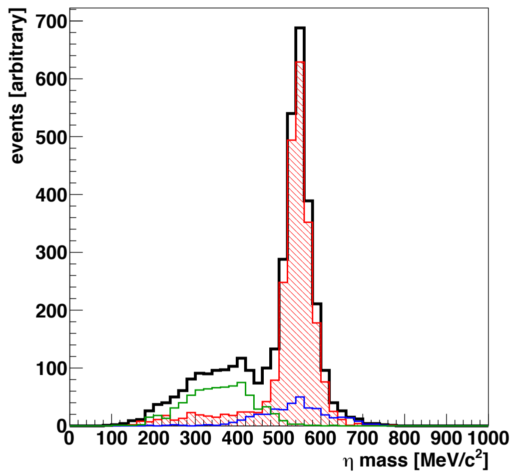

Fig. 5.5: Distributions of reconstructed η invariant mass of the $p \to e^+\eta$ MC in SK-IV after applying the selection criteria A and B. The black solid lines show all the decay branches of the η meson. Left figure: The cyan shaded histogram shows the distribution for free protons and the red dashed line shows the the distribution of the atmospheric neutrino MC in SK-IV normalized by the maximum bin values. The green solid lines indicate the selection criteria C in Tab. 5.1. Right figure: The red shaded histogram, the blue and green histograms shows the distribution of the $\eta \to 2\gamma$, $\eta \to 3\pi^0$, and $\eta \to \pi^+\pi^-\pi^0$ modes, respectively.

for $p \to e^+\eta$ ($p \to \mu^+\eta$) from all protons and 60% (58%) for $p \to e^+\eta$ ($p \to \mu^+\eta$) from free protons. The number of rings distributions for each η meson decay modes are shown in Fig. 5.4. Here, the 1, 2, and 4-ring events of $\eta \to 2\gamma$ mainly attribute to the overlaps of Cherenkov rings to miscount the number of rings. It is clear that the majority of 4 and 5-ring events derives from $\eta \to 3\pi^0$. In addition, most of the 1-ring events arise from events with η mesons being absorbed by the nuclear effect. On the other hand, 1-ring events dominate for the background atmospheric neutrino events from a charged lepton.

B: Particle Identification Another characteristic of the rings is their patterns. Positrons and γ-rays would produce shower-like (e-like) Cherenkov rings, whereas antimuons would produce non-shower-like (μ-like) rings while propagating through the water. From these characteristics, proton decay events should be detected with three Cherenkov rings, and all of the rings should be shower-like for $p \to e^+\eta$ and one of the rings should be no non-shower-like for $p \to \mu^+\eta$ events (criterion B).

C: Reconstructed η Mass If the two shower-like rings derived from γ-rays are detected, the invariant mass of the η meson can be reconstructed by the energies and momenta of these two rings. In the $p \to e^+\eta$ event, however, all three rings show shower-like pattern and the ring of a positron cannot be distinguished from those of γ-rays. To solve this problem, m_η is reconstructed by taking all the possible combinations of two Cherenkov rings. The two rings that can reconstruct the closest mass to the rest mass of η meson are determined as rings derived from γ-rays from η meson decay.

Figure 5.5 shows the distributions of reconstructed η mass after selection criteria A and B for $p \to e^+\eta$ proton decay MC and atmospheric neutrino MC on the left and for each η decay modes on the right. The same distributions for $p \to \mu^+\eta$ MC are shown in

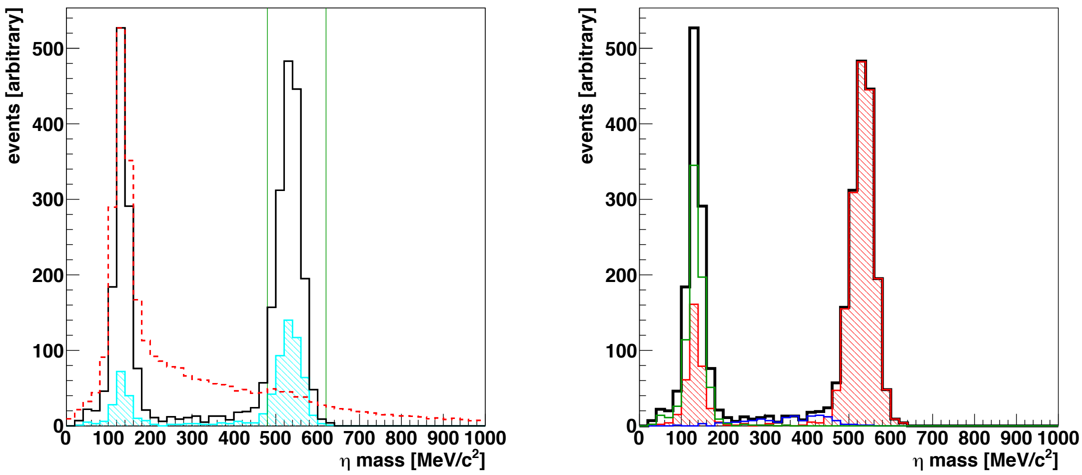

Fig. 5.6: Distributions of reconstructed η invariant mass of the $p \to \mu^+\eta$ MC in SK-IV after applying the selection criteria A and B. The black solid lines show all the decay branches of the η meson. Left figure: the cyan shaded histogram shows the distribution for free protons and the red dashed line shows the the distribution of the atmospheric neutrino MC in SK-IV normalized by the maximum bin values. The green solid lines indicate the selection criteria C in Tab. 5.1. Right figure: the red shaded histogram, the blue and green histograms shows the distribution of the $\eta \to 2\gamma$, $\eta \to 3\pi^0$, and $\eta \to \pi^+\pi^-\pi^0$ modes, respectively.

Fig. 5.6. From the figure on the left in Fig. 5.5, the distribution of proton decay MC events has a peak at ~ 550 MeV/c^2 while the rest mass of η meson is 547.8 MeV/c^2. In contrast, the atmospheric neutrino MC shows peaks around ~ 140 MeV/c^2 and ~ 540 MeV/c^2. Thus, events satisfying $480 \leq m_\eta \leq 620$ MeV/c^2 are selected as candidates. Focusing on the right, it can be seen that most of the events composing the 547.8 MeV/c^2 peak are derived from $\eta \to 2\gamma$. On the other hand, from the left figure of Fig. 5.6, $p \to \mu^+\eta$ MC makes another peak at around ~ 140 MeV/c^2 besides ~ 550 MeV/c^2 from η rest mass. The right figure shows that this low momentum peak is mainly composed of $\eta \to \pi^+\pi^-\pi^0$ events.

The majority of the background events passing criterion A and B consists of an antilepton and single or multiple pions produced events, where a neutral pion decaying into two γ-rays. Muons are generated in CC pion production events induced by muon neutrinos, and the observed three rings can be classified into one μ-like ring and two e-like rings from γ-rays. Therefore, pion including background events for $p \to \mu^+\eta$, $\eta \to 2\gamma$ can reconstruct masses from two γ-rays around the true pion mass of 135.0 MeV/c^2 as seen in Fig. 5.6. CC pion production events from electron neutrino interactions, on the other hand, include electrons and make three e-like rings. In this case, since the rings originating from two γ-rays cannot be identified explicitly, the pion masses can be mis-reconstructed. Thus, the reconstructed η mass in background events for $p \to e^+\eta$, $\eta \to 2\gamma$ shows a broad distribution around 550 MeV/c^2 in addition to the peak at $\sim$140 MeV/c^2 in Fig. 5.5. Furthermore, single η meson production contributed as the second most background events for both events.

D: Number of Michel Electrons The number of Michel electrons also helps to constrain the number of background events. Since no muon and a single muon is generated

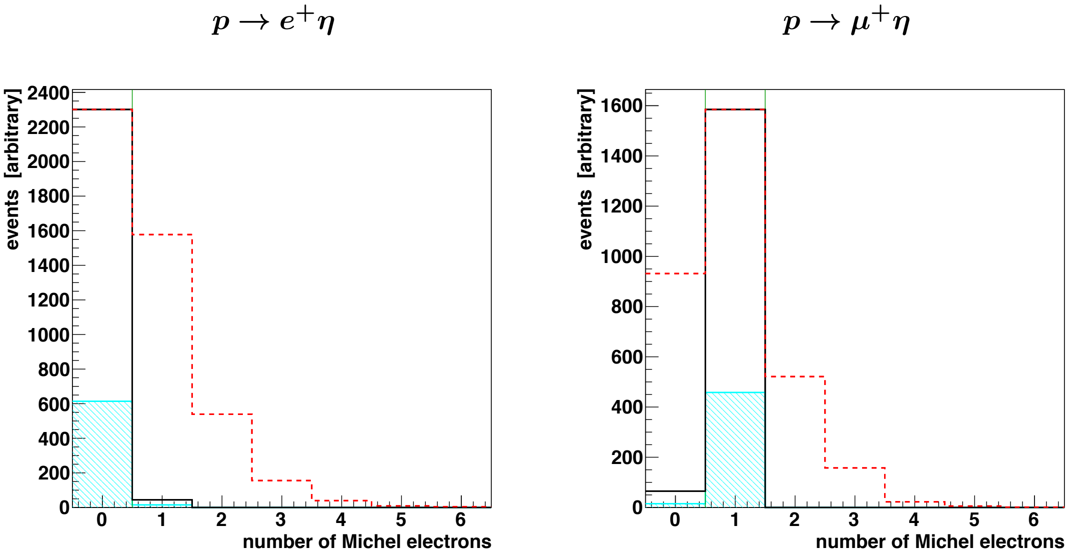

Fig. 5.7: Distributions of the number of Michel electrons of the $p \to e^+\eta$ (left) and $p \to \mu^+\eta$ (right) MC after applying the selection criteria A-C. All of the decay modes of η mesons are considered. The cyan shaded histogram shows the distribution for free protons and the red dashed line shows the distribution of the atmospheric neutrino MC in SK-IV normalized by the maximum bin values. The green solid lines indicate the selection criterion D in Tab. 5.1

in $p \to e^+\eta$ and $p \to \mu^+\eta$ decay respectively, the number of Michel electrons should be zero and one for each mode (criterion D). The number of Michel electrons considering all the decay modes of η mesons after criteria A-C are shown in Fig. 5.7. More than 98% (96%) of the proton decay events from $p \to e^+\eta$ ($p \to \mu^+\eta$) are classified as having no (one) Michel electron.

E, F & G: Reconstructed Total Momentum and Mass The background events of atmospheric neutrino usually do not have isotropic signals because most of the neutrino induced particles are emitted in the direction of movement. This results in background events showing higher total momenta and lower invariant masses than those from true proton decay signals. Hence, the reconstructed momenta and masses are significant clues to distinguish proton decay signals from backgrounds.

The reconstructed total mass and momentum are shown in Fig. 5.8 and Fig. 5.9 respectively for $p \to e^+\eta$ and $p \to \mu^+\eta$ for all η meson decay modes. The peaks in the total mass distributions around 930 MeV/c^2 corresponds to the rest mass of a proton of 938.3 MeV/c^2. From Fig. 5.8, it can be found that event selection with $p_{\rm tot} \leq 100$ MeV/c works especially successful, where more than 99% of the events passed this are proton decay events and most of them derive from free protons.

Against this background, the selection cut of $p_{\rm tot}$ has been set to 250 MeV/c considering the Fermi momentum of bound protons in ^{16}O nucleus (criterion H). In specific, events that satisfies $p_{\rm tot} \leq 100$ MeV/c are considered as signals mainly from free protons and have high significancy as proton decay candidates (criterion I). Besides, only the events fulfilling $800 \leq m_{\rm tot} \leq 1050$ MeV/c^2 are selected as candidates (criterion E).

While pion production events comprise the majority of background events of $p \to e^+\eta$, $\eta \to 2\gamma$ after criterion A-D, those for $p \to \mu^+\eta$, $\eta \to 2\gamma$ include η mesons decaying into two γ-rays. This is because of difference in the distribution of reconstructed neutral pion

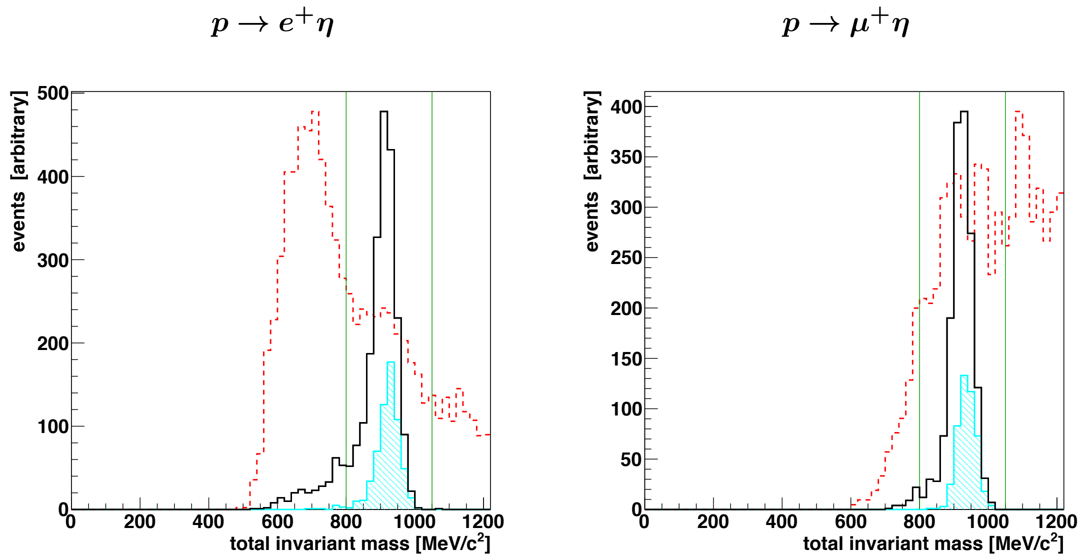

Fig. 5.8: Distributions of reconstructed invariant total mass of the $p \to e^+\eta$ (left) and $p \to \mu^+\eta$ (right) MC after applying the selection criteria A-D. All of the decay modes of η mesons are considered. The cyan shaded histogram shows the distribution for free protons and the red dashed line shows the distribution of the atmospheric neutrino MC in SK-IV normalized by the maximum bin values. The green solid lines indicate the selection criterion E in Tab. 5.1

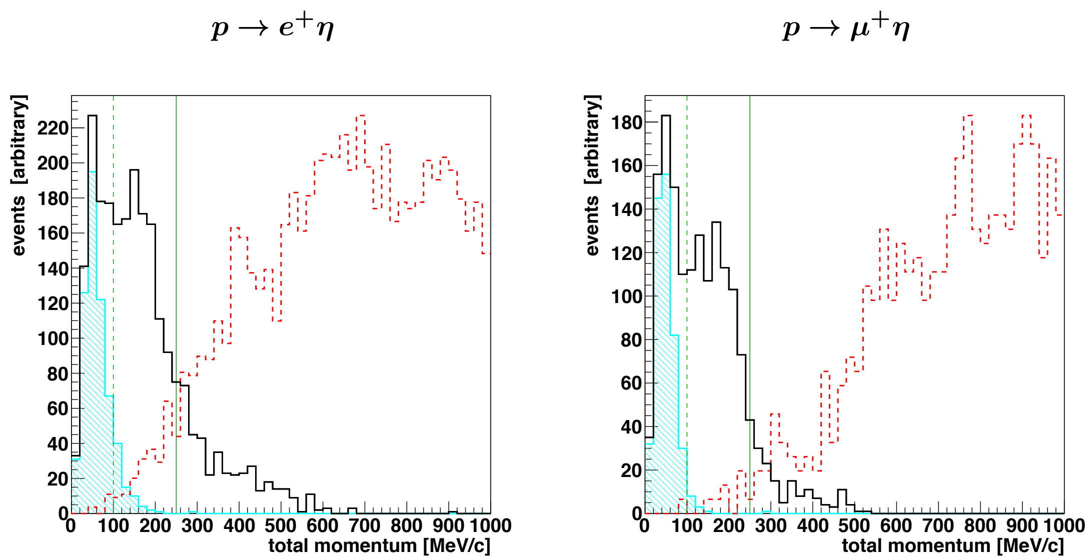

Fig. 5.9: Distributions of reconstructed total momentum of the $p \to e^+\eta$ (left) and $p \to \mu^+\eta$ (right) MC after applying the selection criteria A-D. All of the decay modes of η mesons are considered. The cyan shaded histogram shows the distribution for free protons and the red dashed line shows the distribution of the atmospheric neutrino MC in SK-IV normalized by the maximum bin values. The green solid lines indicate the selection criterion E in Tab. 5.1

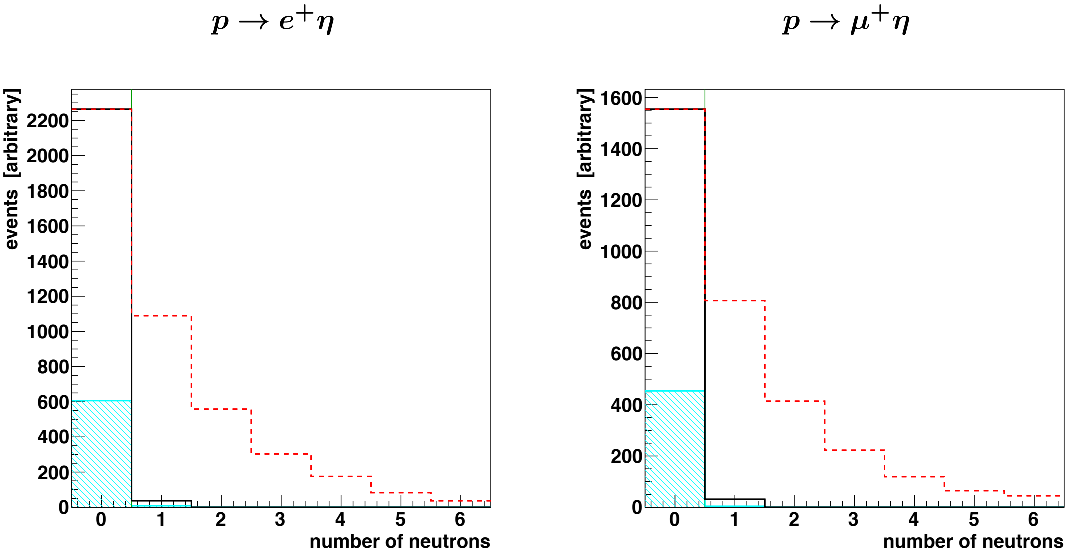

Fig. 5.10: Distributions of the number of neutrons of the $p \to e^+\eta$ (left) and $p \to \mu^+\eta$ (right) MC after applying the selection criteria A-D. All of the decay modes of η mesons are considered. The cyan shaded histogram shows the distribution for free protons and the red dashed line shows the distribution of the atmospheric neutrino MC in SK-IV normalized by the maximum bin values. The green solid lines indicate the selection criteria H and I in Tab. 5.1.

mass as explained in section 5.1.1. Therefore, more background events are reconstructed with total invariant masses with values close to the true proton mass in the analysis of $p \to \mu^+\eta$, $\eta \to 2\gamma$ than that of $p \to e^+\eta$, $\eta \to 2\gamma$ as seen in Fig. 5.8.

H & I: Number of Neutrons The last notable characteristic of proton decay events is the number of neutrons. Neutrons produced in the SK water tank are captured by hydrogens after a few microseconds of travel, followed by emission of a 2.2 MeV prompt γ-ray from the de-excitation of hydrogen. Thus the number of neutrons can be identified by detecting this prompt γ-rays. While neutrino interaction can produce neutrons, oxygen nucleus emits neutrons with a low probability and hydrogen emits no neutron. For these reasons, the information of the number of neutrons is used to select the events; no neutrons should be found in proton decay candidates (criterion H and I). The number of neutrons after criteria A-D are shown in Fig. 5.10. More than 98% (98%) of the proton decay events for $p \to e^+\eta$ ($p \to \mu^+\eta$) are classified as including no neutrons.

5.1.2 Signal Efficiencies and The Number of Background Events

The signal efficiencies are defined as

$$(\text{Signal efficiency of a certain criterion}) = \frac{\text{Number of events passed the criterion}}{\text{Number of } p \to l^+\eta \text{ events after FCFV cut}}, \tag{5.4}$$

and the number of background events have been estimated by normalizing the number of events passed all the event selection criteria in 500 years of atmospheric neutrino MC events to the data live time after the correction of neutrino oscillation effect. Here, the neutrino oscillation probability has been calculated with $\Delta m^2 = 2.5 \times 10^{-3}$ eV^2 and $\sin^2(2\theta) = 1.0$.

Tab. 5.2: Number of events satisfying each event selection criteria of $p \to l^+\eta$, $\eta \to 2\gamma$ mode within 10,000 of $p \to l^+\eta$ events in MC and 500 years of atmospheric neutrino MC events.

	$p \to e^+\eta, \eta \to 2\gamma$		$p \to \mu^+\eta, \eta \to 2\gamma$	
	proton decay MC	atmospheric ν MC	proton decay MC	atmospheric ν MC
FCFV	8023	1771920	8038	1771920
A	4038	145764	3830	145764
B	3635	75490	3067	62600
C	2345	17763	1650	5344
D	2301	8828	1585	2627
E	1816	22	1432	7
F	1065	22	798	6
G	751	0	634	1
H	1046	7	782	6
I	738	0	625	0

Tab. 5.3: Signal efficiencies (ratios) for $p \to l^+\eta$, $\eta \to 2\gamma$ mode against the number of $p \to l^+\eta$ events in MC.

	$p \to e^+\eta,\ \eta \to 2\gamma$	$p \to \mu^+\eta,\ \eta \to 2\gamma$
A	48.8 $\pm$ 0.8%	46.2 $\pm$ 0.7%
B	43.9 $\pm$ 0.7%	37.0 $\pm$ 0.7%
C	28.3 $\pm$ 0.6%	19.9 $\pm$ 0.5%
D	27.8 $\pm$ 0.6%	19.1 $\pm$ 0.5%
E	21.9 $\pm$ 0.5%	17.3 $\pm$ 0.5%
F	12.9 $\pm$ 0.4%	9.6 $\pm$ 0.3%
G	9.1 $\pm$ 0.3%	7.7 $\pm$ 0.3%
H	12.6 $\pm$ 0.4%	9.4 $\pm$ 0.3%
I	8.9 $\pm$ 0.3%	7.5 $\pm$ 0.3%

Tab. 5.4: Number of events and ratios satisfying each event selection criteria of $p \to l^+\eta$, $\eta \to 2\gamma$ mode within 3615 (3553) of $p \to e^+\eta$, $\eta \to 2\gamma$ ($p \to \mu^+\eta$, $\eta \to 2\gamma$) events in MC.

	$p \to e^+\eta, \eta \to 2\gamma$		$p \to \mu^+\eta, \eta \to 2\gamma$	
	number of events	ratio[%]	number of events	ratio[%]
FCFV	3136	100	2984	100
A	2618	83.5 $\pm$ 1.6	2389	80.1 $\pm$ 1.6
B	2396	76.4 $\pm$ 1.6	2078	69.6 $\pm$ 1.5
C	2056	65.6 $\pm$ 1.4	1643	55.1 $\pm$ 1.4
D	2054	65.5 $\pm$ 1.4	1579	52.9 $\pm$ 1.3
E	1674	53.8 $\pm$ 1.3	1427	47.8 $\pm$ 1.3
F	973	31.0 $\pm$ 1.0	796	26.7 $\pm$ 0.9
G	701	22.4 $\pm$ 0.8	631	21.1 $\pm$ 0.8
H	956	30.5 $\pm$ 1.0	780	26.1 $\pm$ 0.9
I	688	21.9 $\pm$ 0.8	622	20.8 $\pm$ 0.8

Tab. 5.5: Breakdown (number of events contribution) of the neutrino interaction modes of the background events in the signal boxes.

Interaction	$p \to e^+\eta,\ \eta \to 2\gamma$	$p \to \mu^+\eta,\ \eta \to 2\gamma$
CC single π production	4	1
CC multiple π production	1	1
NC multiple π production	0	1
CC single η production	1	3
CC quasi-elastic scattering	1	0

The numbers of events that survived each criterion are listed in Tab. 5.2 for 10,000 $p \to l^+\eta$ proton decay MC events and background MC events of 500 years for each decay modes. Table 5.3 shows the efficiencies for each criterion defined above together with statistical errors. The number of background events with statistical errors arose from limited number of MC events are estimated to be 0.13 ± 0.05 (0.08 ± 0.04) for the full SK-IV period for $p \to e^+\eta$ ($p \to \mu^+\eta$). All the MC events are produced by SK-IV period simulation. Selection criteria H and I correspond to the final signal region, and the numbers in the row H and I of Tab. 5.2 and Tab. 5.3 corresponds to the number of proton decay candidates and the final signal efficiencies, respectively. Table 5.4 shows the number of events and ratios extracting only the events decaying in $\eta \to 2\gamma$ after each criterion. It has been shown that around 52% (47%) from $\eta \to 2\gamma$ for $p \to e^+\eta$ ($p \to \mu^+\eta$) MC events can be detected by SK. These inefficiencies are mainly caused by the η nuclear effect explained in section 4. The lower signal efficiency of $p \to \mu^+\eta$ is mainly due to the higher mis-PID rate.

The breakdown of the seven (six) events selected as $p \to e^+\eta$, $\eta \to 2\gamma$ ($p \to \mu^+\eta$, $\eta \to 2\gamma$) candidates from background MC are listed in Tab. 5.5. The majority of the events are accompanied by one or two pions. In the events derived from CC single π production interaction, a charged lepton and the decaying two γ-rays from π^0 generates three rings and create similar signals to those of proton decays. A charged and a neutral pion in the multiple pions production events induced by deep inelastic scattering can also generate three rings. Events of CC single η production interaction with an η meson decaying into two γ-rays also survives the selection criteria. In the rest CCQE induced event, a single electron generates two Cherenkov rings by changing its direction by scattering. These two shower-like rings overlap to be mis-identified as three-ring event.

5.1.3 Confirmation of Data Agreement with MC

The agreement between data and atmospheric neutrino MC events are confirmed before conducting the proton decay search with data. Only the data 100 MeV/c (MeV/c^2) outside the signal region are used so that the final results cannot be seen. Figure 5.11 (Fig. 5.12) shows the scatter diagram of total mass and total momentum, and the distributions of total momentum and total mass are shown as Fig. 5.13 (Fig. 5.14) for $p \to e^+\eta$, $\eta \to 2\gamma$ ($p \to \mu^+\eta$, $\eta \to 2\gamma$) respectively. Criterion A and B are applied and the events inside the black box are not used. No significant difference between data and atmospheric neutrino MC is seen.

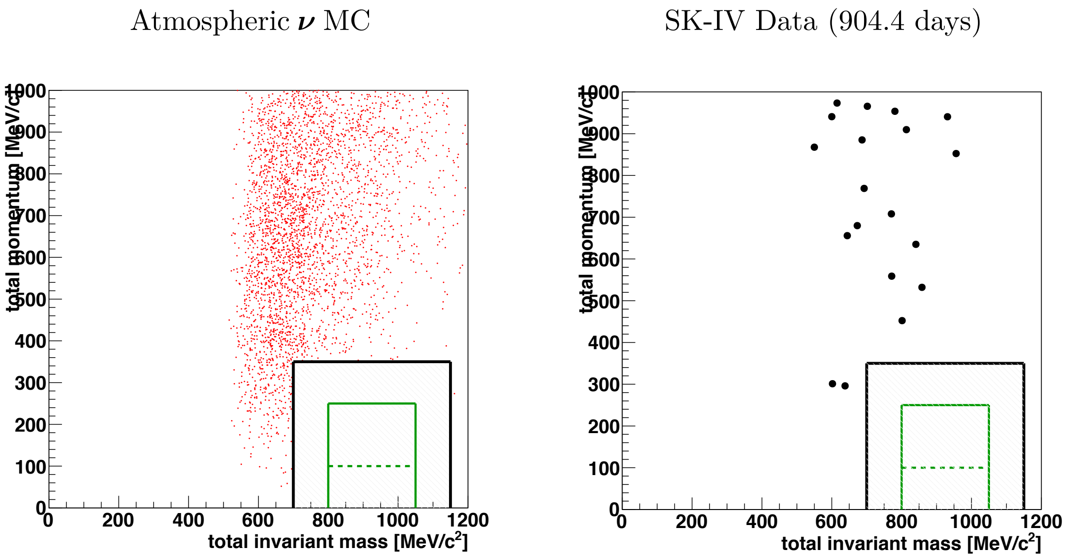

Fig. 5.11: Scatter plots of total mass and total momentum after applying the selection criteria A-D for $p \to e^+\eta$, $\eta \to 2\gamma$ search. The diagram on the left stand for atmospheric neutrino MC events and the right for data from SK-IV period of 905.0 days.

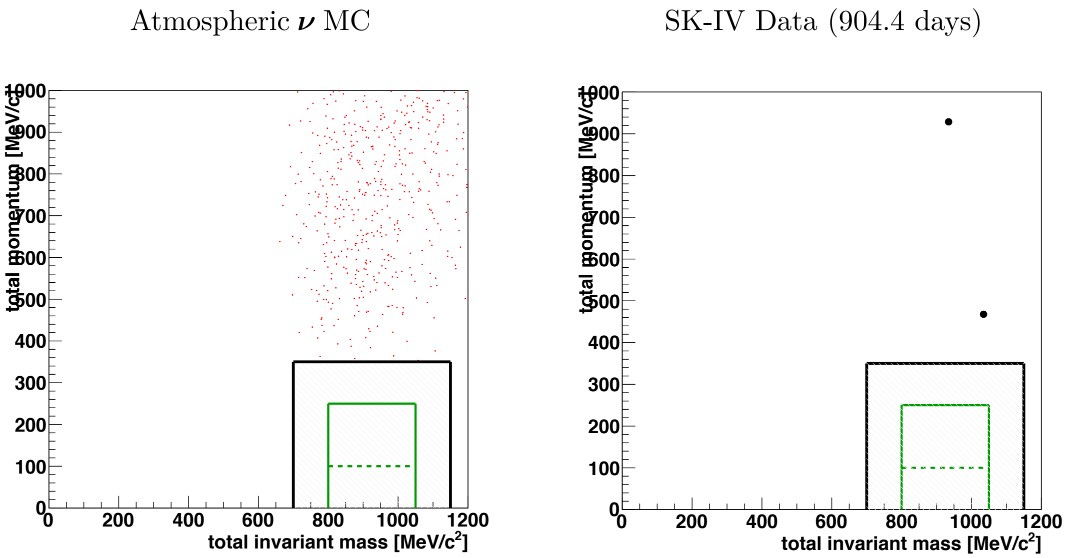

Fig. 5.12: Scatter plots of total mass and total momentum after applying the selection criteria A-D for $p \to \mu^+\eta$, $\eta \to 2\gamma$ search. The diagram on the left stand for atmospheric neutrino MC events and the right for data from SK-IV period of 905.0 days.

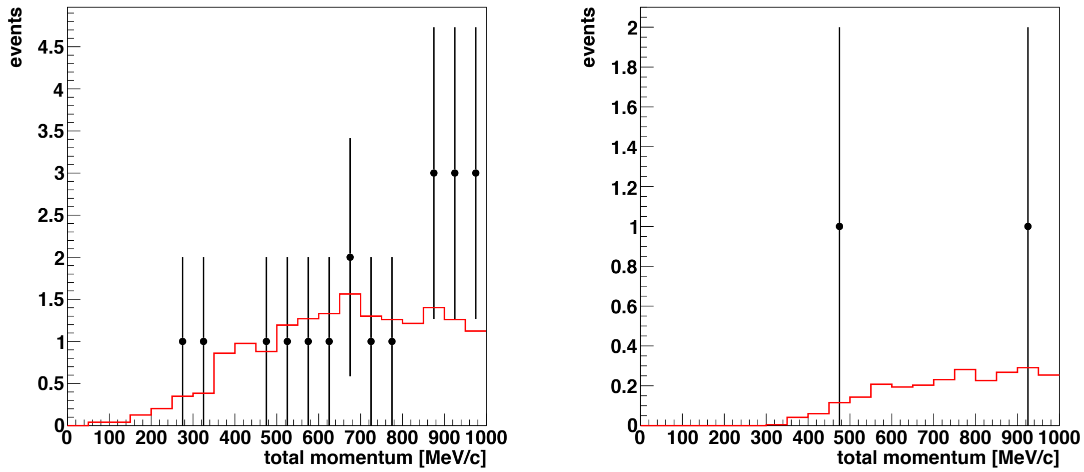

Fig. 5.13: Distributions of reconstructed total momenta outside the signal region after applying the selection criteria A-D for $p \to e^+\eta$ (left) and $p \to \mu^+\eta$ (right). The black circles and red histograms stand for SK-IV data of 905.0 days and for atmospheric neutrino MC events, respectively. The green boxes corresponds to the signal boxes (criterion H and I) and the black box shows the 100 MeV/c (MeV/c^2) outside region from the signal boxes.

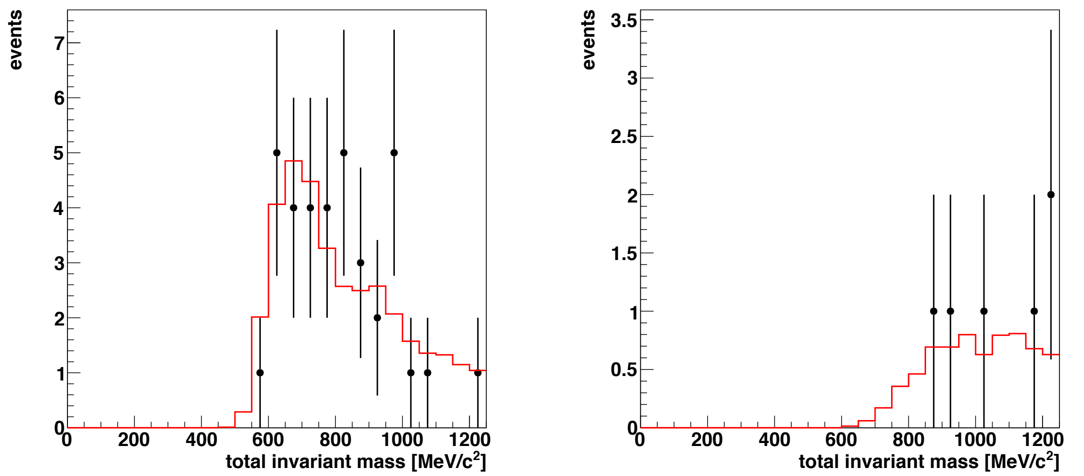

Fig. 5.14: Distributions of reconstructed total masses outside the signal region after applying the selection criteria A-D for $p \to e^+\eta$ (left) and $p \to \mu^+\eta$ (right). The black circles and red histograms stand for SK-IV data of 905.0 days and for atmospheric neutrino MC events, respectively. The green boxes corresponds to the signal boxes (criterion H and I) and the black box shows the 100 MeV/c (MeV/c^2) outside region from the signal boxes.

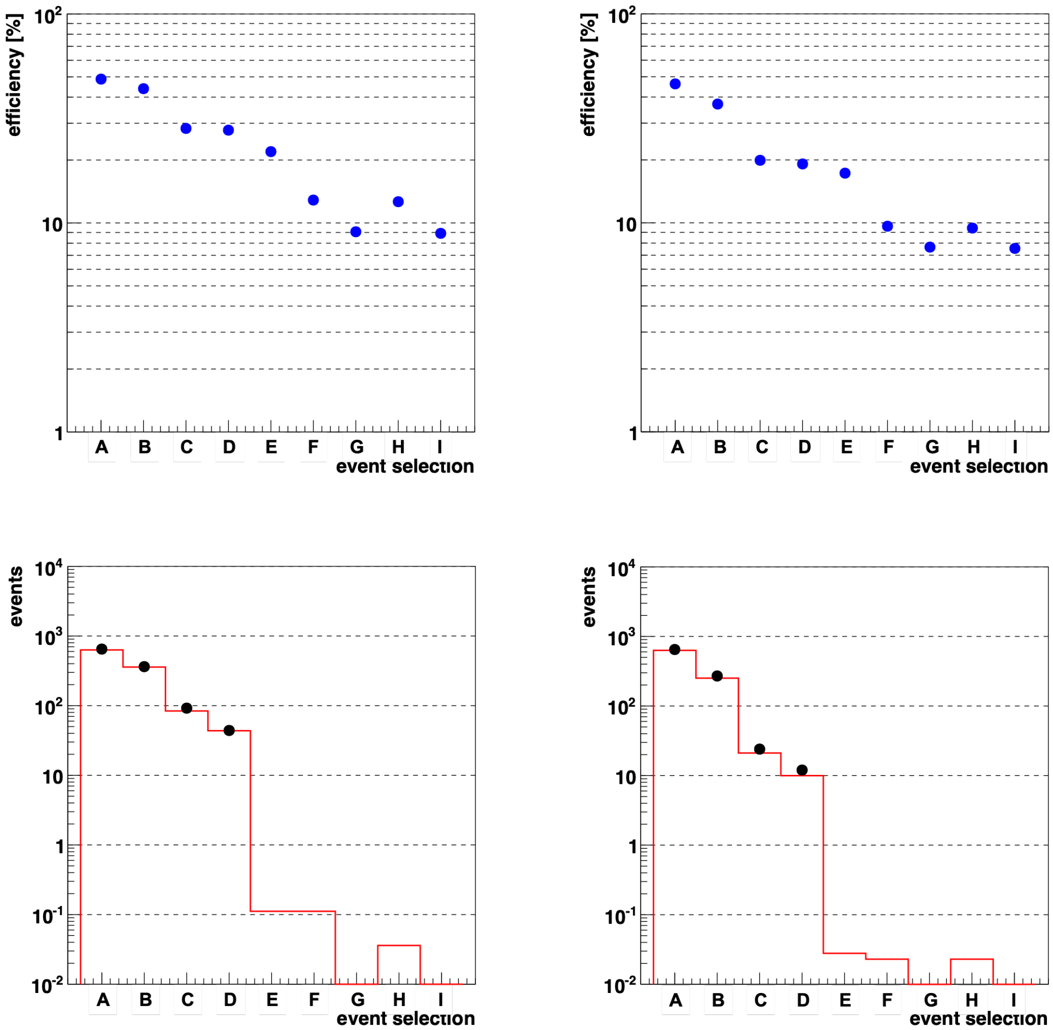

Fig. 5.15: The signal efficiencies (upper) and the number of expected backgrounds (lower, red histogram) and data candidates (lower, black circles) of SK-IV for $p \to e^+\eta$, $\eta \to 2\gamma$ search on the left and $p \to \mu^+\eta$, $\eta \to 2\gamma$ search on the right. The atmospheric neutrino MC are normalized by live time and the data corresponds to the 55.7 kt·years of exposure in SK-IV. The event selection criteria are defined in section 5.1.1.

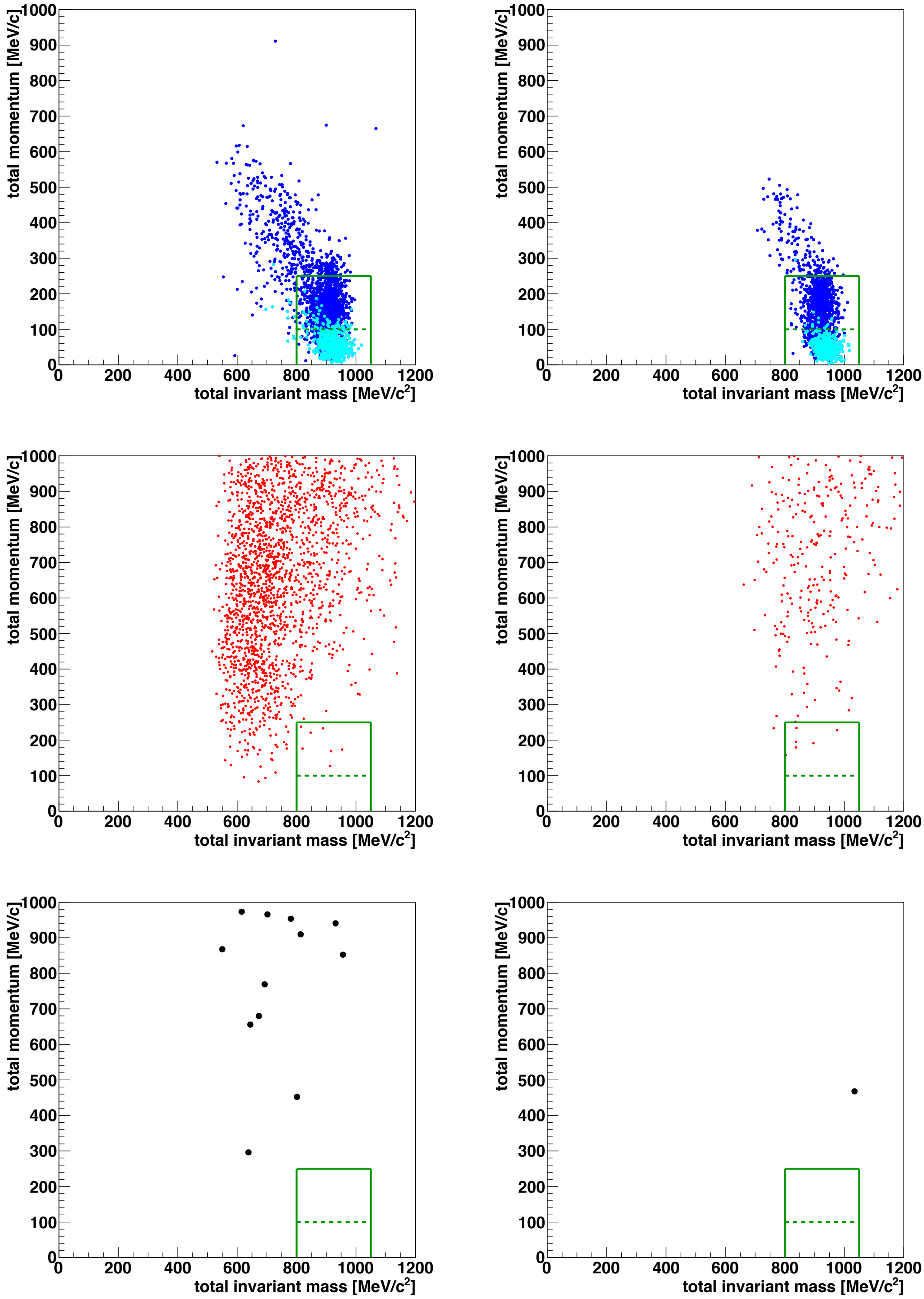

Fig. 5.16: Reconstructed total invariant mass and momentum of proton decay MC (upper), atmospheric neutrino MC (middle), and data (lower) for $p \to e^+\eta$, $\eta \to 2\gamma$ search on the left and $p \to \mu^+\eta$, $\eta \to 2\gamma$ search on the right. The blue and cyan circles in the upper figures show the distribution from all the decay branches of the η meson, and for free proton decay events only, respectively. The red circles in the middle and the black circles in the lower each correspond to the 500 years of atmospheric neutrino MC and the data for 55.7 kt·years of SK-IV period. The green solid and dashed lines indicate the selection criteria E, F, and G in section 5.1.1. All the event selections except E, F and G are applied.

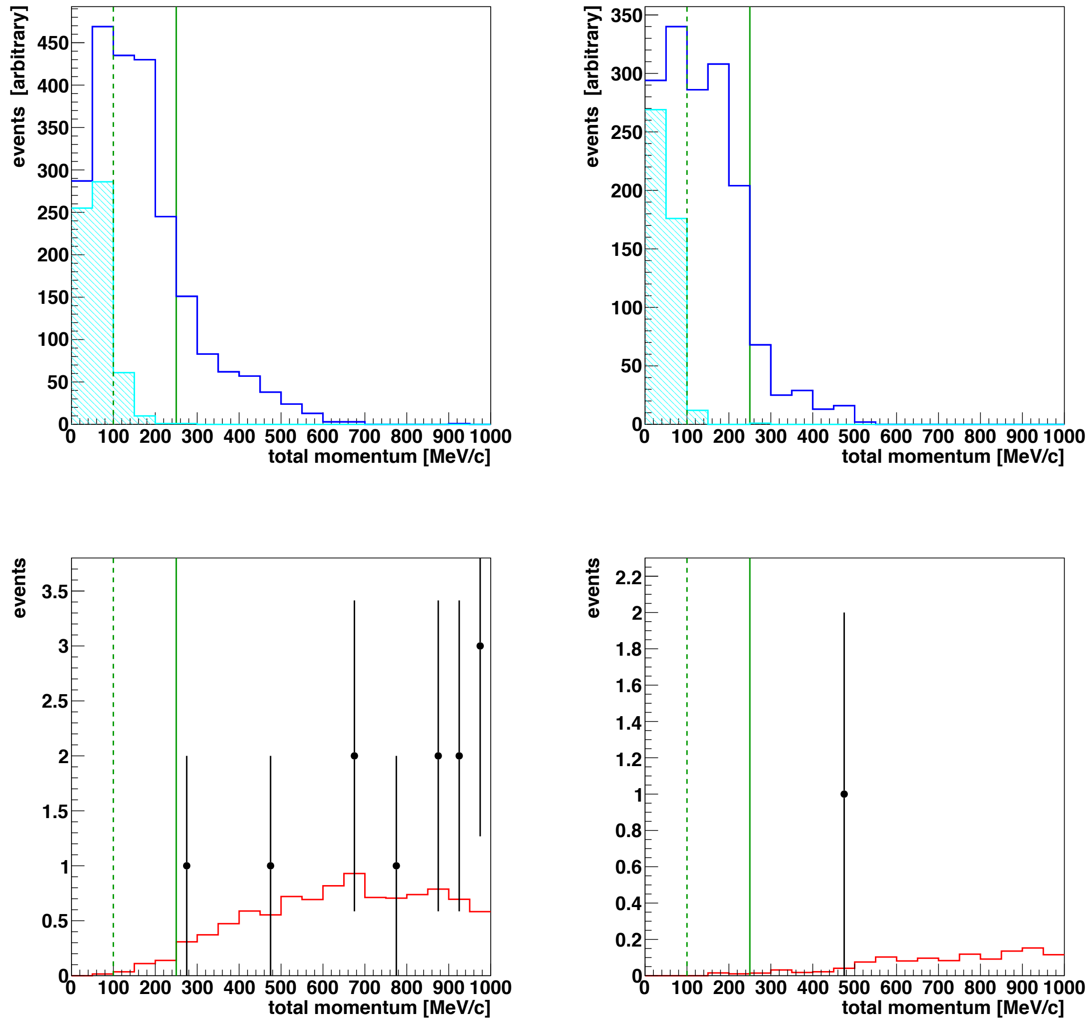

Fig. 5.17: Distributions of reconstructed total invariant momentum of the $p \to l^+\eta$ MC (upper), and atmospheric neutrino MC and data (lower) for $p \to e^+\eta$ search on the left and $p \to e^+\eta$ search on the right. The blue open and shaded cyan histograms in the upper figures show the distribution from all the decay branches of the η meson, and for free proton decay events only, respectively. The red histograms and the black circles in the lower correspond to the atmospheric neutrino MC and the data for 55.7 kt·years of SK-IV period. The green solid and dashed lines indicate the selection criteria F and G in section 5.1.1. All the event selections except E, F, and G are applied.

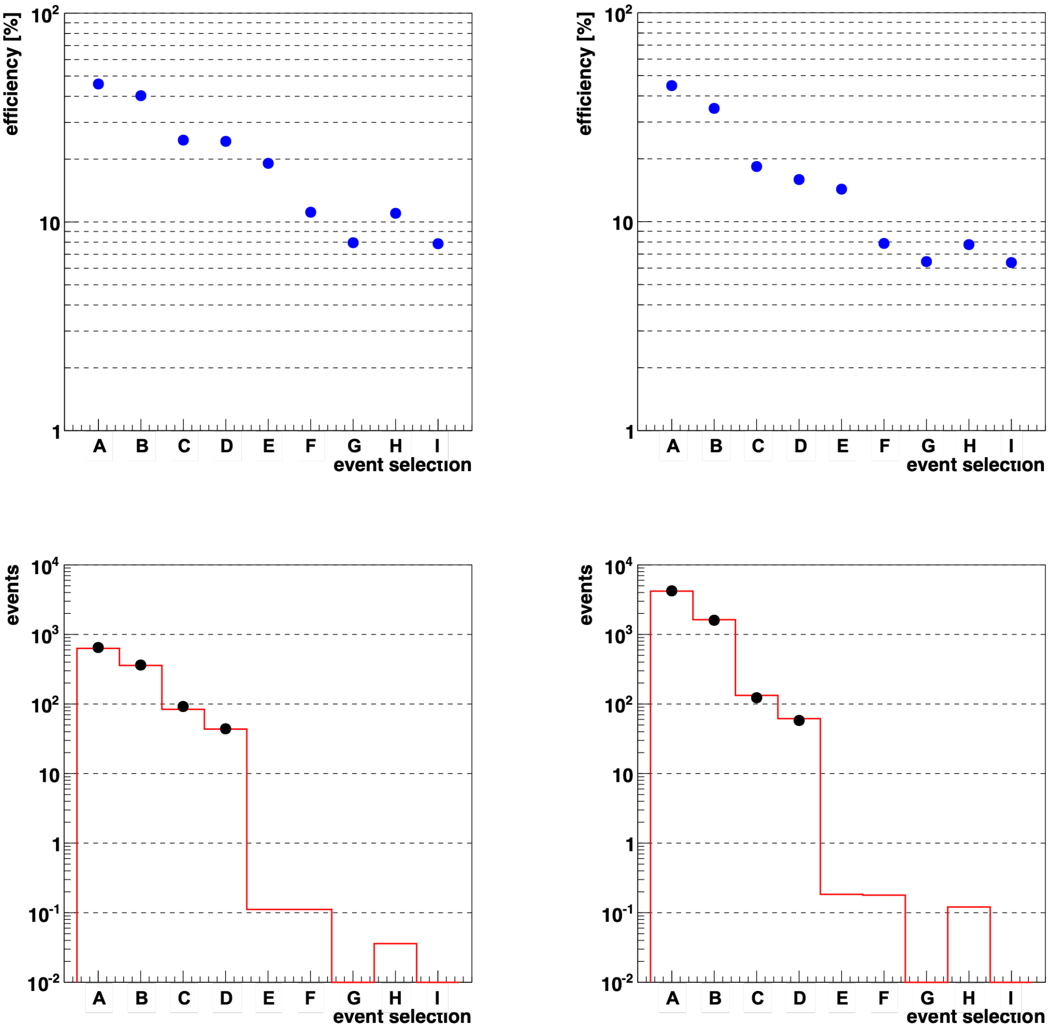

Fig. 5.18: The signal efficiencies (upper) and the number of expected backgrounds (lower, red histogram) and data candidates (lower, black circles) of from SK-I to SK-IV for $p \to e^+\eta$, $\eta \to 2\gamma$ search on the left and $p \to \mu^+\eta$, $\eta \to 2\gamma$ search on the right. All the results from SK-I to SK-IV with 0.373 Mt·years of exposure are combined. The event selection criteria are defined in section 5.1.1.

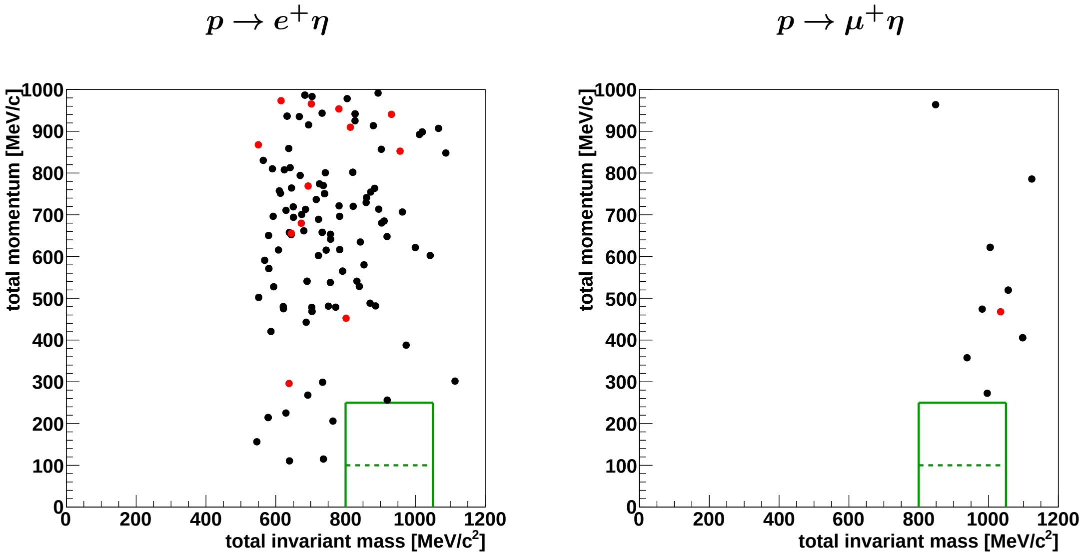

Fig. 5.19: Reconstructed total invariant mass and momentum of the data from SK-I to SK-IV period for $p \to e^+\eta$, $\eta \to 2\gamma$ search on the left and $p \to \mu^+\eta$, $\eta \to 2\gamma$ search on the right. The black and red circles correspond to the results from SK-I to SK-IV in the previous study [29] with 0.316 Mt·years of exposure, and the newly analyzed SK-IV data with 55.7 kt·years of exposure in this study, respectively. All the event selections except E, F, and G are applied.

Tab. 5.6: Summary of the signal efficiencies, the number of expected background events and the number of candidate events from 91.5, 49.1, 31.8, and 199.9 kton·years exposure during SK-I, SK-II, SK-III, and SK-IV periods. The numbers except for those of $p \to l^+\eta, \eta \to 2\gamma$ searches for SK -IV are cited from [29]. The errors of the background events are statistical errors from 500 years of atmospheric neutrino MC for each SK period. The "upper" and "lower" in the $\eta \to 2\gamma$ searches stand for $100 < p_{\mathrm{tot}} < 250$ and $p_{\mathrm{tot}} < 100$, respectively.

	Efficiency [%]				Background [events]				Candidate [events]			
Modes	I	II	III	IV	I	II	III	IV	I	II	III	IV
$p \to e^+\eta$												
(2γ, upper)	11.0	10.9	10.7	12.6	0.17(4)	0.10(2)	0.05(1)	0.13(5)	0	0	0	0
(2γ, lower)	7.9	6.7	8.2	8.9	0.01(1)	0.01(1)	0.003(3)	0.000(10)	0	0	0	0
($3\pi^0$)	8.0	8.2	7.6	7.7	0.15(3)	0.06(2)	0.06(1)	0.04(3)	0	0	0	0
$p \to \mu^+\eta$												
(2γ, upper)	7.3	6.5	7.2	9.4	0.05(2)	0.02(1)	0.01(1)	0.08(4)	0	0	0	0
(2γ, lower)	5.8	5.6	6.0	7.5	0.000(6)	0.000(4)	0.000(3)	0.000(10)	0	0	0	0
($3\pi^0$)	6.9	6.2	6.9	7.9	0.34(5)	0.13(2)	0.12(2)	0.22(6)	0	1	0	1

Tab. 5.7: Summary of the systematic uncertainties (percentage contribution) on signal efficiencies for each factors for SK-IV period. The numbers except for the η nuclear effect of $p \to l^+\eta, \eta \to 2\gamma$ searches for SK-IV are cited from [29]. The "upper" and "lower" in the $\eta \to 2\gamma$ searches stand for $100 < p_{\mathrm{tot}} < 250$ and $p_{\mathrm{tot}} < 100$, respectively.

Modes	η nuclear effect	N-N correlated decay	Fermi momentum	Detector performances	Total
$p \to e^+\eta$					
(2γ, upper)	10	8	9	2	16
(2γ, lower)	4	3	13	2	14
($3\pi^0$)	12	4	15	4	20
$p \to \mu^+\eta$					
(2γ, upper)	10	9	10	3	17
(2γ, lower)	4	3	12	3	13
($3\pi^0$)	17	6	2	5	19

5.1.4 Results

The proton decay events for $p \to e^+\eta$, $\eta \to 2\gamma$ and $p \to \mu^+\eta$, $\eta \to 2\gamma$ are searched for 55.7 kton $\cdot$ years of SK-IV data with the selection criteria in Tab. 5.1. Figure 5.15 shows the signal efficiencies, the number of background events, and the number of candidates in data. The distribution of the data candidates and that of expected background events agree well. The total invariant mass and total momentum distributions are shown in Fig. 5.16 and Fig. 5.17 for proton decay MC, atmospheric neutrino MC, and SK-IV data. The number of background events in the signal boxes for 55.7 kton $\cdot$ years exposure are expected to be 0.034 (0.000) events for the upper and 0.022 (0.000) events for the lower box for $p \to e^+\eta$, $\eta \to 2\gamma$ ($p \to \mu^+\eta$, $\eta \to 2\gamma$). No event is found in the signal boxes; No proton decay candidate is found.

The results for $p \to l^+\eta$, $\eta \to 2\gamma$ modes from SK-I to SK-IV combined from the previous study [29] are shown in Fig. 5.18 and Fig. 5.19. No candidate is found through SK-I to SK-IV period. All the signal efficiency, the number of expected background events, and the number of data candidate events for each SK period are summarized in Tab. 5.6. The numbers of $\eta \to 2\gamma$ except for SK-IV period and those of $\eta \to 3\pi^0$ are cited from [29]. Two candidates were found for $p \to \mu^+\eta$, $\eta \to 3\pi^0$ search in the previous study. The probability to observe more than two candidates was calculated by the expected background events of Poisson statistics without considering systematic errors. The Poisson probability of observing two events for $p \to \mu^+\eta$, $\eta \to 3\pi^0$ was deduced to be 20.9%.

5.2 Systematic Uncertainties

The systematic uncertainties on signal efficiency and the number of expected background events are described in this section. The uncertainties discussed in section 4 are applied as the systematic errors coming from η nuclear effect for SK-IV period. The other uncertainties are cited from the latest research [29]. Each error sources are summarized in Tab. 5.7 and Tab. 5.8.

5.2.1 Systematic Uncertainties on Signal Efficiency

(1) η Nuclear Effect

The systematic uncertainties arising from η nuclear effect of SK-IV period are estimated by the relative variations of the number of events without experiencing nuclear effect in ^{16}O nucleus as described in section 4. These estimated values in Eq. (4.31) and Eq. (4.32) are adopted for the systematic uncertainties of upper signal boxes, whereas those of lower signal boxes are estimated to be 0.35 times the error of upper ones. This is because the fractions of bound proton in the lower boxes are around 35%. For SK-I to SK-III period, uncertainties are taken from [29].

(2) N-N Correlated Decay

Around 10% [48] of the bound protons in ^{16}O nucleus are affected by other nucleons in the same ^{16}O nucleus as described in section 3.1. This effect can make another nucleon to recoil together with the decaying proton. Thus, this decay is considered as three body decay with low signal efficiency. The systematic uncertainty is estimated by the fluctuation of the number of events in the signal box with 100% uncertainty of the effect of correlated decay.

(3) Fermi Momentum

The proton momentum is simulated by a spectral function from electron scattering experiment in ^{12}C [47]. The proton momentum distribution in atmospheric neutrino MC, on the other hand, is calculated based on the Fermi gas model. Therefore, the difference between the number of events in the signal box based on the spectral function and the Fermi gas model is considered as uncertainties.

(4) Detector Performances

The uncertainties related to event reconstruction are combined as the systematic errors from detector performances. A total of six error sources is included: vertex position, the number of Cherenkov rings, particle identification (ring pattern), the number of Michel electrons, and the energy scale. The detail of this information is described in section 2.2.

5.2.2 Systematic Uncertainties on the Number of Background Events

The uncertainties from atmospheric neutrino flux, neutrino cross section, meson nuclear effect, and impact of hadron propagation in water are considered for the background estimations. The systematic uncertainty due to detector performances is also evaluated as well as that of signal efficiencies. The background estimation errors are considered to be the same for both lower and upper signal boxes for $\eta \to 2\gamma$ decay. All of the values of each error source have been taken from [29].

(1) Meson Nuclear Effect

Pions and η mesons generated by neutrino interaction in ^{16}O can interact with ^{16}O nucleus. Due to this nuclear effect, the mesons get absorbed or scattered by the nucleon. In this study, the systematic uncertainty of the π nuclear effect and η nuclear effect are evaluated. The former is taken from reference [29] evaluated by tuning the parameters of the interaction model of π-scattering experiment data [76] within 1σ uncertainty. The uncertainty is adopted as 12% (14%) for $p \to e^+\eta$, $\eta \to 2\gamma$ ($p \to \mu^+\eta$, $\eta \to 2\gamma$) mode. These parameters are the interaction probabilities of quasi-elastic scattering and charge exchange, inelastic scattering, and absorption. Around 60% of the background events are simulated to originate from pion productions as indicated in Tab. 5.5. The latter estimated from Eq. (4.31) and Eq. (4.31) are about 10% for $p \to l^+\eta$, $\eta \to 2\gamma$ decays, which are comparable to the ones of pion nuclear effect. About 30% of the background events include single η meson. Since more than 90% of the background events are accompanied by mesons, 12% (14%) is adopted as a error source of meson nuclear effect for all background events of ($p \to \mu^+\eta$, $\eta \to 2\gamma$) search.

(2) Hadron Propagation in Water

Charged pions can be generated by neutrino interactions and strongly interact with nucleons. This effect of hadron propagation in water is evaluated by both the simulated and measured cross section of charged pions in water from [77, 78] with 100% uncertainty.

(3) Neutrino Flux

The systematic uncertainty of neutrino flux is evaluated by the atmospheric neutrino data analyses in SK described in [79, 80]. Several error sources listed below are taken into account.

- Energy dependent normalization
- Neutrino flavor ratio
- $\bar{\nu}/\nu$ ratio
- Up/down asymmetry
- Horizontal/vertical ratio
- K/π production ratio
- Neutrino flight length

The dominant factor for the neutrino flux error is the energy-dependent normalization.

(4) Neutrino Cross Section

The systematic uncertainty of neutrino cross section is also evaluated by atmospheric neutrino data analyses in SK [79, 80]. Each of the error sources is shown below.

- M_A (axial vector mass) in quasi-elastic scattering and single-meson production
- Quasi-elastic scattering for bound nucleons (total cross section)
- Quasi-elastic scattering for bound nucleons ($\bar{\nu}/\nu$)
- Quasi-elastic scattering for bound nucleons (flavor ratio)
- Single(multi)-meson production (total cross section)
- Single(multi)-meson production (model dependence)
- Coherent pion production
- NC/CC ratio

(5) Detector Performances

The uncertainties related to event reconstruction are all combined as the systematic errors from detector performances. A total of seven error sources is included: fiducial volume,

Tab. 5.8: Summary of the systematic uncertainties (percentage contribution) on the number of background events for each factors for SK-IV period. All the numbers are cited from [29]. The "upper" and "lower" in the $\eta \rightarrow 2\gamma$ searches stand for $100 < p_{\mathrm{tot}} < 250$ and $p_{\mathrm{tot}} < 100$, respectively.

Modes	Neutrino flux	Neutrino cross section	Meson nuclear effect	Hadron propagation in water	Detector performances	Total
$p \rightarrow e^+\eta$						
(2γ, upper)	8	15	12	5	21	30
(2γ, lower)	8	15	12	5	21	30
($3\pi^0$)	8	12	34	17	30	51
$p \rightarrow \mu^+\eta$						
(2γ, upper)	9	15	14	8	28	37
(2γ, lower)	9	15	14	8	28	37
($3\pi^0$)	8	12	9	13	12	25

detector non-uniformity, energy scale, particle identification (ring pattern), the number of Cherenkov rings, the number of Michel electrons, and neutron tagging. The detail of this information is described in section 2.2.

5.3 Lifetime Limits

The lower limits of the proton's partial lifetime are calculated by the Bayesian method. In this study, the results from 12 independent searches are conducted for $p \to l^+\eta$ decay: the lower and upper box analysis for $p \to l + \eta,\ \eta \to 2\gamma$ for SK-I to SK-IV, and the $p \to l + \eta,\ \eta \to 3\pi^0$ for SK-I to SK-IV.

5.3.1 Lifetime Estimation

The probability of detecting n events of proton decay is given as Poisson statistics:

$$\mathbf{P}(n|\Gamma\lambda\epsilon b) = \frac{e^{-(\Gamma\lambda\epsilon+b)}(\Gamma\lambda\epsilon + b)^n}{n!}, \tag{5.5}$$

where Γ is the decay rate, λ is the exposure, ϵ is the signal efficiency, and b is the number of background event. From the Baye's theorem, Eq. (5.5) can be transformed as

$$\begin{aligned}\mathbf{P}(\Gamma\lambda\epsilon b|n) &= \frac{1}{\mathbf{P}(n)}\mathbf{P}(n|\Gamma\lambda\epsilon b) \cdot \mathbf{P}(\Gamma\lambda\epsilon b), && (5.6)\\ &= \frac{1}{\mathbf{P}(n)}\mathbf{P}(n|\Gamma\lambda\epsilon b) \cdot \mathbf{P}(\Gamma) \cdot \mathbf{P}(\lambda) \cdot \mathbf{P}(\epsilon) \cdot \mathbf{P}(b), && (5.7)\end{aligned}$$

where the second line is derived from the assumption that Γ, λ, ϵ and b are all independent. Here, the probability density function of Γ is

$$\begin{aligned}\mathbf{P}(\Gamma|n) &= \iiint \mathbf{P}(\Gamma\lambda\epsilon b|n)\ d\epsilon d\lambda db, && (5.8)\\ &= \frac{1}{A}\iiint \frac{e^{-(\Gamma\lambda\epsilon+b)}(\Gamma\lambda\epsilon + b)^n}{n!}\mathbf{P}(\Gamma) \cdot \mathbf{P}(\lambda) \cdot \mathbf{P}(\epsilon) \cdot \mathbf{P}(b)\ d\epsilon d\lambda db, && (5.9)\end{aligned}$$

where A is the normalization constant defined as

$$A = \int_0^\infty \mathbf{P}(\Gamma|n)\ d\Gamma. \tag{5.10}$$

The probabilities $\mathbf{P}(\lambda)$ and $\mathbf{P}(\epsilon)$ are assumed to be Gaussians;

$$\mathbf{P}(\lambda) \propto \begin{cases} \exp\left(-\frac{(\lambda-\lambda_0)^2}{2\sigma_\lambda^2}\right) & (\lambda > 0) \\ 0 & (\lambda \le 0) \end{cases} \tag{5.11}$$

$$\mathbf{P}(\epsilon) \propto \begin{cases} \exp\left(-\frac{(\epsilon-\epsilon_0)^2}{2\sigma_\epsilon^2}\right) & (\epsilon > 0) \\ 0 & (\epsilon \le 0) \end{cases} \tag{5.12}$$

where λ_0 (σ_λ), ϵ_0 (σ_ϵ), b_0 (σ_b) are the estimations (systematic errors) for exposure, signal efficiency, and the number of background, respectively. The systematic errors of exposure are set to be 0.01 kton·years. When the number of background b is low (less than around

10), a convolution of Poisson and Gaussian distribution should be adopted for the probability of the number of background to take the statistical error into account. Therefore, $\mathbf{P}(b)$ is expressed as

$$\mathbf{P}(b) \propto \int_0^\infty \frac{e^{-B}(B)_b^n}{n_b!} \cdot \exp\left(-\frac{(bC-B)^2}{2\sigma_b^2}\right) dB. \tag{5.13}$$

Here n_b is the number of events in 500 years of atmospheric neutrino MC, B is the number of true background events in 500 years of atmospheric neutrino MC, C is the normalization constant for MC live time to the data live time, and σ_b is the systematic error of the number of background.

The relationship between the lower limit of the decay rate, Γ_{limit} and the confidence level $C.L.$ is

$$C.L. = \int_0^{\Gamma_{\text{limit}}} \mathbf{P}(\Gamma|n)\, d\Gamma, \tag{5.14}$$

and the the lower limit of lifetime is defined as;

$$\tau/B = \frac{1}{\Gamma_{\text{limit}}}. \tag{5.15}$$

The probability to detect n_i events in the i-th independent proton decay search is given as the product of each Poisson probabilities

$$\mathbf{P}(n_1 \cdots n_s|\Gamma\lambda_1\epsilon_1 b_1 \cdots \Gamma\lambda_s\epsilon_s b_s) = \prod_{i=1}^{s} \mathbf{P}(n_i|\Gamma\lambda_i\epsilon_i b_i) \tag{5.16}$$

$$= \frac{e^{-(\Gamma\lambda_1\epsilon_1+b_1)}(\Gamma\lambda_1\epsilon_1+b_1)_1^n}{n_1!} \times \cdots \times \frac{e^{-(\Gamma\lambda_s\epsilon_s+b_s}(\Gamma\lambda_s\epsilon_s+b_s)_s^n}{n_s!}, \tag{5.17}$$

where s is the number of independent searches, λ_i, ϵ_i and b_i are the exposure, signal efficiency and the number of background in SK-i period. Therefore, the lower limit of decay rate for the combined period searches is

$$0.9 = \int_0^{\Gamma_{\text{limit}}} \prod_{i=1}^{s} \mathbf{P}(\Gamma|n_i)\, d\Gamma. \tag{5.18}$$

5.3.2 Final Results

The lifetime limits are calculated by combining the three different search methods for four different SK periods. For each $p \to l^+\eta$ search, there are three methods: two for the lower and upper box analysis for $\eta \to 2\gamma$ and one for $\eta \to 3\pi^0$, with four SK periods. Therefore, 12 independent searches are combined to estimate the limit for $p \to l^+\eta$. The searches for $p \to l^+\eta$, $\eta \to 2\gamma$ lower and upper box analysis for SK-IV period are updated in this study with new data, signal efficiencies, and systematic errors. The results of the other 20 searches are cited from [29].

The lifetime limit for $p \to l^+\eta$ at 90% confidence level are summarized in Tab. 5.9. The updated factors compared to the previous study in this thesis are

- Extend exposure from 0.317 Mton·years→0.373 Mton·years for $p \to l^+\eta$, $\eta \to 2\gamma$

Tab. 5.9: Impact of signal efficiencies and their systematic errors on lifetime limit. The numbers in the second row are cited from [29].

	Lifetime limit at 90% CL [$\times 10^{33}$ years]	
Modes	$p \to e^+\eta$	$p \to \mu^+\eta$
Previous study [29]	10.4	4.7
Extended SK-IV data	11.6	5.4
with updated systematic errors	12.1	5.8
with updated signal efficiencies	13.3	6.1

Tab. 5.10: Summary of proton decay search of $p \to l^+\eta$.

Modes	Background [events]	Candidate [events]	Probability [%]	Lifetime limit at 90% CL
$p \to e^+\eta$	0.84 ± 0.32	0	$\cdots$	13.3×10^{33} years
$p \to \mu^+\eta$	0.93 ± 0.25	2	20.9	6.1×10^{33} years

- Reduced the systematic errors on signal efficiencies by a factor of two for $p \to l^+\eta$, $\eta \to 2\gamma$ in SK-IV period
- Increased the signal efficiencies by 2.8% (1.0%) for the upper box analysis and 1.4% (0.5%) for the lower box analysis of $p \to e^+\eta,\ \eta \to 2\gamma$ ($p \to \mu^+\eta,\ \eta \to 2\gamma$) in SK-IV period

As shown in Tab. 5.9, the extended exposure, updated systematic errors, and the updated signal efficiencies extend the lifetimes by around 11%(15%), 4%(7%), and 10%(5%), respectively for $p \to e^+\eta$ ($p \to \mu^+\eta$). The summary of the proton decay search is shown in Tab. 5.10. As overall, the lower limit of partial proton lifetime for $p \to e^+\eta$ ($p \to \mu^+\eta$) have increased by 28% (30%) with lifetimes of

$$\tau/B_{p\to e^+\eta} = 13.3 \times 10^{33} \text{ years at 90\% C.L.,} \tag{5.19}$$

$$\tau/B_{p\to \mu^+\eta} = 6.1 \times 10^{33} \text{ years at 90\% C.L..} \tag{5.20}$$

Chapter 6

Discussion and Conclusion

6.1 Comparison with GUT models

As discussed in section 1.2.4, several GUT models suggest that the proton decay $p \to l^+\eta$ occurs with a substantial branching ratio. The lower limits on the lifetime for the $p \to e^+\eta$ mode estimated by four GUT models [22–25] are

$$\mathrm{SU}(5)\ [22] \quad : \quad \sim 3 \times 10^{32} \text{ years} \tag{6.1}$$

$$\mathrm{SU}(5)\ [23] \quad : \quad \sim 3 \times 10^{32} \text{ years} \tag{6.2}$$

$$\mathrm{SU}(5)\ [24] \quad : \quad \sim 7 \times 10^{32} \text{ years} \tag{6.3}$$

$$\mathrm{SO}(10)\ [25] \quad : \quad \sim 1 \times 10^{35} \text{ years.} \tag{6.4}$$

The above lifetimes are estimated by the expected lifetime of the proton divided by the branching ratio of $p \to e^+\eta$ mode. By contrast, the lower limit on the lifetime of the $p \to e^+\eta$ mode estimated in this work is

$$\tau/B_{p\to e^+\eta} = 13.3 \times 10^{33} \text{ years at 90\% C.L..} \tag{6.5}$$

This represents the most stringent experimental limit reported so far, and excludes the SU(5) models of [22–24].

6.2 Conclusion

The proton decay search into a charged antilepton plus an eta meson and the eta meson into two gamma-rays have been updated to include improved nuclear effect estimation, signal efficiencies, systematic errors for SK-IV period, and an additional 55.7 kton·years exposure of SK-IV data. As for the newly analyzed 55.7 kton·years data, no evidence of $p \to l^+\eta,\ \eta \to 2\gamma$ is found in this study. The partial lifetimes of protons via $p \to l^+\eta$ are estimated based on Bayes' theorem by using total of 0.373 Mton·years exposure from SK-I to SK-IV including the results from [29]. The lower limits at 90% confidence level are calculated as below.

$$\tau/B_{p\to e^+\eta} = 13.3 \times 10^{33} \text{ years at 90\% C.L.,}$$
$$\tau/B_{p\to \mu^+\eta} = 6.1 \times 10^{33} \text{ years at 90\% C.L..}$$

The limits of $p \to e^+\eta$ and $p \to \mu^+\eta$ have extended by 33% and 29% respectively from the previous study [29]. These results set the most stringent limits in the world.

6.3 Future Prospects

In this study, due to the re-estimation of the cross section of η nuclear effect, improvement of the signal efficiencies and the systematic errors of $p \to l^+\eta, \eta \to 2\gamma$ are demonstrated for SK-IV data. This re-estimation will also be applied to both the rest of SK-I, II and III data for $p \to l^+\eta, \eta \to 2\gamma$ search, and the $p \to l^+\eta, \eta \to 3\pi^0$ search for SK-I to SK-IV data with additional data. With all of these updates, the lifetime limit can roughly estimated to be $\sim 20 \times 10^{33}$ years ($\sim 10 \times 10^{33}$) for $p \to e^+\eta$ ($p \to \mu^+\eta$) mode.

SK is now running as a new phase, SK-Gd, with Gadolinium (Gd) dissolved in water. Gd increases the capture efficiency of neutrons, and thus the neutron tagging technology has improved. This phase has started from August 2020 and the atmospheric neutrino background events are expected to decrease, which can contribute to the better sensitivity of proton decay searches. In addition, the Hyper-Kamiokande project (HK) [81], the successor to SK, have started its construction planning to operate in 2027. The magnitude is planned to be 10 times larger than of SK consisting of a cylindrical water tank of 74 m diameter and 60 m height, 40,000 PMTs and 260 kton of pure water. HK is expected to contribute to proton decay analysis with such high statistics.

Acknowledgements

My profound gratitude goes first to my supervisor, Professor Masashi Yokoyama, for all the continuous support during my Master ’ s course. His enthusiasm towards physics had led me to join the Super-Kamiokande experiment and his invaluable advice allowed me to complete this thesis.

I am deeply indebted to Makoto Miura and Shunichi Mine who generously gave me their support. They taught me how to carry out research without hesitation. My analysis would never have been accomplished without their insightful comments and suggestions.

I am grateful to all of the members in Super-Kamiokande collaboration, especially to the following people: Yoshinari Hayato, Roger Wendell, Takuya Tashiro, Masaki Ishitsuka, Hidekazu Tanaka, Yasuhiro Nishimura, Akira Takenaka and Ryo Matsumoto.

My appreciation also extends to all the laboratory colleagues. Thanks go to Konosuke Iwamoto and Kota Nakagiri for being supportive not only for this study but also for building skills as a physicist. My friends, Aoi Eguchi, Haruto Kikutani, Kohei Matsushita, Yoshimi Yoshimoto had encouraged each other and made my time at The University of Tokyo enjoyable.

Finally, sincere thanks to my family for their considerations, encouragements and emotional support for years, and my beloved dog, Chiffon, for always having been with me, which are the most essential to accomplish this big goal.

Bibliography

[1] S. Weinberg, *A Model of Leptons*, Physical Review Letters **19**, 1264–1266 (1967).

[2] A. Salam, *Weak and Electromagnetic Interactions*, Conf. Proc. C **680519**, 367–377 (1968).

[3] M. Thomson, *Modern particle physics*, Cambridge University Press, (2013).

[4] F. Englert and R. Brout, *Broken Symmetry and the Mass of Gauge Vector Mesons*, Phys. Rev. Lett. **13**, 321–323 (1964).

[5] P.W. Higgs, *Broken Symmetries and the Masses of Gauge Bosons*, Phys. Rev. Lett. **13**, 508–509 (1964).

[6] H. Nishino, *Search for Nucleon Decay into Charged Antilepton plus Meson in Super-Kamiokande*", Ph.D. thesis, The University of Tokyo (2009).

[7] H. Georgi and S.L. Glashow, *Unity of all elementary-particle forces*, Physical Review Letters **32**, 438–441 (1974).

[8] P. Langacker, *Grand Unification and the Standard Model*, 1–22 (1994).

[9] K. Hirata, T. Kajita, T. Kifune *et al.*, *Experimental limits on nucleon lifetime for lepton+meson decay modes*, Physics Letters B **220**, 308–316 (1989).

[10] C. McGrew, R. Becker-Szendy, C.B. Bratton *et al.*, *Search for nucleon decay using the IMB-3 detector*, Physical Review D - Particles, Fields, Gravitation and Cosmology **59**, 3–8 (1999).

[11] C. Berger, A. Hofmann, H. Mönch *et al.*, *The Fréjus nucleon decay detector*, Nuclear Instruments and Methods in Physics Research Section A: Accelerators, Spectrometers, Detectors and Associated Equipment **262**, 463–495 (1987).

[12] P. Nath and P. Fileviez Pérez, *Proton stability in grand unified theories, in strings and in branes*, Physics Reports **441**, 191–317 (2007).

[13] U. Amaldi, W. d Boer, and H. Fürstenau, *Comparison of grand unified theories with electroweak and strong coupling constants measured at LEP*, Physics Letters B **260**, 447–455 (1991).

[14] J. Ellis, S. Kelley, and D.V. Nanopoulos, *Probing the desert using gauge coupling unification*, Physics Letters B **260**, 131–137 (1991).

[15] P. Langacker and M. Luo, *Implications of precision electroweak experiments for m_t, ρ_0, $\sin\theta_W{}^2$, and grand unification*, Physical Review D **44**, 817–822 (1991).

[16] J. Hisano, H. Murayama, and T. Yanagida, *Nucleon decay in the minimal supersymmetric SU(5) grand unification*, Nuclear Physics, Section B **402**, 46–84 (1993).

[17] K. Abe, Y. Hayato, T. Iida *et al.*, *Search for nucleon decay via $n \to \bar{\nu}\pi^0$ and $p \to \bar{\nu}\pi^+$ in super-kamiokande*, Physical Review Letters **113**, 1–6 (2014).

[18] H. Fritzsch and P. Minkowski, *Unified interactions of leptons and hadrons*, Annals of Physics **93**, 193–266 (1975).

[19] J.C. Pati and A. Salam, *Lepton number as the fourth "color"*, Physical Review D **10**, 275–289 (1974).

[20] N.T. Shaban and W.J. Stirling, *Minimal left-right symmetry and SO(10) grand unification using LEP coupling constant measurements*, Physics Letters B **291**, 281–287 (1992).

[21] D.g. Lee, R.N. Mohapatra, M.K. Parida *et al.*, *Predictions for the proton lifetime in minimal nonsupersymmetric SO(10) models: An update*, Physical Review D **51**, 229–235 (1995).

[22] M. Machacek, *The decay modes of the proton*, Nuclear Physics B **159**, 37–55 (1979).

[23] M.B. Gavela, A. Le Yaouanc, L. Oliver *et al.*, *Exclusive modes of proton decay in SU(5)*, Physics Letters B **98**, 51–56 (1981).

[24] J.F. Donoghue, *Proton lifetime and branching ratios in SU(5)*, Physics Letters B **92**, 99–102 (1980).

[25] F. Buccella, G. Miele, L. Rosa *et al.*, *An upper limit for the proton lifetime in SO(10)*, Physics Letters B **233**, 178–182 (1989).

[26] J. Ellis, M.K. Gaillard, and D. Nanopoulos, *On the effective lagrangian for baryon decay*, Physics Letters B **88**, 320–324 (1979).

[27] H. Nishino, K. Abe, Y. Hayato *et al.*, *Search for nucleon decay into charged antilepton plus meson in Super-Kamiokande I and II*, Physical Review D **85**, 112001 (2012).

[28] K. Abe, Y. Haga, Y. Hayato *et al.*, *Search for proton decay via $p \to e^+\pi^0$ and $p \to \mu^+\pi^0$ in 0.31 megaton·years exposure of the Super-Kamiokande water Cherenkov detector*, Physical Review D **95**, 1–10 (2017).

[29] K. Abe, C. Bronner, G. Pronost *et al.*, *Search for nucleon decay into charged antilepton plus meson in 0.316 megaton·years exposure of the Super-Kamiokande water Cherenkov detector*, Physical Review D **96**, 1–18 (2017).

[30] F. Reines, C.L. Cowan, and M. Goldhaber, *Conservation of the Number of Nucleons*, Physical Review **96**, 1157–1158 (1954).

[31] J.C. Evans and R.I. Steinberg, *Nucleon stability: A geochemical test independent of decay mode*, Science **197**, 989–991 (1977).

[32] F. Reines, C.L. Cowan, and H.W. Kruse, *Conservation of the Number of Nucleons*, Physical Review **109**, 609–610 (1958).

[33] M. Krishnaswamy, M. Menon, N. Mondal *et al.*, *Candidate events for nucleon decay in the Kolar Gold Field experiment*, Physics Letters B **106**, 339–346 (1981).

[34] G. Battistoni, *Tracking techniques in underground physics*, Nuclear Instruments and Methods in Physics Research Section A: Accelerators, Spectrometers, Detectors and Associated Equipment **279**, 137–141 (1989).

[35] W.W. Allison, G.J. Alner, I. Ambats *et al.*, *The SOUDAN 2 detector: The operation and performance of the tracking calorimeter modules*, Nuclear Instruments and Methods in Physics Research, Section A: Accelerators, Spectrometers, Detectors and Associated Equipment **381**, 385–397 (1996).

[36] S. Fukuda, Y. Fukuda, T. Hayakawa *et al.*, *The Super-Kamiokande detector*, Nuclear Instruments and Methods in Physics Research, Section A: Accelerators, Spectrometers, Detectors and Associated Equipment **501**, 418–462 (2003).

[37] R. Becker-Szendy, R.M. Bionta, C.B. Bratton *et al.*, *IMB-3: a large water Cherenkov detector for nucleon decay and neutrino interactions*, Nuclear Inst. and Methods in Physics Research, A **324**, 363–382 (1993).

[38] L.K. Pik, *Study of the neutrino mass hierarchy with the atmospheric neutrino data observed in Super-Kamiokande*", Ph.D. thesis, Kyoto University (2019).

[39] H. Nishino, K. Awai, Y. Hayato *et al.*, *High-speed charge-to-time converter ASIC for the Super-Kamiokande detector*, Nuclear Instruments and Methods in Physics Research, Section A: Accelerators, Spectrometers, Detectors and Associated Equipment **610**, 710–717 (2009).

[40] M. Shiozawa, *Reconstruction algorithms in the Super-Kamiokande large water Cherenkov detector*, Nuclear Instruments and Methods in Physics Research Section A: Accelerators, Spectrometers, Detectors and Associated Equipment **433**, 240–246 (1999).

[41] E.R. Davies, *Machine vision: theory, algorithms, practicalities*, Elsevier, (2004).

[42] M. Tanaka, *Search for proton decay into three charged leptons in Super-Kamiokande*", Ph.D. thesis, The University of Tokyo (2019).

[43] J.D. Gustafson, *A Search for baryon number violation by two units at the Super-Kamiokande detector*", Ph.D. thesis, Boston University (2016).

[44] T. James Irvine, *Development of Neutron-Tagging Techniques and Application to Atmospheric Neutrino Oscillation Analysis in Super-Kamiokande*", Ph.D. thesis, The University of Tokyo (2014).

[45] T. Mochizuki, *Development of 50-cm Diameter Photomultiplier Tubes and a Neutron Tagging Algorithm for Hyper-Kamiokande* (2019).

[46] Y. Suda, *Search for Proton Decay Using an Improved Event Reconstruction Algorithm in Super-Kamiokande*", Ph.D. thesis, The University of Tokyo (2017).

[47] K. Nakamura, S. Hiramatsu, T. Kamae *et al.*, *The reaction* $^{12}\mathrm{C}(\mathrm{e},\mathrm{e}'\mathrm{p})$ *at 700 MeV and DWIA analysis*, Nuclear Physics A **268**, 381–407 (1976).

[48] T. Yamazaki and Y. Akaishi, *Nuclear medium effects on invariant mass spectra of hadrons decaying in nuclei*, Physics Letters B **453**, 1–6 (1999).

[49] R.D. Woods and D.S. Saxon, *Diffuse surface optical model for nucleon-nuclei scattering*, Physical Review **95**, 577–578 (1954).

[50] M. Honda, T. Kajita, K. Kasahara *et al.*, *Calculation of atmospheric neutrino flux using the interaction model calibrated with atmospheric muon data*, Physical Review D - Particles, Fields, Gravitation and Cosmology **75**, 1–26 (2007).

[51] M. Honda, T. Kajita, K. Kasahara *et al.*, *Improvement of low energy atmospheric neutrino flux calculation using the JAM nuclear interaction model*, Physical Review D - Particles, Fields, Gravitation and Cosmology **83**, 1–34 (2011).

[52] J. Alcaraz, B. Alpat, G. Ambrosi *et al.*, *Cosmic protons*, Physics Letters, Section B: Nuclear, Elementary Particle and High-Energy Physics **490**, 27–35 (2000).

[53] J. Alcaraz, B. Alpat, G. Ambrosi *et al.*, *Helium in near earth orbit*, Physics Letters, Section B: Nuclear, Elementary Particle and High-Energy Physics **494**, 193–202 (2000).

[54] K. Niita, T. Sato, H. Iwase *et al.*, *PHITS-a particle and heavy ion transport code system*, Radiation Measurements **41**, 1080–1090 (2006).

[55] S. Roesler, R. Engel, and J. Ranft, *The Monte Carlo Event Generator DPMJET-III*, Advanced Monte Carlo for Radiation Physics, Particle Transport Simulation and Applications, 1033–1038 (2001).

[56] G. Battistoni, A. Ferrari, T. Montaruli *et al.*, *The FLUKA atmospheric neutrino flux calculation*, Astroparticle Physics **19**, 269–290 (2003).

[57] G.D. Barr, T.K. Gaisser, P. Lipari *et al.*, *Three-dimensional calculation of atmospheric neutrinos*, Physical Review D - Particles, Fields, Gravitation and Cosmology **70**, 13 (2004).

[58] Y. Hayato, *Neut*, Nuclear Physics B - Proceedings Supplements **112**, 171–176 (2002).

[59] Y. Hayato, *A neutrino interaction simulation program library NEUT*, Acta Physica Polonica B **40**, 2477–2489 (2009).

[60] C. Llewellyn Smith, *Neutrino reactions at accelerator energies*, Physics Reports **3**, 261–379 (1972).

[61] R.A. Smith and E.J. Moniz, *Neutrino reactions on nuclear targets*, Nuclear Physics, Section B **43**, 605–622 (1972).

[62] C.H. Albright, C. Quigg, R.E. Shrock *et al.*, *Neutrino-proton elastic scattering: Implications for weak-interaction models*, Physical Review D **14**, 1780–1798 (1976).

[63] K. Abe, L.A. Ahrens, K. Amako *et al.*, *Precise Determination of* $\sin\theta_W{}^2$ *from Measurements of the Differential Cross Sections for* $\nu_\mu p \to \nu_\mu p$ *and* $\bar{\nu}_\mu p \to \bar{\nu}_\mu p$, Physical Review Letters **56**, 1107–1111 (1986).

[64] D. Rein and L.M. Sehgal, *Neutrino-excitation of baryon resonances and single pion production*, Annals of Physics **133**, 79–153 (1981).

[65] C. Albright, C. Jarlskog, and L. Wolfenstein, *Neutrino production of M^+ and E^+ heavy leptons (II)*, Nuclear Physics B **84**, 493–502 (1975).

[66] M. Derrick, P. Gregory, L.G. Hyman *et al.*, *Properties of the hadronic system resulting from $\overline{\nu}_\mu p$ interactions*, Phys. Rev. D **17**, 1–15 (1978).

[67] S. Barlag and Others, *Charged Hadron Multiplicities in High-energy Anti-muon Neutrino n and Anti-muon Neutrino p Interactions*, Z. Phys. C **11**, 283 (1982).

[68] T. Sjostrand, *PYTHIA 5.7 and JETSET 7.4: Physics and manual* (1994).

[69] P. d Perio, S.K. Singh, J.G. Morfin *et al.*, AIP Conference Proceedings, 223–228 (2011).

[70] L. Salcedo, E. Oset, M. Vicente-Vacas *et al.*, *Computer simulation of inclusive pion nuclear reactions*, Nuclear Physics A **484**, 557–592 (1988).

[71] P.A. Zyla, R.M. Barnett, J. Beringer *et al.*, *Review of Particle Physics**, Progress of Theoretical and Experimental Physics **2020**, 1–878 (2020).

[72] B. Krusche and C. Wilkin, *Production of η and η' mesons on nucleons and nuclei*, Progress in Particle and Nuclear Physics **80**, 43–95 (2015).

[73] M. Röbig-Landau, J. Ahrens, G. Anton *et al.*, *Near threshold photoproduction of η-mesons from complex nuclei*, Physics Letters B **373**, 45–50 (1996).

[74] R. Arndt and Others. *INS Data Analysis Center*, `http://gwdac.phys.gwu.edu/`.

[75] B. Krusche, J. Ahrens, J. Annand *et al.*, *Near-threshold photoproduction of η-mesons from the deuteron*, Physics Letters B **358**, 40–46 (1995).

[76] G. Rowe, M. Salomon, and R.H. Landau, *Energy-dependent phase shift analysis of pion-nucleon scattering below 400 MeV*, Physical Review C **18**, 584–589 (1978).

[77] C.H.Q. Ingram, P.A.M. Gram, J. Jansen *et al.*, *Quasielastic scattering of pions from ^{16}O at energies around the $\Delta(1232)$ resonance*, Physical Review C **27**, 1578–1601 (1983).

[78] J. Albanese, J. Arvieux, J. Bolger *et al.*, *Elastic scattering of positive pions by ^{16}O between 80 and 340 MeV*, Nuclear Physics A **350**, 301–331 (1980).

[79] Y. Ashie, J. Hosaka, K. Ishihara *et al.*, *Measurement of atmospheric neutrino oscillation parameters by Super-Kamiokande I*, Physical Review D - Particles, Fields, Gravitation and Cosmology **71**, 1–35 (2005).

[80] G. Mitsuka, K. Abe, Y. Hayato *et al.*, *Study of nonstandard neutrino interactions with atmospheric neutrino data in Super-Kamiokande i and II*, Physical Review D - Particles, Fields, Gravitation and Cosmology **84**, 1–12 (2011).

[81] K. Abe and Others, *Hyper-Kamiokande Design Report*, KEK Preprint, 2016–21 (2016).